Nanostructured Surfaces for Controlling Absorption and Thermal Radiation

Master Thesis 2014

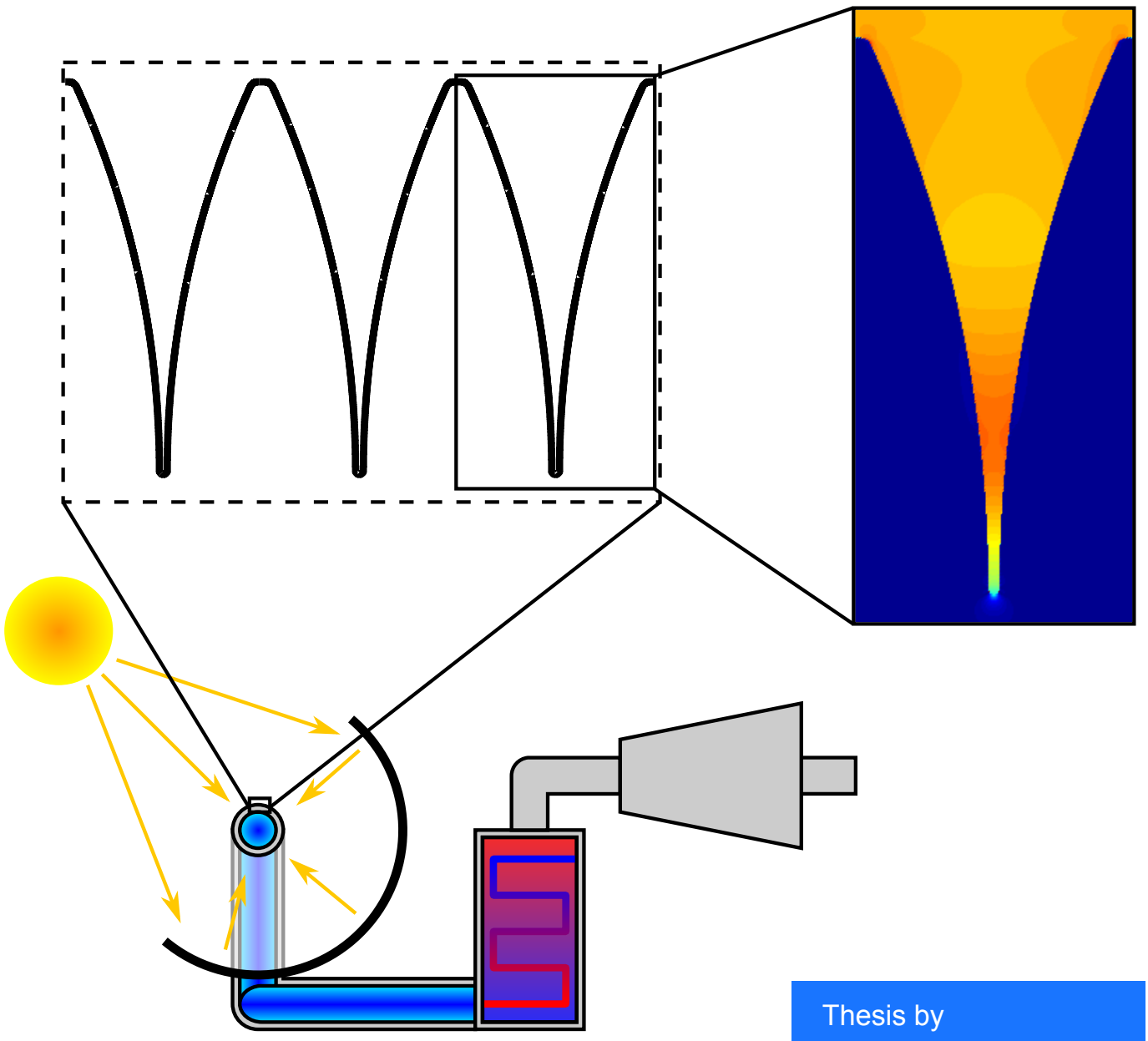

Thesis by

Mads Goldschmidt Laursen

Michael Odgaard

Supervised by

Thomas Søndergaard

AALBORG UNIVERSITY
DENMARK

Nanostructured Surfaces for Controlling Absorption and Thermal Radiation

Master thesis by
Mads Goldschmidt Laursen and Michael Odgaard
Aalborg University, Skjernvej 4A, DK-9220 Aalborg Øst

Supervised by
Thomas Søndergaard
Aalborg University, Skjernvej 4A, DK-9220 Aalborg Øst

Abstract

In this thesis the reflectance of ultra-sharp periodic groove arrays in a gold surface is studied for a general direction of light incidence. This includes the case of incident light propagating along the grooves. These structures are interesting due to their tunable absorption selective properties, which make them promising candidates in various methods of renewable energy production such as thermophotovoltaics and concentrated solar power. Two efficient numerical modelling approaches are presented, namely a simple and approximate stack matrix method that uses the mode-index of gap-plasmon polaritons (G-SPP's) as an effective index, and a rigorous Green's Function Surface Integral Equation Method (GFSIEM). The results of the highly simple stack matrix method show remarkable similarity to the exact results obtained with the rigorous GFSIEM, which reinforces the idea that the physics of light absorption in such structures is dominated by the coupling of light into plasmons.

Danish Abstract

I denne afhandling undersøges reflektansen af ultraskarpe periodiske rillestrukturer i en guldoverflade for en generel indfaldsvinkel af lys. Dette inkluderer situationen, hvor lyset propagerer langs rillerne. Disse strukturer er interessante grundet deres kontrollerbare absorptionsegenskaber, som gør dem til attraktive materialer til brug i forskellige metoder til produktion af vedvarende energi såsom thermophotovoltaics og koncentreret solenergi. To effektive numeriske metoder præsenteres: en simpel og tilnærmet lag-matrice-metode, der bruger mode-indekset for gap-plasmoner (G-SPP'er) som et effektivt brydningsindeks, og en grundig Greens-funktions Overflade-integrale-lignings-metode (GFSIEM). Resultaterne af den simple lag-matrice-metode viser bemærkelsesværdige ligheder med de præcise resultater opnået med den nøjagtige GFSIEM, hvilket forstærker idéen om, at fysikken bag absorptionen af lys i sådanne strukturer domineres af koblingen af lys til plasmoner.

Concluded June 4, 2014
Number of pages: 74 (82)
Number of appendices: 3

Preface

This Master thesis was written by the authors during the Master's degree program Nanophysics and -materials at the Department of Physics of Nanotechnology at Aalborg University during the period of September 1, 2013 - June 4, 2014.

Sources are denoted by numbers in square brackets, [#]. These numbers correspond to entries in the bibliography found at the end of the thesis. Page numbers are given in citations when relevant. In the bibliography sources are listed by author, title, and year. Publisher and ISBN are given for books, and journal is given for articles and papers.

The work presented in this thesis was submitted to the Journal of the Optical Society of America B under the title *Modeling the Reflectivity of Plasmonic Ultra-sharp Groove Arrays: General Direction of Light Incidence* on May 1, 2014, and it is currently undergoing peer review. The submitted manuscript is included in Appendix C.

The cover illustration depicts one of the ultra-sharp groove structures under consideration in this thesis and the magnetic field distribution in the groove as well as a possible use of the structure in a concentrated solar power application.

Attached to the back cover of this thesis is a CD containing a PDF of the paper, a PDF of the submitted manuscript, as well as the developed MATLAB programs for calculating the reflectance of ultra-sharp groove structures.

Abbreviations

CSP:	Concentrated Solar Power
GFSIEM:	Green's Function Surface Integral Equation Method
G-SPP:	Gap-Surface-Plasmon-Polariton
PBM:	Plasmonic Black Metal
SMM:	Stack Matrix Method
SPP:	Surface-Plasmon-Polariton
TPV:	Thermophotovoltaics

Mads G. Laursen

Michael Odgaard

Contents

Introduction 1

The design of materials with absorption selective properties is relevant in many current fields of research such as thermophotovoltaics (TPV) and concentrated solar power (CSP). TPV and CSP are both promising technologies for renewable energy production. TPV is similar to conventional photovoltaics in the sense that it is based on the conversion of electromagnetic radiation into electricity. In TPV, however, the incident electromagnetic radiation comes from thermal emission from a source heated to a high temperature. The advantage of TPV compared to conventional photovoltaics lies in the fact that it is possible to convert a larger amount of the total input energy into electricity by modifying the properties of the emitting material to fit with the photovoltaic material used. By tuning the emitting material such that the wavelength of maximum emission corresponds to the bandgap of the semiconductor used as the photovoltaic material, a high level of efficiency can be achieved. The source used to heat the emitter can be e.g. sunlight or excess heat from other methods of electricity production. For a comprehensive treatment of concepts related to TPV see e.g. [1].

CSP is based on the use of large mirrors to capture and focus sunlight onto a collector. A variety of different CSP systems exist, but common for all of them is that the collector is heated through absorption of focused sunlight. A common construction of a CSP system consists of large parabolic mirrors, which focus the sunlight onto absorber tubes filled with a synthetic oil acting as a heat transfer fluid. The fluid is transported to a heat exchanger, where a reservoir of water is heated and converted into steam, which drives a turbine to produce electricity. Fig. 1.1 shows a schematic of a CSP based power plant. In many modern CSP power plants a thermal storage is included in the form of a reservoir of molten salt. In this way the energy can be stored to accomodate for periods of peak electricity consumption, which typically do not coincide with the periods of maximum production of solar based power plants. [2]

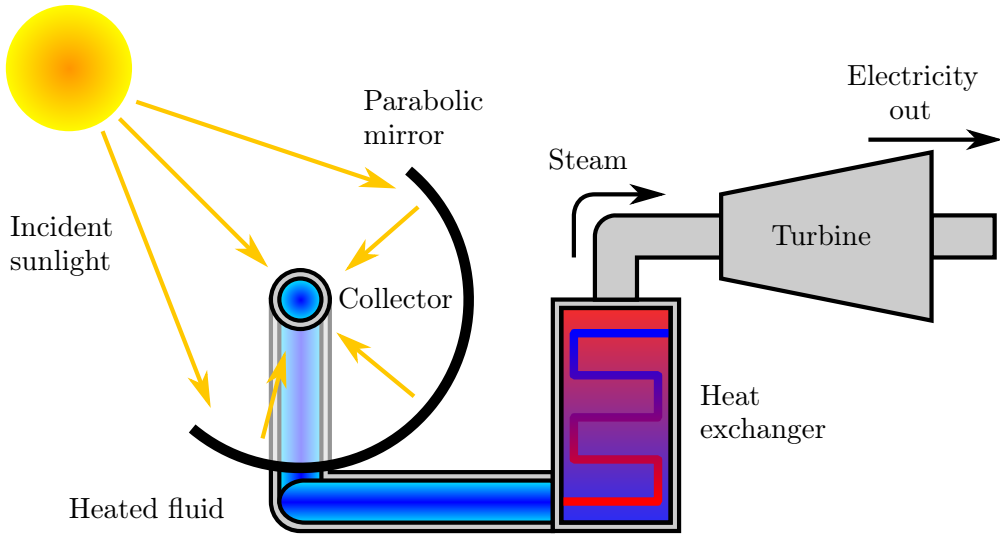

Figure 1.1. Schematic of a power plant based on CSP.

From the brief introduction to TPV and CSP given above it is evident that both of these methods of electricity production are highly dependent on materials with appropriate absorption and emission properties. In the case of TPV the ideal emitter material has a sharply defined wavelength of maximum emission, with little emission occurring at other wavelengths. For a CSP system the absorber material should absorb the incident sunlight very efficiently while minimizing losses due to thermal radiation at infrared wavelengths. According to Kirchhoff's law of thermal radiation, the emittance of a material is identical to its absorbtance. Thus for a TPV emitter it is desirable to produce a material with a sharply defined absorbtance maximum, and for a CSP absorber it is desirable to produce a material with high absorbtance across the visible spectrum and low absorptance (high reflectance) at infrared wavelengths corresponding to thermal radiation.

A widely used approach to the creation of materials with tunable absorption properties is the structuring of metal surfaces on a sub-wavelength scale. Specifically the production of black materials based on metal nanostructures is widely investigated [3–7]. The main subject of this thesis is a so-called plasmonic black metal (PBM) based on a periodic array of ultra-sharp grooves in a metal surface. Such structures have been demonstrated to drastically alter the optical properties of a metal surface for a broad wavelength range, turning it into a broadband absorber or black surface [8].

The optical properties of a PBM are connected to the coupling of incident light into gap-surface-plasmon-polaritons (G-SPP's), which are waves propagating in the dielectric gap between the metal groove walls. The structures under consideration in this thesis are one-dimensionally periodic arrays of ultra-sharp grooves in a gold surface constructed such that they allow for adiabatic nanofocusing of G-SPP's. This is done by designing convex groove walls with slopes such that the reflection for a G-SPP propagating into the groove is minimized [9]. Such a surface may also be used as a broadband low-dispersion polarizer for ultra-short laser pulses [10]. In general it is observed that the absorption properties are sensitive to the exact surface geometry and the angle of light incidence. The focus of this

thesis is the modelling of these structures under a general direction of light incidence. As an example of the structures under consideration in this thesis, Fig. 1.2 shows the surfaces of the structures with bottom widths of 0.3 and 10 nm.

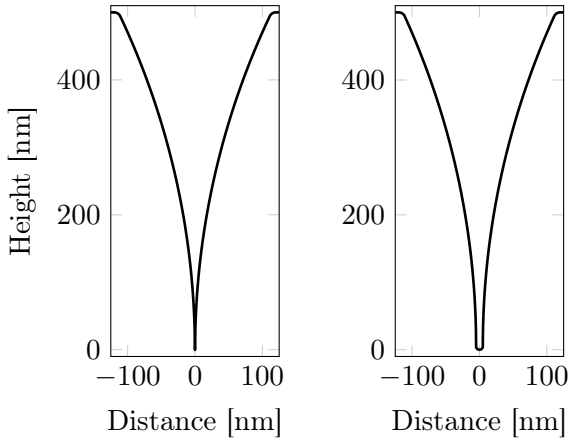

Figure 1.2. The surfaces of the groove structures with bottom widths of 0.3 (left) and 10 nm (right). Each graph represents one period of the respective structure.

In many theoretical studies of the optics of one-dimensionally periodic gratings it is common to only consider a direction of light incidence in the plane spanned by the surface normal vector and the direction of periodicity (see e.g. [9, 11–16]). This is a convenient restriction, since it greatly reduces the complexity of the theoretical problem. However, this means that out of convenience a general direction of light incidence on such structures is rarely considered. In some cases a general direction of light incidence has been considered for non-periodic structures [17], and the rigorous coupled wave analysis has been applied to a general direction of light incidence for small angles [18].

In this thesis two efficient numerical methods are applied to model the reflectance of periodic arrays of ultra-sharp grooves. These methods are an approximate stack matrix method and a rigorous Green's Function Surface Integral Equation Method (GFSIEM). The stack matrix method takes advantage of the physical interpretation that wave propagation in the grooves is almost entirely governed by G-SPP waves. The GFSIEM, on the other hand, is a rigorous and highly efficient method for the modelling of general electromagnetic scattering problems [19–24]. While the GFSIEM is widely used for two-dimensional scattering problems, not much attention has been given to formulating a GFSIEM for solving scattering problems under a general direction of light incidence.

With the above considerations in mind, this thesis contains

- A presentation of the theory behind the stack matrix method and the GFSIEM as well as a brief introduction to the concepts of G-SPP's and thermal emission.
- A description of the MATLAB code developed to model the reflectance of periodic groove structures.
- A presentation of the results of the reflectance calculations with the different numerical methods.

Theory 2

This chapter contains a presentation of relevant theory for the understanding of the concepts treated in this thesis. First an introduction to plasmons and G-SPP's is given, since the interaction of light with the structures under consideration is heavily dominated by the coupling of light into G-SPP's. This is followed by a description of the concepts behind the stack matrix method and an outline of the required components for describing a given system as a stack matrix. In the sections following this a description of Green's functions and the GFSIEM is given. First the dyadic Green's function is introduced, which is followed by a description of the construction of a two-dimensional Green's function as well as a periodic two-dimensional Green's function. These Green's functions are then used as the starting point for describing the GFSIEM for both non-periodic and periodic cases. Finally an introduction to the basic concepts of thermal emission is given. While no specific treatment of thermal emission is given in this thesis, this section is included since it is highly relevant for potential applications of the investigated groove structures, such as TPV and CSP.

2.1 Plasmons

This section contains an introduction to the concepts of surface-plasmon-polaritons (SPP's) as well as a description of G-SPP's. SPP's are introduced first since the basics of G-SPP's are very similar to those of SPP's. The description of G-SPP's also contains a derivation of the equations required to determine the effective mode index of a G-SPP in a given structure as well as a description of how to solve these equations numerically on a computer.

2.1.1 Surface-Plasmon-Polaritons

Surface-plasmon-polaritons (SPP's) are oscillations in charge density propagating along a surface. SPP's represent specific solutions to Maxwell's equations, which appear when certain boundary conditions are fulfilled. The simplest form of SPP's can appear at a plane interface between a metal and a dielectric. In order to illustrate this, an interface between two materials with different dielectric constants, ε_1 and ε_2, as illustrated in Fig. 2.1 is considered. [25, pp. 377-379]

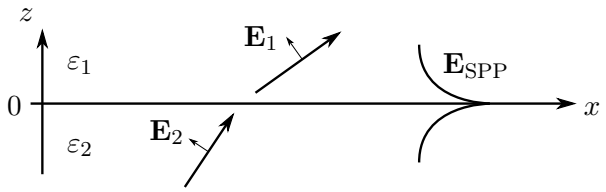

Figure 2.1. An interface between two materials with different dielectric constants, ε_1 and ε_2. $\mathbf{E}_2$ represents incident radiation in medium 2, $\mathbf{E}_1$ represents the transmitted radiation into medium 1, and $\mathbf{E}_{\mathrm{SPP}}$ represents the electric field of a SPP bound to the interface and propagating in the x direction. The electric field of the SPP decays exponentially away from the interface, i.e. in the z direction. Inspired by [25, p. 378].

In a situation as illustrated in the figure an SPP is characterized by a solution of the wave equation localized at the interface. Starting from the wave equation gives

$$\left(\nabla^2 + k_0^2\varepsilon(\mathbf{r})\right)\mathbf{E} = 0 \quad \Rightarrow \quad -k_x^2 - k_z^2 + k_0^2\varepsilon = 0 \quad \Rightarrow \quad k_z = \sqrt{k_0^2\varepsilon - k_x^2}. \tag{2.1}$$

In order for an interface bound mode to exist k_z must be purely imaginary. Furthermore, the incident radiation must be p polarized, since an electric field component in the direction of propagation is required. As such the electric field is given by

$$z > 0: \quad \mathbf{E} = (\hat{x}E_{x1} + \hat{z}E_{z1})\, e^{-ik_x x} e^{-ik_{z1} z}, \tag{2.2}$$

$$z < 0: \quad \mathbf{E} = (\hat{x}E_{x2} + \hat{z}E_{z2})\, e^{-ik_x x} e^{ik_{z2} z}. \tag{2.3}$$

Since both materials are source free, $\nabla \cdot \mathbf{D} = \nabla \cdot \varepsilon\mathbf{E} = 0$ must be fulfilled for $z > 0$ and $z < 0$. That is

$$z > 0: \quad \nabla \cdot \mathbf{E} = -ik_x E_{x1} - ik_{z1} E_{z1} = 0 \quad \Rightarrow \quad E_{z1} = E_{x1}\left(-\frac{k_x}{k_{z1}}\right), \tag{2.4}$$

$$z < 0: \quad \nabla \cdot \mathbf{E} = -ik_x E_{x2} + ik_{z2} E_{z2} = 0 \quad \Rightarrow \quad E_{z2} = E_{x2}\left(\frac{k_x}{k_{z2}}\right). \tag{2.5}$$

Furthermore, the tangential component of the $\mathbf{E}$ field and the normal component of the $\mathbf{D}$ field must be conserved across the interface, i.e.

$$\mathbf{E}_1^{\parallel} = \mathbf{E}_2^{\parallel}, \tag{2.6}$$

$$\mathbf{D}_1^{\perp} = \mathbf{D}_2^{\perp}. \tag{2.7}$$

Applying boundary condition (2.6) gives

$$E_{x1} = E_{x2} = E_x, \tag{2.8}$$

and boundary condition (2.7) gives

$$\begin{aligned} D_{z1} = D_{z2} \quad &\Rightarrow \quad \varepsilon_1\left(-\frac{k_x}{k_{z1}}\right)E_x = \varepsilon_2\left(\frac{k_x}{k_{z2}}\right)E_x \\ &\Rightarrow \quad \varepsilon_1 k_{z2} + \varepsilon_2 k_{z1} = 0. \end{aligned} \tag{2.9}$$

With some further calculations an expression for k_x can be found:

$$\begin{aligned}\varepsilon_1^2 k_{z2}^2 = \varepsilon_2^2 k_{z1}^2 \quad &\Rightarrow \quad \varepsilon_1^2(k_0^2\varepsilon_2 - k_x^2) = \varepsilon_2^2(k_0^2\varepsilon_1 - k_x^2) \\ &\Rightarrow \quad k_x^2(\varepsilon_1^2 - \varepsilon_2^2) = k_0^2(\varepsilon_1^2\varepsilon_2 - \varepsilon_2^2\varepsilon_1) = k_0^2\varepsilon_1\varepsilon_2(\varepsilon_1 - \varepsilon_2) \\ &\Rightarrow \quad k_x^2 = k_0^2\frac{\varepsilon_1\varepsilon_2}{\varepsilon_1 + \varepsilon_2} \quad \Rightarrow \quad k_x = k_0\sqrt{\frac{\varepsilon_1\varepsilon_2}{\varepsilon_1 + \varepsilon_2}}. \end{aligned} \tag{2.10}$$

Inserting this expression for k_x into the expression for k_z given by Eq. (2.1) gives

$$k_{z1} = k_0\sqrt{\frac{\varepsilon_1(\varepsilon_1 + \varepsilon_2) - \varepsilon_1\varepsilon_2}{\varepsilon_1 + \varepsilon_2}} = k_0\sqrt{\frac{\varepsilon_1^2}{\varepsilon_1 + \varepsilon_2}}, \tag{2.11}$$

$$k_{z2} = k_0\sqrt{\frac{\varepsilon_2^2}{\varepsilon_1 + \varepsilon_2}}. \tag{2.12}$$

In order for the wave to propagate along the x direction and be dampened in the z direction, which corresponds to a surface-bound wave, k_x must be real, and k_z must be imaginary. In order for this to be fulfilled, the dielectric constants for the two materials must obey

$$\varepsilon_1 + \varepsilon_2 < 0 \quad \text{and} \quad \varepsilon_1\varepsilon_2 < 0. \tag{2.13}$$

Eq. (2.13) is the so-called SPP criterion. It is fulfilled when the dielectric constant of one material has a negative real part with a greater absolute value than the (positive) real part of the dielectric constant of the other material. [25, pp. 377-379]

It should be noted, however, that Eq. (2.13) arises from the assumption that both of the dielectric constants are real. In reality the dielectric constants are complex, where the imaginary part describes losses in the materials. When losses in the materials are taken into account, the SPP criterion will not be as simple as Eq. (2.13).

2.1.2 Gap-Surface-Plasmon-Polaritons

Another type of plasmons is gap-surface-plasmon-polaritons (G-SPP's), which are SPP's propagating in a thin dielectric layer sandwiched between two metal surfaces. This situation is illustrated in Fig. 2.2. Structures supporting propagating G-SPP's have been studied by several groups such as Prade, Vinet and Mysyrowicz [26] and Bozhevolnyi and Jung [27]. Furthermore, the optical properties of the ultra-sharp groove structures under consideration in this thesis are heavily influenced by the coupling of light into G-SPP's [8]. In this section we derive an analytical expression for a determinant, which may be solved numerically in order to obtain the G-SPP mode index.

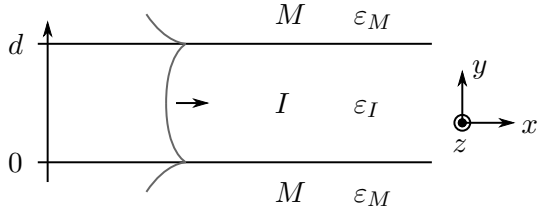

Figure 2.2. A dielectric layer, I, of thickness d sandwiched between two metal surfaces, M, allowing for propagation of G-SPP's along the x-direction.

Consider a dielectric layer, I, of thickness d sandwiched between two metal surfaces, M, as shown in Fig. 2.2. Similar to the situation of SPP's, where surface-bound modes can only exist for p polarized radiation, the existence of solutions to the problem of G-SPP's requires the propagating wave to be p polarized. With the chosen coordinate system the magnetic field of a p polarized wave is purely in the z direction, $\mathbf{H} = \hat{z}H$. The magnetic field as a function of x and y can then be written as

$$H(x,y) = e^{-i\beta x} f(y), \tag{2.14}$$

where β is the propagation constant corresponding to k_x for the SPP case given in Eq. (2.10), and $f(y)$ is an appropriate function, which describes the variation in the y-direction. In order to describe a G-SPP, this function should be constructed such that the field decays exponentially into both metal layers. This can be done as

$$y > d: \quad H = e^{-i\beta x} A e^{-i\kappa_{yM}(y-d)}, \tag{2.15}$$

$$0 < y < d: \quad H = e^{-i\beta x}\left(B e^{-i\kappa_{yI} y} + C e^{i\kappa_{yI} y}\right), \tag{2.16}$$

$$y < 0: \quad H = e^{-i\beta x} e^{i\kappa_{yM} y} D. \tag{2.17}$$

Here A, B, C, and D are constants to be determined. Furthermore, requiring the expressions to satisfy the wave equation gives

$$\left(\nabla^2 + k_0^2 \varepsilon(y)\right) H = 0 \quad \Rightarrow \quad \kappa_{yM} = \sqrt{k_0^2 \varepsilon_M - \beta^2}, \tag{2.18}$$

$$\kappa_{yI} = \sqrt{k_0^2 \varepsilon_I - \beta^2}, \tag{2.19}$$

where ε_M and ε_I are the dielectric constants of the metal and the dielectric, respectively. In order to determine the constants A, B, C, and D in Eqs. (2.15)-(2.17) the appropriate boundary conditions have to be considered. At both metal/dielectric interfaces the tangential components of the magnetic and electric fields have to be conserved. Since the interfaces are located at $y = 0$ and $y = d$, the conservation of the tangential component of the magnetic field yields, from Eqs. (2.15)-(2.17),

$$A = B e^{-i\kappa_{yI} d} + C e^{i\kappa_{yI} d}, \tag{2.20}$$

$$B + C = D. \tag{2.21}$$

The tangential component of the electric field is found as

$$\nabla \times \mathbf{H} = \frac{\partial \mathbf{D}}{\partial t} = i\omega\varepsilon_0 \varepsilon \mathbf{E} \quad \Rightarrow \quad E_x = \frac{-i}{\omega\varepsilon_0 \varepsilon} \frac{\partial H}{\partial y}. \tag{2.22}$$

Once again using Eqs. (2.15)-(2.17), the conservation of the tangential component of the electric field yields

$$\frac{1}{\varepsilon_M} i\kappa_{yM} A - \frac{1}{\varepsilon_I} i\kappa_{yI} B e^{-i\kappa_{yI} d} + \frac{1}{\varepsilon_I} i\kappa_{yI} C e^{i\kappa_{yI} d} = 0, \tag{2.23}$$

$$-\frac{1}{\varepsilon_M} i\kappa_{yM} D - \frac{1}{\varepsilon_I} i\kappa_{yI} B + \frac{1}{\varepsilon_I} i\kappa_{yI} C = 0. \tag{2.24}$$

The set of Eqs. (2.20), (2.21), (2.23), and (2.24) can then be reduced to a set of two equations with two unknowns. This process is shown in detail in Appendix A.1. With the

final expression for the determinant given as

$$\begin{aligned}
&\frac{1}{\varepsilon_I^2}\kappa_{yI}^2 + \frac{1}{\varepsilon_M^2}\kappa_{yM}^2 - \frac{1}{\varepsilon_I^2}\kappa_{yI}^2 e^{2i\kappa_{yI}d} - \frac{1}{\varepsilon_M^2}\kappa_{yM}^2 e^{2i\kappa_{yI}d} \\
&- \frac{2}{\varepsilon_M\varepsilon_I}\kappa_{yM}\kappa_{yI} - \frac{2}{\varepsilon_M\varepsilon_I}\kappa_{yM}\kappa_{yI}e^{2i\kappa_{yI}d} = 0 \qquad (2.25) \\
&\Updownarrow \\
&[1 - \exp(2i\kappa_{yI}d)]\left(\frac{\kappa_{yI}^2}{\varepsilon_I^2} + \frac{\kappa_{yM}^2}{\varepsilon_M^2}\right) - [1 + \exp(2i\kappa_{yI}d)]\frac{2\kappa_{yM}\kappa_{yI}}{\varepsilon_M\varepsilon_I} = 0, \qquad (2.26)
\end{aligned}$$

it is possible to solve the rest of the problem numerically on a computer such that an effective mode index may be obtained. [27]

One possible way of numerically solving the problem is by use of the Newton-Raphson method, which is the method that is used in the present work. The basic idea of the Newton-Raphson method is to start from a guess for the solution, x_0, and then iteratively approach the correct solution by making new guesses on the form of

$$x_{n+1} = x_n - \frac{f(x_n)}{f'(x_n)}, \qquad (2.27)$$

where x_{n+1} is the new guess, and x_n is the previous guess. $f(x_n)$ and $f'(x_n)$ represent the value and the derivative of the function in the point x_n, respectively. This form of guesses iteratively approaches the root of the function by shooting closer and closer to the correct value using the slope of the tangent in a given point. In order for the Newton-Raphson method to converge, however, the initial guess should be relatively close to the correct solution. Otherwise the next guess might overshoot and thus never arrive at the correct solution.

The process of solving the problem with the Newton-Raphson method on a computer goes as follows. First the determinant given in Eq. (2.26) is calculated for a range of values of β. The values of β are chosen in a way such that they span a grid of combinations of real and imaginary parts. Since the computation time for this problem scales as N^2, where N is the number of different values of real or imaginary parts tested, this grid should be relatively small in order to minimize the required computation time. The next step is to examine each area of the resulting grid of determinant values. As the problem will have a solution when the resulting determinant is 0, the idea is to find zeroes in the determinant grid. Due to the way the grid is constructed it is highly unlikely that any of the grid points result in a determinant value of exactly 0. However, if the signs of both the real and imaginary part of the determinant change between neighbouring grid points, there will be a root somewhere between these points. Thus the determinant values for each set of four grid points are compared, and when an area is found in which both the imaginary and real parts change sign, an initial guess for the solution can be made by taking the centre of this area as the guess. For this method to be able to locate zeroes, however, it is important that the grid points are not spaced too far from each other. If the grid points are spaced too far it is possible that one or both of the real and imaginary parts may change sign twice within the same area, and in this case the check will fail even if the solution is within the given area.

The process of constructing new guesses on the form of Eq. (2.27) is continued until a given guess x_{n+1} is within some threshold of the guess x_n, e.g. $x_{n+1} - x_n < 10^{-8}$. As mentioned previously the Newton-Raphson method essentially shoots closer and closer to the correct solution, and as such when a given guess is very close to the previous guess, this guess will also be very close to the correct solution. If the initial guess is good, the method will usually converge quickly. Thus if the process runs for more than e.g. 100 iterations it can be assumed that the initial guess was not good enough, and the process should be run again with a different initial guess.

2.2 The Stack Matrix Method

The stack matrix method is a method used to determine the reflectance and transmittance of an optical system consisting of a stack of layers with parallel interfaces such as the one shown in Fig. 2.3. While the structures under consideration in this thesis do not consist of stacks of parallel layers it is possible to model them as such by using the effective mode index for a G-SPP, which was described in the previous section. In this way a representation of the structure may be constructed by considering the groove structure as a stack of layers, where each layer is described by an effective mode index corresponding to that for a G-SPP propagating in a gap of the same width as the groove width at that point.

The basic idea of the stack matrix method is to set up specific matrices to represent the various factors that affect the propagation of light through a multilayer system and then combine these matrices into a single stack matrix, which describes the entire system. The approach presented in the following is based on s polarized light, although a completely analogous procedure may be carried out for p polarization by using the magnetic fields rather than the electric fields.

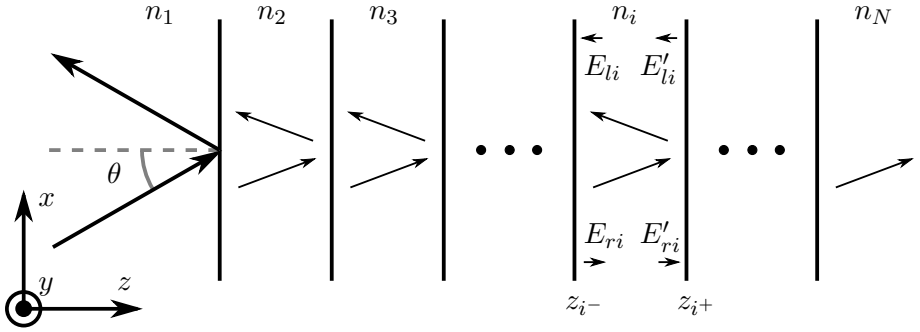

Figure 2.3. A multilayer system consisting of a stack of N parallel layers. Inspired by [28, p. 297].

Consider the stack of N parallel layers shown in Fig. 2.3. In each layer the electric field is described by the field components E_{ri} and E'_{ri} propagating to the right and the field components E_{li} and E'_{li} propagating to the left. The unprimed and primed notations refer to the fields on the left and right sides of the layer, respectively. For s polarization the electric fields are given as $\mathbf{E} = \hat{y}E(x, z)$. The electric field in the first layer near the interface to the

second layer, i.e. E_1', can then be expressed as

$$\begin{aligned} E_1'(x,z) &= E_{r1}' e^{-ik_0 n_1(\cos(\theta)z + \sin(\theta)x)} + E_{l1}' e^{-ik_0 n_1(-\cos(\theta)z + \sin(\theta)x)} \\ &= e^{-ik_0 n_1 \sin(\theta)x}\left(E_{r1}' e^{-ik_0 n_1 \cos(\theta)z} + E_{l1}' e^{ik_0 n_1 \cos(\theta)z}\right). \end{aligned} \tag{2.28}$$

Similarly the field in the second layer near the interface to the first layer, i.e. E_2, can be expressed as

$$E_2(x,z) = e^{-ik_0 n_1 \sin(\theta)x}\left(E_{r2} e^{-i\beta_2 z} + E_{l2} e^{i\beta_2 z}\right). \tag{2.29}$$

In this equation β_2 represents the phase shift of the electric field caused by the change in material from layer 1 to layer 2. An expression for β_2 can be found by inserting Eq. (2.29) into the wave equation, $(\nabla^2 + k_0^2 n^2)\mathbf{E} = 0$. This gives

$$\begin{aligned} & k_0^2 n_1^2 \sin^2(\theta) + \beta_2^2 - k_0^2 n_2^2 = 0 \\ \Rightarrow\ & \beta_2^2 = k_0^2 n_2^2 - k_0^2 n_1^2 \sin^2(\theta). \end{aligned} \tag{2.30}$$

A general expression for β_i in layer i is similarly found as

$$\beta_i^2 = k_0^2 n_i^2 - k_0^2 n_1^2 \sin^2(\theta). \tag{2.31}$$

The electric fields (2.28) and (2.29) must fulfil the boundary condition

$$E_1'(x, z = 0^-) = E_2(x, z = 0^+) \quad \Rightarrow \quad E_{r1}' + E_{l1}' = E_{r2} + E_{l2}. \tag{2.32}$$

Furthermore, the tangential components of the magnetic fields must be conserved across the interface. These are found through the relation

$$\boldsymbol{\nabla} \times \mathbf{E} = \frac{-\partial \mathbf{B}}{\partial t} = i\omega\mu_0 \mathbf{H} = -\hat{x}\frac{\partial E}{\partial z} + \hat{z}\frac{\partial E}{\partial x}. \tag{2.33}$$

Conservation of the tangential component of $\mathbf{H}$ thus yields

$$\begin{aligned} & \frac{\partial E_1'}{\partial z}\Big|_{z=0^-} = \frac{\partial E_2}{\partial z}\Big|_{z=0^+} \\ \Rightarrow\ & i\beta_1(E_{l1}' - E_{r1}') = i\beta_2(E_{l2} - E_{r2}). \end{aligned} \tag{2.34}$$

For the case where only the first interface is considered, no light propagates to the left in layer 2, i.e. $E_{l2} = 0$. Then Eqs. (2.32) and (2.34) reduce to

$$E_{r1}' + E_{l1}' = E_{r2}, \tag{2.35}$$

$$\frac{\beta_1}{\beta_2}(E_{r1}' - E_{l1}') = E_{r2}. \tag{2.36}$$

From these equations the reflection coefficient between layers 1 and 2, ρ_{12}, can be found as the ratio between E_{l1}' and E_{r1}',

$$\begin{aligned} & E_{r1}' + E_{l1}' = \frac{\beta_1}{\beta_2}(E_{r1}' - E_{l1}') \\ \Rightarrow\ & E_{r1}'\left(\frac{\beta_1}{\beta_2} - 1\right) = E_{l1}'\left(1 + \frac{\beta_1}{\beta_2}\right) \\ \Rightarrow\ & \frac{E_{l1}'}{E_{r1}'} = \rho_{12} = \frac{\frac{\beta_1}{\beta_2} - 1}{\frac{\beta_1}{\beta_2} + 1} = \frac{\beta_1 - \beta_2}{\beta_1 + \beta_2}. \end{aligned} \tag{2.37}$$

The transmission coefficient, τ_{12}, is simply

$$\tau_{12} = \frac{E_{r2}}{E'_{r1}} = \frac{2\beta_1}{\beta_1 + \beta_2} = 1 + \rho_{12}. \tag{2.38}$$

From the definition of the reflection and transmission coefficients it follows naturally that $\rho_{12} = -\rho_{21}$ and $\tau_{21} = 1 + \rho_{21}$. If the incident light is p polarized, the coefficients must instead be found from the magnetic fields. In this case they become

$$\rho_{12,p} = \frac{H'_{l1}}{H'_{r1}} = \frac{\frac{\beta_1}{\varepsilon_1} - \frac{\beta_2}{\varepsilon_2}}{\frac{\beta_1}{\varepsilon_1} + \frac{\beta_2}{\varepsilon_2}}, \tag{2.39}$$

$$\tau_{12,p} = \frac{H_{r2}}{H'_{r1}} = \frac{2\frac{\beta_1}{\varepsilon_1}}{\frac{\beta_1}{\varepsilon_1} + \frac{\beta_2}{\varepsilon_2}} = 1 + \rho_{12,p}, \tag{2.40}$$

where ε_1 and ε_2 are the relative dielectric constants of materials 1 and 2. The reflection and transmission coefficients given by Eqs. (2.37)-(2.40) are completely general and can be used for any two adjacent layers i and j by substituting the appropriate β's. Using the coefficients for s polarization the electric field components in two adjacent layers i and j can be expressed in terms of each other as

$$E'_{li} = \rho_{ij} E'_{ri} + \tau_{ji} E_{lj}, \tag{2.41}$$

$$E_{rj} = \tau_{ij} E'_{ri} + \rho_{ji} E_{lj}, \tag{2.42}$$

or

$$E'_{ri} = \frac{1}{\tau_{ij}}(E_{rj} - \rho_{ji} E_{lj}), \tag{2.43}$$

$$E'_{li} = \frac{\rho_{ij}}{\tau_{ij}}(E_{rj} - \rho_{ji} E_{lj}) + \tau_{ji} E_{lj} = \frac{1}{\tau_{ij}} \left[E_{rj}\rho_{ij} + \left(\underbrace{\tau_{ji}\tau_{ij} - \rho_{ji}\rho_{ij}}_{1} \right) E_{lj} \right]. \tag{2.44}$$

By introducing the interface transition matrix

$$\mathbf{H}_{ij} = \frac{1}{\tau_{ij}} \begin{bmatrix} 1 & \rho_{ij} \\ \rho_{ij} & 1 \end{bmatrix}, \tag{2.45}$$

Eqs. (2.43) and (2.44) can be expressed in matrix form as

$$\begin{bmatrix} E'_{li} \\ E'_{ri} \end{bmatrix} = \mathbf{H}_{ij} \begin{bmatrix} E_{lj} \\ E_{rj} \end{bmatrix}. \tag{2.46}$$

In order to fully describe the system by matrices one more relation is needed, namely the relation between the fields at the two ends of a layer, E_{li}, E_{ri} and E'_{li}, E'_{ri}. The field inside the layer can be expressed as functions of z in two ways as

$$E_i(z) = e^{-ik_0 n_i \sin(\theta)x} \left(E_{ri} e^{-i\beta_i (z - z_{i^-})} + E_{li} e^{i\beta_i (z - z_{i^-})} \right), \tag{2.47}$$

$$E_i(z) = e^{-ik_0 n_i \sin(\theta)x} \left(E'_{ri} e^{-i\beta_i (z - z_{i^+})} + E'_{li} e^{i\beta_i (z - z_{i^+})} \right), \tag{2.48}$$

where z_{i^-} is the position in z of the interface between layers $(i-1)$ and i, and z_{i^+} is the position in z of the interface between layers i and $(i+1)$, see Fig. 2.3. By inserting the

values $z = z_{i^-}$ and $z = z_{i^+}$ into Eqs. (2.47) and (2.48) and setting the two expressions equal to each other for each of these values of z, E_{ri} and E_{li} can be expressed as functions of E'_{ri} and E'_{li}, respectively. With the thickness of layer i defined as $z_{i^+} - z_{i^-} = d_i$, the relation can be described through the layer propagation matrix

$$\mathbf{L}_i = \begin{bmatrix} \exp(-i\beta_i d_i) & 0 \\ 0 & \exp(i\beta_i d_i) \end{bmatrix}, \tag{2.49}$$

such that the relation becomes

$$\begin{bmatrix} E_{li} \\ E_{ri} \end{bmatrix} = \mathbf{L}_i \begin{bmatrix} E'_{li} \\ E'_{ri} \end{bmatrix}. \tag{2.50}$$

The matrices $\mathbf{H}_{ij}$ and $\mathbf{L}_i$ of Eqs. (2.45) and (2.49) for the entire stack of N layers are then combined into a single stack matrix

$$\mathbf{H}_{12}\mathbf{L}_2 \ldots \mathbf{H}_{N-2,N-1}\mathbf{L}_{N-1}\mathbf{H}_{N-1,N} = \mathbf{S}_{1N} = \begin{bmatrix} S_{11} & S_{12} \\ S_{21} & S_{22} \end{bmatrix}, \tag{2.51}$$

which describes the relation between the fields in the incident layer, 1, and the final layer, N, through the equation

$$\begin{bmatrix} E'_{l1} \\ E'_{r1} \end{bmatrix} = \mathbf{S}_{1N} \begin{bmatrix} E_{lN} \\ E_{rN} \end{bmatrix}. \tag{2.52}$$

Since layer N is the final layer of the stack $E_{lN} = 0$, and as such $E'_{l1} = S_{12}E_{rN}$ and $E'_{r1} = S_{22}E_{rN}$. Thus the final reflectance of the entire system is found as

$$R = \left| \frac{E'_{l1}}{E'_{r1}} \right|^2 = \left| \frac{S_{12}}{S_{22}} \right|^2, \tag{2.53}$$

and the transmittance is found as

$$T = \left| \frac{E'_{rN}}{E'_{r1}} \right|^2 = \left| \frac{1}{S_{22}} \right|^2. \tag{2.54}$$

[28, pp. 295-300]

2.3 The Dyadic Green's Function

In this section we shall consider a solution to an inhomogeneous differential equation. The solution we find is known as the dyadic Green's function. The Green's function plays an important role in solving electromagnetic scattering problems, as the electromagnetic wave equation is a linear partial differential equation. As such this and the following sections lead towards a description of the required equations for solving an electromagnetic scattering problem such as the one for the groove structures under consideration in the present work. Consider an inhomogeneous differential equation of the form

$$\mathcal{L}\mathbf{A}(\mathbf{r}) = \mathbf{B}(\mathbf{r}). \tag{2.55}$$

Here $\mathcal{L}$ is a linear operator acting on the vector field $\mathbf{A}(\mathbf{r})$ to give another vector field $\mathbf{B}(\mathbf{r})$. A general solution to this problem can be constructed as the sum of the homogeneous solution of Eq. (2.55) and a particular inhomogeneous solution. For the purpose of finding a particular inhomogeneous solution we consider the following inhomogeneous equation

$$\mathcal{L}\mathbf{G}_i(\mathbf{r},\mathbf{r}') = \mathbf{n}_i\delta(\mathbf{r}-\mathbf{r}'), \qquad i = x, y, z. \tag{2.56}$$

In this case the inhomogeneous part of the equation is a Kronecker delta function $\delta(\mathbf{r}-\mathbf{r}')$. This function is defined such that it is zero everywhere except at the point $\mathbf{r} = \mathbf{r}'$, where it has the value 1. In this case $\mathbf{G}_i(\mathbf{r},\mathbf{r}')$ is the solution of the operator $\mathcal{L}$, and $\mathbf{n}_i$ is a constant unit vector. Here we shall write the three equations of Eq. (2.56) as

$$\mathcal{L}\overleftrightarrow{\mathbf{G}}(\mathbf{r},\mathbf{r}') = \overleftrightarrow{\mathbf{I}}\,\delta(\mathbf{r}-\mathbf{r}'), \tag{2.57}$$

where $\mathcal{L}$ operates on each column of the dyadic Green's function, $\overleftrightarrow{\mathbf{G}}$, and $\overleftrightarrow{\mathbf{I}}$ is the unit dyad given as

$$\overleftrightarrow{\mathbf{I}} = \hat{x}\hat{x} + \hat{y}\hat{y} + \hat{z}\hat{z}. \tag{2.58}$$

If we have the solution of $\overleftrightarrow{\mathbf{G}}$, we can postmultiply Eq. (2.57) with $\mathbf{B}(\mathbf{r}')$ and integrate over the volume to get

$$\int_V \mathcal{L}\overleftrightarrow{\mathbf{G}}(\mathbf{r},\mathbf{r}')\cdot\mathbf{B}(\mathbf{r}')dV' = \int_V \mathbf{B}(\mathbf{r}')\delta(\mathbf{r}-\mathbf{r}')dV'. \tag{2.59}$$

Due to the property of the delta function the right hand side reduces to $\mathbf{B}(\mathbf{r})$. It then follows from Eq. (2.55) that

$$\mathbf{A}(\mathbf{r}) = \int_V \overleftrightarrow{\mathbf{G}}(\mathbf{r},\mathbf{r}')\cdot\mathbf{B}(\mathbf{r}')dV'. \tag{2.60}$$

Thus we see that the dyadic Green's function plays an important role in finding the solution of an inhomogeneous differential equation such as the wave equation. [25, pp. 25-26]

2.4 Construction of a Two-Dimensional Green's Function

In this section we consider how to construct a two-dimensional Green's function for a layered structure in the xy plane. This is done in order to provide a simple introduction to the main ideas behind the periodic Green's function, which is described in the next section. The construction of the Green's function is done through mode expansion. This concept can be understood in a quantum mechanical formalism, where we seek to construct a Green's function G, which meets the requirement that when an operator $\widehat{H}$ acts on it, the result is -1, i.e

$$\widehat{H}G = -1. \tag{2.61}$$

Using the same operator $\widehat{H}$ we consider the construction of wavefunctions through the eigenvalue problem

$$\widehat{H}\varphi_n = \lambda_n|\varphi\rangle. \tag{2.62}$$

The complete set of wavefunctions,

$$|\varphi\rangle = \sum_m |\varphi_m\rangle a_m, \tag{2.63}$$

is a solution to the stated eigenvalue problem, where we have that the wavefunctions are linearly independent and orthogonal. The linear independence and orthogonality of the wavefunctions entails that

$$\int \varphi_n(\mathbf{r})^* \varphi_m(\mathbf{r}) d^3r = \langle \varphi_n | \varphi_m \rangle = \delta_{nm} N_n, \tag{2.64}$$

where N_n is a normalization constant and δ_{nm} is the Kronecker delta function. We now consider the operator

$$\widehat{A} = \sum_n \frac{|\varphi_n\rangle\langle\varphi_n|}{N_n}. \tag{2.65}$$

We see that with the way the wavefunctions, φ, are constructed, $\widehat{A}$ operating on φ returns the wavefunctions themselves, i.e

$$\widehat{A}|\varphi\rangle = \sum_n \frac{1}{N_n} |\varphi_n\rangle\langle\varphi_n| \sum_m |\varphi_m\rangle a_m = \sum_n a_n |\varphi_n\rangle, \tag{2.66}$$

which demonstrates that $\widehat{A}$ is a unit operator,

$$\widehat{A} = \sum_n \frac{|\varphi_n\rangle\langle\varphi_n|}{N_n} = 1. \tag{2.67}$$

We then see that a Green's function fulfilling Eq. (2.61) can be constructed as

$$G = -\sum_n \frac{|\varphi_n\rangle\langle\varphi_n|}{N_n \lambda_n}, \tag{2.68}$$

where the division by the eigenvalue λ_n is included because our operator returns an eigenvalue when it operates on G.

We may now use this concept for the construction of the Green's function used in electromagnetic scattering problems. That is we construct the Green's function as a sum of modes where each mode, φ_λ, is a solution to the eigenvalue problem,

$$(\nabla^2 + k_0 \varepsilon_{ref})\varphi_\lambda(\mathbf{r}) = \lambda \varphi_\lambda(\mathbf{r}), \tag{2.69}$$

which leads to

$$(\nabla^2 + k^2)\varphi_{\mathbf{k}}(\mathbf{r}) = 0, \quad k^2 = k_0^2 \varepsilon_{ref} - \lambda_{\mathbf{k}}, \tag{2.70}$$

with λ being the eigenvalue to the eigenfunction φ_λ. The complete set of solutions for the eigenvalue problem is of the form $\varphi_{\mathbf{k}}(\mathbf{r}) = e^{-i\mathbf{k}\cdot\mathbf{r}}$ and as such we can write

$$\int \varphi_{\mathbf{k}}(\mathbf{r})\varphi_{\mathbf{k}'}(\mathbf{r})^* d^2r = N_{\mathbf{k}}\delta(\mathbf{k}-\mathbf{k}') = \int e^{i(\mathbf{k}-\mathbf{k}')\cdot\mathbf{r}} d^2r = (2\pi)^2 \delta(k_x' - k_x)\delta(k_y' - k_y), \tag{2.71}$$

where we find the normalization constant as $N_{\mathbf{k}} = (2\pi)^2$. For a derivation of this see appendix A.2. Recalling that our Green's function should satisfy

$$\left(\frac{\partial^2}{\partial x^2} + \frac{\partial^2}{\partial y^2} + k_0\varepsilon_{ref}(\mathbf{r})\right) G(\mathbf{r}, \mathbf{r}') = -\delta(\mathbf{r}, \mathbf{r}'), \tag{2.72}$$

we may construct our Green's function as

$$G(\mathbf{r}, \mathbf{r}') = -\int_{\mathbf{k}} \frac{\varphi_{\mathbf{k}}(\mathbf{r})\varphi_{\mathbf{k}}(\mathbf{r}')^*}{N_{\mathbf{k}}\lambda_{\mathbf{k}}} d^2k = -\int \frac{e^{-i\mathbf{k}\cdot\mathbf{r}} e^{+i\mathbf{k}\cdot\mathbf{r}'}}{(2\pi)^2(k_0^2\varepsilon_{ref} - k^2)} d^2k. \tag{2.73}$$

Here we add a small imaginary part, $i\epsilon$, in the denominator of the Green's function. Doing so simply adds a homogeneous solution to Eq. (2.72), but it ensures that the Green's function satisfies the radiating boundary condition. The Green's function is then written as

$$G(\mathbf{r}, \mathbf{r}') = -\int \frac{e^{-i\mathbf{k}\cdot\mathbf{r}} e^{+i\mathbf{k}\cdot\mathbf{r}'}}{(2\pi)^2(k_0^2\varepsilon_{ref} - k^2 - i\epsilon)} d^2k, \tag{2.74}$$

which we may decompose and write as

$$G(\mathbf{r}, \mathbf{r}') = -\int \frac{e^{-ik_x(x-x')} e^{-ik_y(y-y')}}{(2\pi)^2(\sqrt{k_0^2\varepsilon_{ref} - k_x^2 - i\epsilon} - k_y)(\sqrt{k_0^2\varepsilon_{ref} - k_x^2 - i\epsilon} + k_y)} dk_x dk_y, \tag{2.75}$$

where we have used that

$$k_0^2\varepsilon_{ref} - k^2 - i\epsilon = (\sqrt{k_0^2\varepsilon_{ref} - k_x^2 - i\epsilon} - k_y)(\sqrt{k_0^2\varepsilon_{ref} - k_x^2 - i\epsilon} + k_y). \tag{2.76}$$

We now evaluate the integral over k_y by integrating over a closed curve in the complex half-plane using the residue theorem,

$$\oint \frac{f(z)}{z - z_0} dz = -i2\pi f(z_0). \tag{2.77}$$

We then get that our Green's function can be constructed as

$$\begin{aligned} g(\mathbf{r}, \mathbf{r}') &= \frac{i2\pi}{(2\pi)^2} \int \frac{e^{-ik_x(x-x')} e^{-i\sqrt{k_0^2\varepsilon - k_x^2}|y-y'|}}{2\sqrt{k_0^2\varepsilon - k_x^2}} dk_x \\ &= \frac{i}{2\pi} \int_{-\infty}^{\infty} \frac{e^{-ik_x(x-x')} e^{-ik_y|y-y'|}}{2k_y} dk_x, \quad k_y = \sqrt{k_0^2\varepsilon - k_x^2}. \end{aligned} \tag{2.78}$$

For a layered structure the incident light will undergo reflection and transmission at each interface. These effects can be incorporated in the Green's function by including Fresnel reflection and transmission coefficients in Eq. (2.78). [29, pp. 24-27]

2.5 Construction of the Periodic Green's Function

In this section we consider the construction of a periodic Green's function, which is an essential part for the solution of periodic scattering problems such as those under consideration in this thesis. The construction of the periodic Green's function follows the same overall approach as used in the previous section. The Green's function should still satisfy

$$(\nabla^2 + k_0\varepsilon_{ref})G(\mathbf{r}, \mathbf{r}') = -\delta(\mathbf{r}, \mathbf{r}'), \tag{2.79}$$

as well as the radiating boundary condition in the direction where the structure is not periodic. However, the constructed Green's function should now take into account the underlying periodicity of the structure in question. This is done through the Bloch boundary condition. For a structure with a periodicity along the x direction, we require our Green's function to satisfy the Bloch boundary condition $g(x+\Lambda, y; x', y') = g(x, y; x', y') \exp(-ik_x\Lambda)$, where Λ is the period of the structure and k_x is the Bloch wave number. Once more we seek solutions to the eigenvalue problem

$$(\nabla^2 + k_0\varepsilon_{ref})\varphi_\lambda(\mathbf{r}) = \lambda\varphi_\lambda(\mathbf{r}). \tag{2.80}$$

Here, however, the solutions should also satisfy the periodic boundary condition, $\varphi_\lambda(x + \Lambda, y) = \varphi_\lambda(x, y)\exp(ik_x\Lambda)$. For this problem we have eigenfunctions of the form

$$E_{n,k_y}(\mathbf{r}) = e^{-i(k_x - nG)x}e^{-ik_y y}, \tag{2.81}$$

where inserting this eigenfunction into Eq. (2.80) leads to the eigenvalue $\lambda_{n,k_y} = k_0^2\varepsilon_{ref} - (k_x - nG) - k_y^2$, with $G = 2\pi/\Lambda$ and n being an integer. We find the normalization constant through

$$\begin{aligned} N_{n,k_y}\delta_{nm}\delta(k_y - k_y') &= \int_{x=0}^{x=\Lambda}\int_{y=-\infty}^{y=\infty} \varphi_{n',k_y'}(\mathbf{r})(\varphi_{n,k_y}(\mathbf{r}))^* dxdy \\ &= \int_{x=0}^{x=\Lambda}\int_{y=-\infty}^{y=\infty} e^{-iG(n-m)x}e^{-i(k_y-k_y')y}dxdy \\ &= \Lambda 2\pi\delta_{nm}\delta(k_y - k_y'), \end{aligned} \tag{2.82}$$

and thus we see that $N_{n,k_y} = 2\pi\Lambda$. For a detailed derivation see Appendix A.2. The Green's function is now constructed through mode expansion as

$$\begin{aligned} G(\mathbf{r}, \mathbf{r}') &= \sum_n \int_{k_y} \frac{\varphi_{n,k_y}(\mathbf{r})(\varphi_{n,k_y}(\mathbf{r}'))^*}{N_{n,k_y}\lambda_{n,k_y}} dk_y \\ &= \sum_n \int_{k_y} \frac{e^{-i(k_x-nG)(x-x')}e^{-ik_y(y-y')}}{(2\pi)\Lambda(k_0^2\varepsilon_{ref} - (k_x - nG)^2 - k_y^2)}. \end{aligned} \tag{2.83}$$

Here we again add a small imaginary part, $i\epsilon$, in order for the Green's function to satisfy the radiating boundary condition such that we get

$$\begin{aligned} G(\mathbf{r}, \mathbf{r}') &= \sum_n \int_{k_y} \frac{e^{-i(k_x-nG)(x-x')}e^{-ik_y(y-y')}}{(2\pi)\Lambda(k_0^2\varepsilon_{ref} - (k_x - nG)^2 - k_y^2 - i\epsilon)} \\ &= \sum_n \int_{k_y} \frac{e^{-i(k_x-nG)(x-x')}e^{-ik_y(y-y')}}{(2\pi)\Lambda(\sqrt{k_x^2\varepsilon_{ref} - (k_x - nG)^2 - i\epsilon} - k_y)(\sqrt{k_x^2\varepsilon_{ref} - (k_x - nG)^2 - i\epsilon} + k_y)}. \end{aligned} \tag{2.84}$$

Using the residue theorem we integrate in both the upper and lower complex half-plane and find that our periodic Green's function can be constructed as

$$G(\mathbf{r}, \mathbf{r}') = \frac{-i}{2\Lambda}\sum_n \frac{e^{-i(k_x-nG)(x-x')}e^{-ik_y(y-y')}}{\sqrt{k_{y,n}}}, \tag{2.85}$$

with $k_{y,n} = \sqrt{k_0^2\varepsilon_{ref} - (k_x - nG)^2}$. [29, pp. 36-37]

2.6 2D Green's Function Surface Integral Equation Method

In this section the basics of the Green's Function Surface Integral Equation Method (GFSIEM) are outlined. The GFSIEM is a powerful method for the determination of electric and magnetic fields at any given position in a scattering configuration. The strength of the GFSIEM [30] has been demonstrated in several applications ranging from simple scattering configurations [19–24] to more complex periodic structures [31, 32]. In the GFSIEM the electric and magnetic fields are determined through a simple identity which relates the fields to a simple overlap integral between a Green's function and the normal derivatives of the fields at the surface of the scattering object. The focus of this section is therefore to arrive at these identities. In order to do this a scattering configuration as shown in Fig. 2.4 is considered.

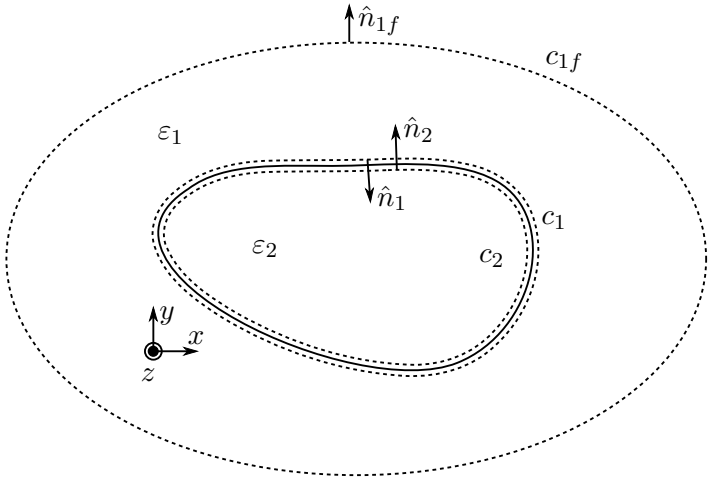

Figure 2.4. A scattering configuration in which a scatterer with dielectric constant ε_2 is surrounded by a material with dielectric constant ε_1. Here the dashed curves of c_1, c_2, and c_{1f} represent imaginary curves with normal vectors $\hat{n}_1$, $\hat{n}_2$, and $\hat{n}_{1f}$.

Here we shall consider the incident field being p polarized such that the $\mathbf{H}$ field purely has a z component

$$\mathbf{H} = \hat{z}H(x, y). \tag{2.86}$$

The choice to consider either s or p polarized light has the important consequence of reducing the problem to requiring only the consideration of one scalar field component. As explained in Sec. 2.3 the Green's function used in the overlap integral is constructed such that it satisfies

$$(\nabla^2 + k_0\varepsilon_i)g(\mathbf{r}, \mathbf{r}') = -\delta(\mathbf{r}, \mathbf{r}'), \tag{2.87}$$
$$(\nabla'^2 + k_0\varepsilon_i)g(\mathbf{r}, \mathbf{r}') = -\delta(\mathbf{r}, \mathbf{r}'), \tag{2.88}$$

where $\nabla^2 = \frac{\partial^2}{\partial x^2} + \frac{\partial^2}{\partial y^2}$ and $\nabla'^2 = \frac{\partial^2}{\partial x'^2} + \frac{\partial^2}{\partial y'^2}$. A Green's function that satisfies these conditions is

$$g_i(\mathbf{r}, \mathbf{r}') = \frac{1}{4i}H_0^{(2)}(k_0 n_i|\mathbf{r} - \mathbf{r}'|). \tag{2.89}$$

This Green's function has been chosen such that it satisfies the radiating boundary condition, entailing that the scattered field propagates away from the scatterer. A requirement for the magnetic field is that it satisfies

$$(\nabla^2 + k_0\varepsilon_i)\mathbf{H}(\mathbf{r}) = 0. \tag{2.90}$$

If we now consider the field at a point inside the imaginary surface c_2 we propose that we can write the field identity as

$$H(\mathbf{r}) = \oint_{c_2} \{(\hat{n}_2' \cdot \boldsymbol{\nabla}' H(\mathbf{r}'))g_2(\mathbf{r},\mathbf{r}') - (\hat{n}_2' \cdot \boldsymbol{\nabla}' g_2(\mathbf{r},\mathbf{r}'))H(\mathbf{r}')\} dl'. \tag{2.91}$$

The first step in deriving Eq. (2.91) is to convert the surface integral on the right hand side to an area integral. This is done simply by using Gauss' theorem. That is we use the relation $\oint \hat{n} \cdot \mathbf{f}(\mathbf{r}) dl = \int \boldsymbol{\nabla} \cdot \mathbf{f}(\mathbf{r}) dA$. We then get that the right hand side of Eq. (2.91) can be written as

$$\begin{aligned}
&\int_{A=\Omega 2} \left\{ \boldsymbol{\nabla}' \cdot \left((\boldsymbol{\nabla}' H(\mathbf{r}'))g_2(\mathbf{r},\mathbf{r}') - H(\mathbf{r}')(\boldsymbol{\nabla}' g_2(\mathbf{r},\mathbf{r}')) \right) \right\} dA' \\
&= \int_{A=\Omega 2} \{ \underbrace{(\nabla^2 H(\mathbf{r}'))}_{-k_0\varepsilon H(\mathbf{r}')} g_2(\mathbf{r},\mathbf{r}') + \boldsymbol{\nabla}' H(\mathbf{r}') \cdot \boldsymbol{\nabla}' g_2(\mathbf{r},\mathbf{r}') \\
&\quad - \boldsymbol{\nabla}' H(\mathbf{r}') \cdot \boldsymbol{\nabla}' g_2(\mathbf{r},\mathbf{r}') - \underbrace{H(\mathbf{r}')\boldsymbol{\nabla}'^2 g_2(\mathbf{r},\mathbf{r}')}_{(-k_0^2\varepsilon g_2(\mathbf{r},\mathbf{r}') - \delta(\mathbf{r}-\mathbf{r}'))H(\mathbf{r}')} \} dA'.
\end{aligned} \tag{2.92}$$

After the cancellation of terms we are left with

$$\int_{A=\Omega 2} H(\mathbf{r}')\delta(\mathbf{r}-\mathbf{r}')dA', \tag{2.93}$$

which is exactly equal to $H(\mathbf{r})$ due to the integration over the delta function only giving a non-zero value for $\mathbf{r} = \mathbf{r}'$. If we consider a position enclosed by the curves c_1 and c_{1f}, we find in a similar fashion that

$$H(\mathbf{r}) = \oint_{c_1 + c_{1f}} \{(\hat{n}_1' \cdot \boldsymbol{\nabla}' H(\mathbf{r}'))g_1(\mathbf{r},\mathbf{r}') - (\hat{n}_1' \cdot \boldsymbol{\nabla}' g_1(\mathbf{r},\mathbf{r}'))H(\mathbf{r}')\} dl'. \tag{2.94}$$

Here we choose c_{1f} to be far away from the scatterer. Far away from the scatterer the total field should be equal to a sum of the incident field and the scattered field, $H(\mathbf{r}) = H_0(\mathbf{r}) + H_{scat}(\mathbf{r})$, where the scattered field in accordance with the radiating boundary condition is on the form $H_{scat}(\mathbf{r}') \approx \frac{1}{\sqrt{r'}} e^{-ikr'} f(\theta')$. We can then look at the integral equation for c_{1f} separately for the incident and scattered fields, H_0 and H_{scat}. For H_0 a similar procedure as Eqs. (2.92)-(2.93) yields

$$H_0(\mathbf{r}) = \oint_{\infty} \{(\hat{n}_\infty' \cdot \boldsymbol{\nabla}' H_0(\mathbf{r}'))g(\mathbf{r},\mathbf{r}') - (\hat{n}_\infty' \cdot \boldsymbol{\nabla}' g(\mathbf{r},\mathbf{r}'))H_0(\mathbf{r}')\} dl', \tag{2.95}$$

entailing that the incident field gives a contribution to the total field outside the scatterer. As for the scattered field we know that in the far field, the Green's function can be approximated as

$$g(\mathbf{r},\mathbf{r}') \approx \frac{e^{-ikr'}}{\sqrt{r'}} f(\mathbf{r},\theta'). \tag{2.96}$$

It then follows

$$\boldsymbol{\nabla}' H_{scat} \approx -ik\frac{\mathbf{r}}{r} f(\theta) H_{scat}(\mathbf{r}), \tag{2.97}$$

$$\boldsymbol{\nabla}' g(\mathbf{r},\mathbf{r}') \approx -ik\frac{\mathbf{r}}{r} g(\mathbf{r},\mathbf{r}'). \tag{2.98}$$

Using both the far field expressions and their derivatives we see that

$$\oint_{\infty} \{(\hat{n}'_{\infty} \cdot \boldsymbol{\nabla}' H_{scat}(\mathbf{r}'))g(\mathbf{r},\mathbf{r}') - (\hat{n}'_{\infty} \cdot \boldsymbol{\nabla}' g(\mathbf{r},\mathbf{r}'))H_{scat}(\mathbf{r}')\} r' d\theta' = 0. \tag{2.99}$$

As such we see that the contribution from the scattered field in region 1 is zero. In a similar manner as before it can be shown for the contribution from c_1 that

$$H(\mathbf{r}) = \oint_{c1} \{(\hat{n}'_1 \cdot \boldsymbol{\nabla}' H(\mathbf{r}'))g_1(\mathbf{r},\mathbf{r}') - (\hat{n}'_1 \cdot \boldsymbol{\nabla}' g_1(\mathbf{r},\mathbf{r}'))H(\mathbf{r}')\} dl'. \tag{2.100}$$

Combining the results for c_1 and c_{1f} and using $\hat{n}'_2 = -\hat{n}'_1 = \hat{n}'$ we end up with an integral equation describing the field outside the scatterer given as

$$H(\mathbf{r}) = H_0(\mathbf{r}) - \oint \{(\hat{n}' \cdot \boldsymbol{\nabla}' H(\mathbf{r}'))g_1(\mathbf{r},\mathbf{r}') - (\hat{n}' \cdot \boldsymbol{\nabla}' g_1(\mathbf{r},\mathbf{r}'))H(\mathbf{r}')\} dl' \quad r \in \Omega_1. \tag{2.101}$$

While Eqs. (2.91) and (2.101) accurately describe the fields inside and outside the scatterer, respectively, they contain four unknowns. As such they have to be treated further to reduce the amount of unknowns in order to simplify the problem. To do this we let the two imaginary surfaces approach the scattering surface until they are infinitesimally close. We can equate the normal derivatives of the magnetic field for each side by using the fact that the tangential components of the electric field must be continuous across the interface. From Maxwell's equations we have that

$$\boldsymbol{\nabla} \times \mathbf{H} = \frac{\partial \mathbf{D}}{\partial t} = i\omega\varepsilon_0\varepsilon\mathbf{E} = \left(\hat{n}\frac{\partial}{\partial n} - \hat{t}\frac{\partial}{\partial t}\right) \times (\hat{z}H), \tag{2.102}$$

where the cross product of the tangential derivative and the field vanishes. We then find

$$i\omega\varepsilon_0\varepsilon E_t = \frac{\partial H}{\partial n} = \hat{n} \cdot \boldsymbol{\nabla} H \Rightarrow \frac{1}{\varepsilon_1}\hat{n} \cdot \boldsymbol{\nabla} H_{\Omega 1} = \frac{1}{\varepsilon_2}\hat{n} \cdot \boldsymbol{\nabla} H_{\Omega 2}. \tag{2.103}$$

Using this boundary condition we find

$$H(\mathbf{r}) = H_0(\mathbf{r}) - \oint \{(\hat{n}' \cdot \boldsymbol{\nabla}' H_{\Omega 1}(\mathbf{r}'))g_1(\mathbf{r},\mathbf{r}') - (\hat{n}' \cdot \boldsymbol{\nabla}' g_1(\mathbf{r},\mathbf{r}'))H_{\Omega 1}(\mathbf{r}')\} dl' \quad r \in \Omega_1, \tag{2.104}$$

$$H(\mathbf{r}) = \oint \{(\hat{n}' \cdot \boldsymbol{\nabla}' H_{\Omega 1}(\mathbf{r}'))\frac{\varepsilon_2}{\varepsilon_1} g_2(\mathbf{r},\mathbf{r}') - (\hat{n}' \cdot \boldsymbol{\nabla}' g_2(\mathbf{r},\mathbf{r}'))H_{\Omega 1}(\mathbf{r}')\} dl' \quad r \in \Omega_2. \tag{2.105}$$

These equations describing the field can be solved by discretizing the scattering surface into N small curve segments. This results in N sets of equations in which the fields and their normal derivatives are the only unknowns. In each of these segments the fields and their normal derivatives are assumed constant. The resulting set of equations can easily be solved when formulated as a matrix in the form of

$$\begin{bmatrix} \overline{H_0} \\ 0 \end{bmatrix} = \begin{bmatrix} \frac{1}{2}\overline{\overline{I}} - \overline{\overline{B}}^{(1)} & \overline{\overline{A}}^{(1)} \\ \frac{1}{2}\overline{\overline{I}} + \overline{\overline{B}}^{(2)} & -\overline{\overline{A}}^{(2)} \end{bmatrix} \begin{bmatrix} \overline{H} \\ \overline{\phi} \end{bmatrix}, \tag{2.106}$$

where $\overline{\overline{A}}^{(n)}$ and $\overline{\overline{B}}^{(n)}$ are matrices, in which the elements are given as

$$A_{i,j}^{(1)} = P\int_j g_1(s_i, s')dl', \tag{2.107}$$

$$B_{i,j}^{(1)} = P\int_j \hat{n}' \cdot \boldsymbol{\nabla}' g_1(s_i, s')dl', \tag{2.108}$$

$$A_{i,j}^{(2)} = \frac{\varepsilon_2}{\varepsilon_1} P\int_j g_2(s_i, s')dl', \tag{2.109}$$

$$B_{i,j}^{(2)} = P\int_j \hat{n}' \cdot \boldsymbol{\nabla}' g_2(s_i, s')dl'. \tag{2.110}$$

Here s_i is a position on the i'th curve segment. The P's in Eqs. (2.107)-(2.110) indicate that the integrals must be calculated as principal value integrals. These integrals are calculated numerically as sums in which the singular point of the integrand is excluded from the integral. The elements $\frac{1}{2}\overline{\overline{I}}$ in Eq. (2.106) arise from an approximation to the Green's function, which is used when $\mathbf{r} = \mathbf{r}'$. An explanation of this is given in Appendix A.5. [29, pp. 15-21]

2.7 2D GFSIEM for a General Direction of Light Incidence

In this section we expand the GFSIEM described in the previous section to provide a method for solving scattering problems for a general direction of light incidence, which has not previously been given a lot of attention in the literature. Consider a scattering structure with a surface as shown in Fig. 2.5.

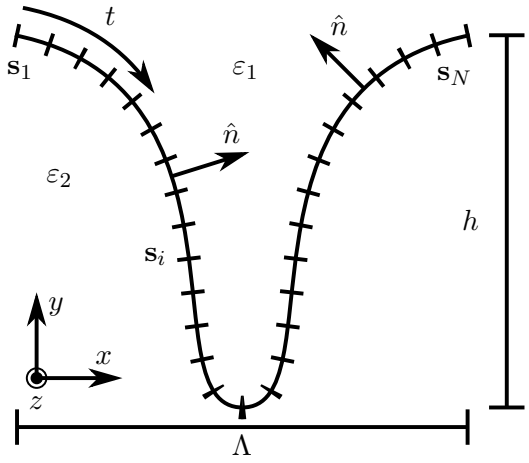

Figure 2.5. The surface of a scattering structure divided into surface elements. For the periodic scattering problem considered here, the figure represents a single period, Λ, of the structure.

For propagation in the xy plane and either s or p polarization the electric or magnetic field will only have a z component, and the other field will be perpendicular to the z axis, which greatly simplifies the problem to a formulation with only one scalar field component as described in previous section. This is no longer the case for a general direction of light incidence. However, as we shall show, the two scalar field components E_z and H_z are sufficient. Due to

the translational invariance along the z axis and periodicity along the x axis the fields can be decomposed into Bloch waves of the form

$$\mathbf{E}(\mathbf{r}) = \mathbf{U}_E(\boldsymbol{\rho}; k_x, k_z)e^{-ik_x x}e^{-ik_z z}, \tag{2.111}$$
$$\mathbf{H}(\mathbf{r}) = \mathbf{U}_H(\boldsymbol{\rho}; k_x, k_z)e^{-ik_x x}e^{-ik_z z}, \tag{2.112}$$

where $\mathbf{U}_{j=E,H}$ is a periodic function satisfying $\mathbf{U}_j(\boldsymbol{\rho}+\hat{x}\Lambda) = \mathbf{U}_j(\boldsymbol{\rho})$ with Λ being the period of the structure, $\boldsymbol{\rho} = \hat{x}x + \hat{y}y$, and $\mathbf{r} = \hat{x}x + \hat{y}y + \hat{z}z$. We see that there are three components for both the magnetic field and the electric field. However, by inserting these expressions for the fields into Maxwell's equations it can be shown that the x and y components of the fields may be described purely from the z components of the magnetic and electric fields, i.e.

$$H_x = \frac{k_0^2\varepsilon}{k_0^2\varepsilon - k_z^2}\left(\frac{i}{\omega\mu_0}\frac{\partial E_z}{\partial y} - \frac{ik_z}{k_0^2\varepsilon}\frac{\partial H_z}{\partial x}\right), \tag{2.113}$$
$$H_y = \frac{k_0^2\varepsilon}{k_0^2\varepsilon - k_z^2}\left(-\frac{i}{\omega\mu_0}\frac{\partial E_z}{\partial x} - \frac{ik_z}{k_0^2\varepsilon}\frac{\partial H_Z}{\partial y}\right), \tag{2.114}$$
$$H_x = \frac{k_0^2\varepsilon}{k_0^2\varepsilon - k_z^2}\left(-\frac{i}{\omega\varepsilon_0\varepsilon}\frac{\partial H_z}{\partial y} - \frac{ik_z}{k_0^2\varepsilon}\frac{\partial E_z}{\partial x}\right), \tag{2.115}$$
$$E_y = \frac{k_0^2\varepsilon}{k_0^2\varepsilon - k_z^2}\left(\frac{i}{\omega\varepsilon_0\varepsilon}\frac{\partial H_z}{\partial x} - \frac{ik_z}{k_0^2\varepsilon}\frac{\partial E_z}{\partial y}\right). \tag{2.116}$$

These in-plane components of $\mathbf{H}$ and $\mathbf{E}$ are expressed in a condensed form as [33]

$$\mathbf{H}_s(\boldsymbol{\rho}) = \frac{-i}{k_s^2}[k_z\boldsymbol{\nabla}_s H_z + \omega\varepsilon_0\varepsilon\hat{z}\times\boldsymbol{\nabla}_s E_z], \tag{2.117}$$
$$\mathbf{E}_s(\boldsymbol{\rho}) = \frac{-i}{k_s^2}[k_z\boldsymbol{\nabla}_s E_z + \omega\mu_0\hat{z}\times\boldsymbol{\nabla}_s E_z], \tag{2.118}$$

where

$$k_s^2 = k_0^2\varepsilon - k_z^2, \tag{2.119}$$
$$\boldsymbol{\nabla}_s = \hat{x}\frac{\partial}{\partial x} + \hat{y}\frac{\partial}{\partial y}. \tag{2.120}$$

The z components of the fields must satisfy the scalar wave equation, i.e.

$$\nabla^2 E_z + k_0^2\varepsilon E_z = \nabla_s^2 E_z + k_s^2 E_z = 0. \tag{2.121}$$

In addition to the electric and magnetic fields, the field due to a point source is considered in each material,

$$(\nabla_s^2 + k_{si}^2)g_i(\boldsymbol{\rho}; \boldsymbol{\rho}') = -\delta(\boldsymbol{\rho} - \boldsymbol{\rho}'). \tag{2.122}$$

Here $k_{si}^2 = k_0^2\varepsilon_i - k_z^2$ with ε_i being the dielectric constant of material i, and g_i is the appropriate Green's function in material i. For a structure with periodicity in the x direction a solution for g_i that satisfies the radiating boundary condition along y and the Bloch boundary condition along x can be constructed through mode expansion (see Sec. 2.5) as

$$g_i(\mathbf{r}, \mathbf{r}') = \frac{-i}{4\pi}\sum_n \frac{e^{-i(k_x - nG)(x-x')}e^{-ik_{yi,n}|y-y'|}}{k_{yi,n}}G. \tag{2.123}$$

Here k_x is the Bloch wave number in the direction in which the structure is periodic, $G = 2\pi/\Lambda$ with Λ being the period of the structure, and $k_{yi,n} = [k_{si}^2 - (kx - nG)^2]^{1/2}$ with $\mathrm{Im}(k_{yi,n}) \leq 0$.

Similar to the case of $k_z = 0$ (see Sec. 2.6) we can obtain the integral equations

$$E_z(\boldsymbol{\rho}) = \begin{cases} E_{z0}(\boldsymbol{\rho}) - \oint \{g_1(\boldsymbol{\rho};\boldsymbol{\rho}')\hat{n}' \cdot \boldsymbol{\nabla}' E_z(\boldsymbol{\rho}') - E_z(\boldsymbol{\rho}')\hat{n}' \cdot \boldsymbol{\nabla}' g_1(\boldsymbol{\rho};\boldsymbol{\rho}')\} dl' & \boldsymbol{\rho} \in \Omega_1 \\ \oint \{g_2(\boldsymbol{\rho};\boldsymbol{\rho}')\hat{n}' \cdot \boldsymbol{\nabla}' E_z(\boldsymbol{\rho}') - E_z(\boldsymbol{\rho}')\hat{n}' \cdot \boldsymbol{\nabla}' g_2(\boldsymbol{\rho};\boldsymbol{\rho}')\} dl' & \boldsymbol{\rho} \in \Omega_2, \end{cases} \tag{2.124}$$

$$H_z(\boldsymbol{\rho}) = \begin{cases} H_{z0}(\boldsymbol{\rho}) - \oint \{g_1(\boldsymbol{\rho};\boldsymbol{\rho}')\hat{n}' \cdot \boldsymbol{\nabla}' H_z(\boldsymbol{\rho}') - H_z(\boldsymbol{\rho}')\hat{n}' \cdot \boldsymbol{\nabla}' g_1(\boldsymbol{\rho};\boldsymbol{\rho}')\} dl' & \boldsymbol{\rho} \in \Omega_1 \\ \oint \{g_2(\boldsymbol{\rho};\boldsymbol{\rho}')\hat{n}' \cdot \boldsymbol{\nabla}' H_z(\boldsymbol{\rho}') - H_z(\boldsymbol{\rho}')\hat{n}' \cdot \boldsymbol{\nabla}' g_2(\boldsymbol{\rho};\boldsymbol{\rho}')\} dl' & \boldsymbol{\rho} \in \Omega_2. \end{cases} \tag{2.125}$$

Here Ω_1 and Ω_2 refer to positions outside and inside the metal, respectively (dielectric constants ε_1 and ε_2), and E_{z0} and H_{z0} are the incident fields. Inserting Eqs. (2.117) and (2.118) into the boundary conditions $\hat{n} \times \mathbf{H}_1 = \hat{n} \times \mathbf{H}_2$ and $\hat{n} \times \mathbf{E}_1 = \hat{n} \times \mathbf{E}_2$ we get (see Appendix A.4)

$$E_{z1} = E_{z2}, \tag{2.126}$$

$$H_{z1} = H_{z2}, \tag{2.127}$$

$$\hat{n} \cdot \boldsymbol{\nabla} H_{z2} = \hat{n} \cdot \boldsymbol{\nabla} H_{z1} \frac{k_0^2\varepsilon_2 - k_z^2}{k_0^2\varepsilon_1 - k_z^2} - \hat{t} \cdot \boldsymbol{\nabla} E_{z1} \frac{k_z}{k_0} \sqrt{\frac{\varepsilon_0}{\mu_0}} \frac{k_0^2(\varepsilon_1 - \varepsilon_2)}{k_0^2\varepsilon_1 - k_z^2}, \tag{2.128}$$

$$\hat{n} \cdot \boldsymbol{\nabla} E_{z2} = \hat{n} \cdot \boldsymbol{\nabla} E_{z1} \frac{\varepsilon_1}{\varepsilon_2} \frac{k_0^2\varepsilon_2 - k_z^2}{k_0^2\varepsilon_1 - k_z^2} - \hat{t} \cdot \boldsymbol{\nabla} H_{z1} \frac{k_z}{k_0} \sqrt{\frac{\mu_0}{\varepsilon_0}} \frac{k_0^2(\varepsilon_2 - \varepsilon_1)}{k_0^2\varepsilon_1 - k_z^2}. \tag{2.129}$$

We see that in the case of $k_z \neq 0$ there is a coupling between H_z and E_z, and if $k_z = 0$ Eqs. (2.128) and (2.129) reduce to $\hat{n} \cdot \boldsymbol{\nabla} H_{z2} = \hat{n} \cdot \boldsymbol{\nabla} H_{z1}\varepsilon_2/\varepsilon_1$ and $\hat{n} \cdot \boldsymbol{\nabla} E_{z2} = \hat{n} \cdot \boldsymbol{\nabla} E_{z1}$, in which case there is no coupling, and it is sufficient to consider each field separately, greatly reducing the complexity of the problem to the case described in Sec. 2.6. In this case the integral equations can be solved by a numerical approach, in which the fields and their normal derivatives are considered constant in each surface element. However, for the case of $k_z \neq 0$ where there is a coupling between H_z and E_z this representation of the fields is inadequate for describing the tangential derivative in Eqs. (2.128) and (2.129). In order to expand the model to account for the tangential derivative, we introduce a linear variation of the fields in each element by combining two weight functions N_1 and N_2 as shown in Fig. 2.6. By combining the weight functions N_1 and N_2 the linear variation of the field between two points with field values A and B will look as shown in the rightmost graph of Fig. 2.6.

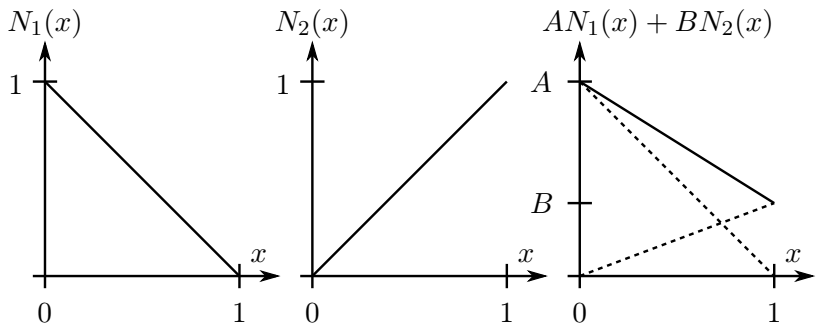

Figure 2.6. The weight functions used in constructing linearly varying fields in each surface element.

The z component of the fields and the z component of their normal derivatives along a surface element may then be described as

$$E_z(\mathbf{s}) = E_z(\mathbf{s}(t)) \approx \sum_{i=1}^{N} E_{z,i}^{(s)} N_1\left(\frac{t-t_i^{(s)}}{L_i}\right) + E_{z,i}^{(e)} N_2\left(\frac{t-t_i^{(s)}}{L_i}\right), \tag{2.130}$$

$$H_z(\mathbf{s}) = H_z(\mathbf{s}(t)) \approx \sum_{i=1}^{N} H_{z,i}^{(s)} N_1\left(\frac{t-t_i^{(s)}}{L_i}\right) + H_{z,i}^{(e)} N_2\left(\frac{t-t_i^{(s)}}{L_i}\right), \tag{2.131}$$

$$\phi_E(\mathbf{s}(t)) = [\hat{n}\cdot\boldsymbol{\nabla} E_z(\mathbf{r})]_{\mathbf{r}=\mathbf{s}(t)} \approx \sum_{i=1}^{N} \phi_{E,i}^{(s)} N_1\left(\frac{t-t_i^{(s)}}{L_i}\right) + \phi_{E,i}^{(e)} N_2\left(\frac{t-t_i^{(s)}}{L_i}\right), \tag{2.132}$$

$$\phi_H(\mathbf{s}(t)) = [\hat{n}\cdot\boldsymbol{\nabla} E_z(\mathbf{r})]_{\mathbf{r}=\mathbf{s}(t)} \approx \sum_{i=1}^{N} \phi_{H,i}^{(s)} N_1\left(\frac{t-t_i^{(s)}}{L_i}\right) + \phi_{H,i}^{(e)} N_2\left(\frac{t-t_i^{(s)}}{L_i}\right), \tag{2.133}$$

where $\mathbf{s} = \mathbf{s}(t)$ is a position along the surface, with t being the distance along the surface from a starting point (see Fig. 2.5), $t_i^{(s)}$ is the start point of element i, L_i is the length of element i, and $E_{z,i}^{(s)}$ and $E_{z,i}^{(e)}$ are the values of E_z in the start and end points of surface element i, respectively. The factor $(t-t_i^{(s)})/L_i$ represents a fractional distance along surface element i.

The tangential derivative, $\hat{t}\cdot\boldsymbol{\nabla} E_z$ at all sampling points $t_i^{(s)}$ given as a column vector $\bar{t}_E$, can then be approximated as the average slope of the field values in neighbouring surface elements,

$$\bar{t}_E = \overline{\overline{T}}\,\bar{E}_z^{(s)}, \tag{2.134}$$

where $\overline{\overline{T}}$ is a matrix constructed from a finite-difference scheme using nearest neighbour sampling points. The concept is illustrated in Fig. 2.7, where the tangential derivative in the point $t_i^{(s)}$ is found as the average slope of the linearly varying fields in the two adjacent surface elements.

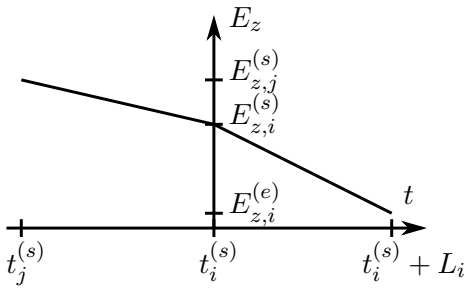

Figure 2.7. Illustration of the finite-difference approach for the tangential derivative.

Using this scheme we approximate the tangential derivative of element i as

$$t_{E,i} = \hat{t} \cdot \boldsymbol{\nabla} E_{z,i} \approx \frac{1}{2}\left(\frac{1}{L_j} - \frac{1}{L_i}\right) E_{z,i}^{(s)} + \frac{1}{2L_i} E_{z,i}^{(e)} - \frac{1}{2L_i} E_{z,j}^{(s)}, \tag{2.135}$$

$$t_{H,i} = \hat{t} \cdot \boldsymbol{\nabla} H_{z,i} \approx \frac{1}{2}\left(\frac{1}{L_j} - \frac{1}{L_i}\right) H_{z,i}^{(s)} + \frac{1}{2L_i} E_{z,i}^{(e)} - \frac{1}{2L_i} H_{z,j}^{(s)}. \tag{2.136}$$

It is then clear that $\overline{\overline{T}}$ is of the form

$$\overline{\overline{T}} = \begin{bmatrix} \frac{1}{2}\left(\frac{1}{L_N} - \frac{1}{L_1}\right) & \frac{1}{2L_1} & 0 & 0 & \dots & \frac{-1}{2L_n} \\ \frac{-1}{2L_1} & \frac{1}{2}\left(\frac{1}{L_2} - \frac{1}{L_1}\right) & \frac{1}{2L_2} & 0 & \dots & 0 \\ \vdots & \vdots & \vdots & \vdots & \ddots & \vdots \\ 0 & \dots & 0 & \frac{-1}{2L_{N-2}} & \frac{1}{2}\left(\frac{1}{L_{N-2}} - \frac{1}{L_{N-1}}\right) & \frac{1}{2L_{N-1}} \\ \frac{1}{2L_N} & 0 & \dots & 0 & \frac{-1}{2L_{N-1}} & \frac{1}{2}\left(\frac{1}{L_{N-1}} - \frac{1}{L_N}\right) \end{bmatrix}. \tag{2.137}$$

Another convenient matrix can be constructed by considering that the end point of surface element i is the start point of element $(i+1)$. That is

$$\overline{E}_z^{(e)} = \overline{\overline{D}}\, \overline{E}_z^{(s)}, \tag{2.138}$$

where $\overline{E}_z^{(s)}$ and $\overline{E}_z^{(s)}$ are column vectors containing all of the values $E_{z,i}^{(s)}$ and $E_{z,i}^{(e)}$, and the matrix $\overline{\overline{D}}$ is of the form

$$\overline{\overline{D}} = \begin{bmatrix} 0 & 1 & 0 & 0 & \dots & 0 \\ 0 & 0 & 1 & 0 & \dots & 0 \\ \vdots & \vdots & \vdots & \vdots & \ddots & \vdots \\ 0 & 0 & 0 & 0 & \dots & 1 \\ 1 & 0 & 0 & 0 & \dots & 0 \end{bmatrix}. \tag{2.139}$$

The matrix describing the magnetic and electric fields governed by Eqs. (2.124) and (2.125) is then constructed as

$$\begin{bmatrix} \overline{E}_{z,0}^{(s)} \\ \overline{0} \\ \overline{H}_{z,0}^{(s)} \\ \overline{0} \end{bmatrix} = \begin{bmatrix} \overline{\overline{B}}_1 & \overline{\overline{A}}_1 & \overline{\overline{0}} & \overline{\overline{0}} \\ \overline{\overline{B}}_2 & -\overline{\overline{A}}_2 f_1 & \overline{\overline{A}}_2 \overline{\overline{T}} f_2 & \overline{\overline{0}} \\ \overline{\overline{0}} & \overline{\overline{0}} & \overline{\overline{B}}_1 & \overline{\overline{A}}_1 \\ \overline{\overline{A}}_2 \overline{\overline{T}} f_4 & \overline{\overline{0}} & \overline{\overline{B}}_2 & -\overline{\overline{A}}_2 f_3 \end{bmatrix} \begin{bmatrix} \overline{E}_z^{(s)} \\ \overline{\phi}_E^{(s)} \\ \overline{H}_z^{(s)} \\ \overline{\phi}_H^{(s)} \end{bmatrix}, \tag{2.140}$$

where

$$f_1 = \frac{\varepsilon_1}{\varepsilon_2}\frac{k_0^2\varepsilon_2 - k_z^2}{k_0^2\varepsilon_1 - k_z^2}, \tag{2.141}$$

$$f_2 = \frac{k_z}{k_0}\frac{1}{\varepsilon_2}\frac{k_0^2(\varepsilon_2 - \varepsilon_1)}{k_0^2\varepsilon_1 - k_z^2}, \tag{2.142}$$

$$f_3 = \frac{k_0^2\varepsilon_2 - k_z^2}{k_0^2\varepsilon_1 - k_z^2}, \tag{2.143}$$

$$f_4 = \frac{k_z}{k_0}\frac{k_0^2(\varepsilon_1 - \varepsilon_2)}{k_0^2\varepsilon_1 - k_z^2}, \tag{2.144}$$

$$\overline{\overline{B}}_1 = \left(\frac{1}{2}\overline{\overline{I}} - \overline{\overline{B}}^{(1,1)} - \overline{\overline{B}}^{(1,2)}\overline{\overline{D}}\right), \tag{2.145}$$

$$\overline{\overline{A}}_1 = \left(\overline{\overline{A}}^{(1,1)} + \overline{\overline{A}}^{(1,2)}\overline{\overline{D}}\right), \tag{2.146}$$

$$\overline{\overline{B}}_2 = \left(\frac{1}{2}\overline{\overline{I}} + \overline{\overline{B}}^{(2,1)} + \overline{\overline{B}}^{(2,2)}\overline{\overline{D}}\right), \tag{2.147}$$

$$\overline{\overline{A}}_2 = \left(\overline{\overline{A}}^{(2,1)} + \overline{\overline{A}}^{(2,2)}\overline{\overline{D}}\right), \tag{2.148}$$

and

$$A_{i,j}^{(u,v)} = P\int g_u(\mathbf{s}_i, \mathbf{s}(t'))N_v\left(\frac{t' - t_j^{(s)}}{L_j}\right)dt', \tag{2.149}$$

$$B_{i,j}^{(u,v)} = P\int [\hat{n}'\cdot\boldsymbol{\nabla}' g_u(\mathbf{s}_i, \mathbf{r}')]_{\mathbf{r}'=\mathbf{s}(t')}N_v\left(\frac{t' - t_j^{(s)}}{L_j}\right)dt'. \tag{2.150}$$

2.8 Thermal Emission

The previous sections contain the theory used to model the reflectance of the periodic groove structures under consideration in this thesis, but there is another important concept to consider if the structures are to be used in TPV or CSP, namely thermal emission. While the thermal emission properties of the structures are not specifically investigated in this thesis, this section contains an introduction to the basic concepts of thermal emission, since it is paramount in the aforementioned applications.

Any material continuously absorbs and emits electromagnetic radiation. Thermal emission is the process by which materials emit electromagnetic radiation. The process is also often called radiative heat transfer or thermal radiation. The radiation emitted in this way is affected by both the type and temperature of the emitting material. The wavelength spectrum of the thermal radiation is highly dependent on the temperature of the emitting material, while the type of material mainly affects the strength of the radiation. Among the three possible methods of heat transfer thermal radiation is unique in that it does not require a medium for its transfer. The other two methods, conduction and convection, both require the presence of a medium. In thermal conduction in solids energy is transferred by free

electrons or phonons, whereas in gases or liquids the transfer occurs through collisions between molecules or atoms. Convection works in a somewhat similar way, only with some of the higher energy molecules being swept away by a flow to be replaced by lower energy molecules.

A further difference between the methods of heat transfer is found in the heat transfer rate or heat flux, q. While the fluxes for conduction and convection are linearly proportional to temperature differences, i.e. $q \propto T_2 - T_1$, the flux for thermal radiation is proportional to differences in temperature to the fourth power, $q \propto T_2^4 - T_1^4$. Thus radiative heat transfer becomes increasingly important at higher temperatures, eventually completely dominating over conduction and convection at very high temperatures.

While these properties make thermal radiation very important in vacuum and high-temperature applications they also tend to complicate the analysis of related problems. Typical ranges for interactions in conduction and convection are on the order of 10^{-9} m, while for thermal radiation the distances can easily span the range of 10^{-10} to 10^{10} m, depending on the situation. Thus conservation of energy cannot be applied to infinitesimal volumes but must instead be applied over the entire volume under consideration, which, in turn, leads to integral equations with up to seven different independent variables. Furthermore, while properties related to conduction and convection are easily measured and often well behaved, radiative properties tend to be difficult to measure and display erratic behaviour as well as being strongly dependent on the wavelength of the radiation. [34, pp. 1-3]

For these reasons the detailed study of thermal radiation is a rather extensive topic, and a thorough description is beyond the scope of this thesis. Instead only the basic principles of thermal emission are described in this section.

In order to describe the basic principles of thermal emission a few terms must be introduced. When electromagnetic radiation propagating through some medium encounters another medium, the wave might be partially or totally reflected, and any remaining part of the wave penetrates into the medium. Materials are classified depending on their interaction with a penetrating electromagnetic wave. If the wave passes through the material without any attenuation the material is called transparent, whereas a material with partial attenuation is called semitransparent. If the wave is partially attenuated but the transmitted light is scattered into many directions the material is instead termed translucent. Any material in which the penetrating electromagnetic wave is completely attenuated is defined as opaque. Materials generally fall into different categories depending on the wavelength of the incident radiation and the thickness of the material. For instance, gold is generally opaque but for extremely thin layers it becomes semitransparent, and while window glass is highly transparent in the visible spectrum it is opaque to both ultraviolet and infrared radiation.

If an opaque surface does not reflect any radiation it is called a perfect absorber or black surface. An object with black surfaces is also typically referred to as a blackbody. While a blackbody absorbs the maximum possible amount of energy it also emits the maximum possible amount of energy. This can be demonstrated by considering an object at a temperature T inside a black-walled enclosure, which is thermally insulated on the outside, such as the

one shown in Fig. 2.8. In accordance with the second law of thermodynamics, the entire system will eventually reach thermal equilibrium, such that the entire enclosure and the object inside are at a single uniform temperature. The object will receive exactly the same amount of energy whether it is black or not, though if it is black it will absorb more energy than it would otherwise. It is evident that in order to reach and maintain thermal equilibrium the object must emit the same amount of energy as it absorbs, i.e. in the case of a blackbody the maximum possible amount. This principle is called Kirchhoff's law. Since the blackbody absorbs the same amount of energy regardless of the direction of incidence, it must also emit the same amount of energy in all directions. [34, pp. 4-5]

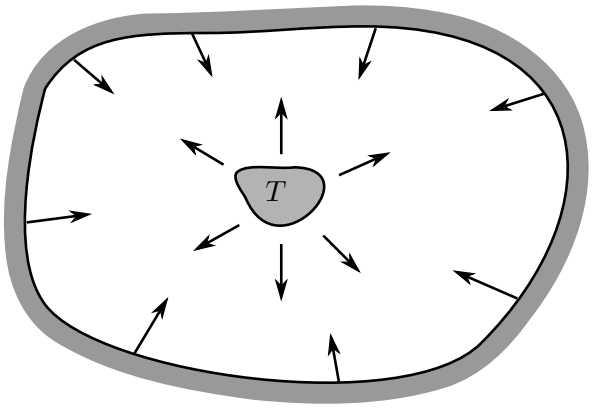

Figure 2.8. An object inside a thermally insulated black-walled enclosure used to illustrate Kirchhoff's law. Inspired by [34, p. 5].

When describing thermal radiation the heat flux emitted from a surface is referred to as emissive power, which is typically described as either spectral emissive power, E_ν, or total emissive power, E. The spectral emissive power is given as emitted energy per unit time per unit area per unit frequency (hence the subscript ν for frequency), while the total emissive power is the heat flux across the entire frequency spectrum. The relationship between E_ν and E is simply

$$E(T) = \int_0^\infty E_\nu(T, \nu) d\nu. \tag{2.151}$$

Max Planck showed in 1901 that the spectral emissive power distribution for a blackbody at a given temperature T surrounded by vacuum is given as

$$E_{b\nu}(T, \nu) = \frac{2\pi h \nu^3}{c^2(e^{h\nu/k_B T} - 1)}, \tag{2.152}$$

which is commonly referred to as Planck's law. Here h is Planck's constant, k_B is Boltzmann's constant, and c is the speed of light in vacuum. Eq. (2.152) can be expressed in terms of the wavelength in vacuum, λ_0, by using the relationships

$$\nu = \frac{c}{\lambda_0}, \tag{2.153}$$

$$d\nu = -\frac{c}{\lambda_0^2} d\lambda_0, \tag{2.154}$$

$$E_b(T) = \int_0^\infty E_{b\nu} d\nu = \int_0^\infty E_{b\lambda} d\lambda_0. \tag{2.155}$$

Using these relationships Eq. (2.152) can be rewritten as

$$E_{b\lambda}(T, \lambda_0) = \frac{2\pi hc^2}{\lambda_0^5(e^{hc/\lambda_0 k_B T} - 1)}. \tag{2.156}$$

Eq. (2.156) shows that an increasing temperature increases the overall level of emission, and that the peak of maximum emission shifts towards shorter wavelengths. Introducing the constants $C_1 = 2\pi hc^2$ and $C_2 = hc/k_B$ allows for Eq. (2.156) to be rewritten as

$$\frac{E_{b\lambda}}{T^5} = \frac{C_1}{(\lambda_0 T)^5(e^{C_2/n\lambda T} - 1)}, \tag{2.157}$$

which is a function of only $\lambda_0 T$. From this equation the scaled emissive power can be plotted simply as a function of the product of the wavelength in vacuum, λ_0, and the temperature, T. This function is plotted in Fig. 2.9.

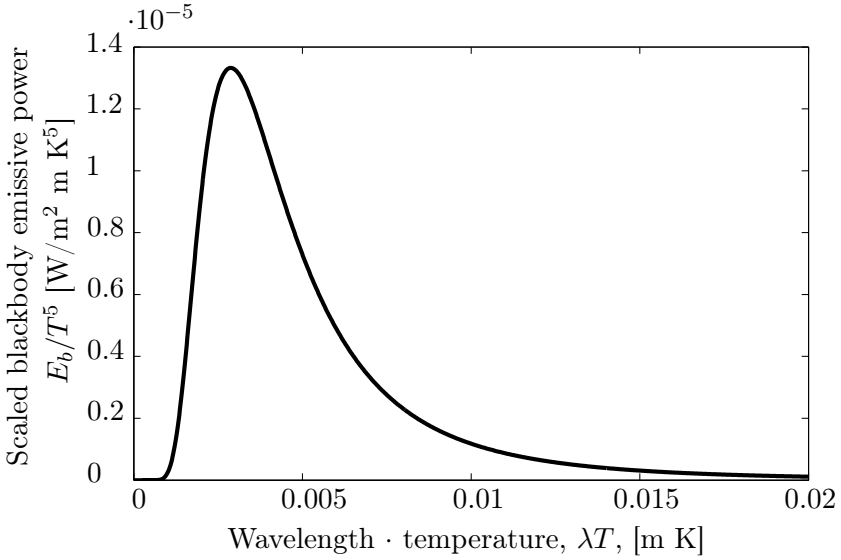

Figure 2.9. Scaled blackbody emissive power as a function of the product of the wavelength in vacuum and temperature.

The maximum of the curve can be found by simply differentiating Eq. (2.157), which solved numerically gives

$$(\lambda_0 T)_{\max} = C_3 = 2898 \cdot 10^{-6} \text{ m K}. \tag{2.158}$$

Eq. (2.158) is called Wien's displacement law and allows for easy determination of the wavelength of maximum emission for a blackbody at a temperature T in vacuum.

From Eq. (2.155) it is evident that the total emissive power of a blackbody may be determined by integrating Eq. (2.156) over the entire wavelength spectrum. The integration results in

$$E_b(T) = \sigma T^4, \tag{2.159}$$

where $\sigma = \pi^4 C_1/15C_2^4$ is the Stefan-Boltzmann constant. Another value, which is often of interest, is the fraction of emissive power within a certain wavelength range. This is typically described in terms of the fraction of emissive power in the interval of 0 to $\lambda_0 T$,

$$f(\lambda_0 T) = \frac{\int_0^{\lambda_0} E_{b\lambda} d\lambda_0}{E_b(T)}. \tag{2.160}$$

With this definition the fraction of emissive power in the wavelength range of λ_1 to λ_2 is found as

$$\int_{\lambda_1}^{\lambda_2} E_{b\lambda} d\lambda_0 = [f(\lambda_2 T) - f(\lambda_1 T)]\sigma T^4. \tag{2.161}$$

As an example of the usage of Eqs. (2.158) and (2.161), it is found by treating the sun as a blackbody at a temperature of $T = 5777$ K (which is a reasonable approximation) that its maximum emissive power is at a wavelength of $\lambda_{\text{max,sun}} \approx 500$ nm, and roughly 37 % of its total emission lies in the visible spectrum between $\lambda_1 = 400$ nm and $\lambda_2 = 700$ nm. [34, pp. 6-11]

A commonly used term in the description of thermal radiation is the radiative intensity, which is simply the energy flow per unit solid angle per unit area normal to the rays. A solid angle is the projection of an area onto a unit hemisphere centred in a reference point. Similar to the case of emissive power a distinction is made between spectral and total intensity, I_λ and I, which are related by

$$I(\mathbf{r}, \hat{\mathbf{s}}) = \int_0^\infty I_\lambda(\mathbf{r}, \hat{\mathbf{s}}, \lambda_0) d\lambda_0. \tag{2.162}$$

In this expression $\mathbf{r}$ is a vector describing a location in space, and $\hat{\mathbf{s}}$ is a unit vector in the direction from the surface of the emitter to the point described by $\mathbf{r}$. The intensity can be converted to emissive power by integrating over all directions from the surface. An expression for this can be developed by considering a geometry as illustrated in Fig. 2.10. In this figure dA is a small area of the surface of the emitter, and $dA_p = dA\cos\theta$ is the projection of dA onto a plane normal to the direction $\hat{\mathbf{s}}$. dA_p thus describes the way dA is seen when viewed from the direction $-\hat{\mathbf{s}}$.

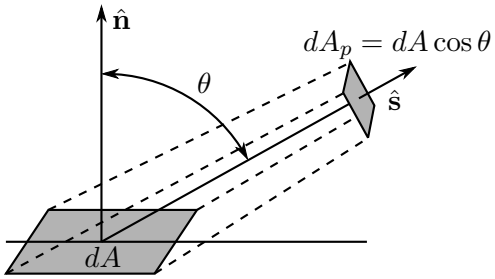

Figure 2.10. The geometry used to relate the blackbody emissive power to the intensity. Inspired by [34, p. 14].

The energy emitted from dA in the direction $\hat{\mathbf{s}}$ within a small solid angle $d\Omega = \sin\theta d\theta d\phi$ is found as

$$I(\mathbf{r}, \hat{\mathbf{s}}) dA_p d\Omega = I(\mathbf{r}, \hat{\mathbf{s}}) dA \cos\theta \sin\theta d\theta d\phi. \tag{2.163}$$

By integrating Eq. (2.163) over all possible directions, the total energy emitted by dA can be found. Dividing this expression by dA gives

$$E(\mathbf{r}) = \int_0^{2\pi} \int_0^{\pi/2} I(\mathbf{r}, \theta, \phi) \cos\theta \sin\theta d\theta d\phi = \int_{2\pi} I(\mathbf{r}, \hat{\mathbf{s}}) \hat{\mathbf{n}} \cdot \hat{\mathbf{s}} d\Omega. \tag{2.164}$$

An identical expression would be obtained if the spectral emissive power, E_λ, and spectral intensity, I_λ, were used.

Using Kirchhoff's law it can be shown that the radiative intensity for a blackbody is independent of direction. By using this fact in combination with the spectral radiative intensity Eq. (2.164) reduces to

$$E_{b\lambda}(\mathbf{r}, \lambda_0) = \pi I_{b\lambda}(\mathbf{r}, \lambda_0). \tag{2.165}$$

The intensity is given per unit area normal to the rays, dA_p. If the intensity is to be compared to the emissive power per area it is important to remember that the emissive power is given per unit surface area dA. Due to the relation $dA = dA_p \cos\theta$ the directional emissive power is found as

$$\begin{aligned} & E'_{b\lambda}(\mathbf{r}, \lambda_0, \theta, \phi) dA = I_{b\lambda}(\mathbf{r}, \lambda_0) dA_p \\ \Rightarrow \quad & E'_{b\lambda}(\mathbf{r}, \lambda_0, \theta, \phi) = I_{b\lambda}(\mathbf{r}, \lambda_0) \cos\theta. \end{aligned} \tag{2.166}$$

This cosine dependence of the directional emissive power is often called Lambert's law. [34, pp. 13-15]

The treatment presented above is heavily based on idealized objects. No real object is a true blackbody, although many may be modelled as one to a reasonable approximation. Furthermore, a blackbody was introduced as an object with perfectly black surfaces, whereas in real objects the actual surface does not absorb or emit any radiation; both absorption and emission actually occur in a thin layer beneath the surface. In the description of real objects the following four radiative properties are used: reflectance, ρ, absorbtance, α, transmittance, τ, and emittance, ϵ. The first three of these are simply defined as the fraction of the total incoming radiation which is reflected, absorbed, or transmitted by the object, respectively. Thus $\rho + \alpha + \tau = 1$, and for a blackbody $\alpha = 1$ and $\rho = \tau = 0$. Since a blackbody is the perfect emitter, the emittance for a real object is defined as the ratio between the energy emitted by the object and the energy emitted by a blackbody at the same temperature. From Kirchhoff's law $\epsilon = \alpha$ for any object. Note, however, that all four properties may be dependent on temperature and wavelength. [34, pp. 20-22]

All of the radiative properties described above are also dependent on one or both of the incoming and outgoing directions. When describing these properties it is thus customary to distinguish between spectral and total properties as well as between directional and hemispherical properties. Further treatment of these concepts is beyond the scope of the present work, and the reader is instead referred to [34].

It should be noted that the radiative properties are also highly dependent on the material in question and the structure of the surface, the latter being the main focus of the

present work. The thermal radiation emitted by a given structure is easily found through the reflectance. From the definitions given above the emissivity of an opaque object can be found as $\epsilon = \alpha = 1 - \rho$. The energy emitted by the object in a given direction at a temperature T is then found as

$$E'_\lambda(\mathbf{r}, \lambda_0, \theta, \phi, T) = \epsilon E'_{b\lambda}(\mathbf{r}, \lambda_0, \theta, \phi, T), \tag{2.167}$$

where $E'_\lambda(\mathbf{r}, \lambda_0, \theta, \phi, T)$ is the directional emissive power of the object, and $E'_{b\lambda}(\mathbf{r}, \lambda_0, \theta, \phi, T)$ is the directional emissive power of a blackbody at the same temperature. The total energy emitted by the object is found by integrating Eq. (2.167) over all directions and all wavelengths at which thermal radiation occurs. It is important to remember that thermal radiation typically occurs at long infrared wavelengths, while the wavelengths of interest when considering absorption are often in the visible spectrum. Thus it is important to consider a wide range of wavelengths if a complete description of the radiative properties of a given surface is desired.

Program Code 3

In this chapter the code produced in relation to this thesis is presented. The first section contains an overview of all of the individual programs developed as well as the motivations behind each of them. An explanation of the different numerical techniques tested in the GFSIEM programs is also given. This is followed by a description of the stack matrix code used to model the structures under angles of incidence in both the xy plane and the yz plane. Finally an overview of the flow of the GFSIEM code is given for both directions of light incidence.

3.1 Overview of Programs

This section contains an overview of the program code produced in relation to the present work. Each of the individual MATLAB programs is introduced along with a brief explanation of the purpose of creating that particular program. The intention of this section is not to give a thorough description of all of the code, but rather to provide an overview of the thought process that led to the choices made.

The first code produced was a simple program to calculate the magnitude of the electric or magnetic field on the surface of a cylinder using the GFSIEM. This was done in order to become familiar with the GFSIEM through a simple geometry before moving on to more complex problems. A direct development to the first program was made by expanding it to calculate the scattering of light by the cylinder. This was done by using the calculated field on the surface of the cylinder to calculate the field in a grid of points around the cylinder. Aside from being a natural progression from the first program, this program served to further increase familiarity with the GFSIEM.

It was decided to calculate the reflectance of a sharp groove structure by using the stack matrix method. This was done because of the authors' prior knowledge of this method as well as a desire to compare this simplified model to the results obtained with the GFSIEM. The sharp grooves would be represented as a stack of thin layers with varying mode indices. In order to do this, however, two things were required. First, the appropriate mode indices for G-SPP's travelling through the grooves would have to be known. For this reason a program was developed to find the mode indices for G-SPP's in a large range of different wavelengths and gap widths. The program used the Newton-Raphson method to approach

the solution within a very small error margin as explained in Sec. 2.1.2. After calculating the mode indices, a set of coordinates representing the structure in question was needed. As such a program was developed to produce a sharp groove structure from a given requirement of angle of inclination and height of the structure. Using the obtained set of coordinates the structure could be converted into a stack of layers with mode indices corresponding to those for a G-SPP travelling in a gap of a certain width. A program using the stack matrix method was then used to calculate the reflectance of the multilayer system.

A basic program using the GFSIEM was then produced to calculate the reflectance of the same structures as those treated by the stack matrix method. The program used a rather crude approximation to the structure by simply representing the surface with a certain number of points, and for each point the Green's function was calculated anew. In order to verify the results produced by this program, they were compared to those presented in [9].

Since the obtained results were found to deviate from those of [9], various modifications of the program were tested. First it was attempted to reduce the running time of the program by simply tabulating the Green's function and interpolating in this table rather than calculating the Green's function for every single point on the surface. The same method of tabulating the Green's function was also attempted where the singularity was subtracted from the results before tabulation. This was done in order to make the interpolation more accurate, and the singularity was then simply added after performing the interpolation. Further attempts at increasing the accuracy of the method and reducing the required running time were made by using angle calculations (see Sec. 3.1.1) when the points in question were close to each other. Further calculations were made by including subdivisions of each line segment representing the surface. This was expected to improve the accuracy of the method as well as enabling the use of fewer points on the surface for the calculations, thus reducing the required running time. All of the programs used Johnson and Christy's model for the dielectric constant [35].

All of the programs described above were designed to allow for an angle of incidence only in the plane parallel to the direction of periodicity. It was desired to also perform calculations for angles of incidence in the plane perpendicular to the direction of periodicity, i.e. along the grooves. For this reason new versions of the stack matrix program and the GFSIEM program were produced to allow for an angle of incidence in this direction.

3.1.1 Numerical Techniques

Two main numerical techniques were tested in order to improve the convergence of the GFSIEM code. These techniques were the subdivision of surface elements and the inclusion of an angle calculation for elements close to each other. The concepts behind the two techniques are shown in Fig. 3.1.

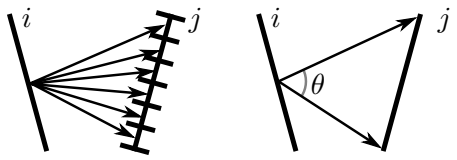

Figure 3.1. The principles of the numerical techniques used in the GFSIEM code. Left: Subdivision of surface elements. Right: Angle calculation for elements close to each other.

For the subdivision of surface elements each surface element was divided into a number of subelements, and in the calculation of the contribution from an element j to the field in an element i each subelement was considered separately. The total field contribution from element j would then be found as the sum of the contributions from each subelement. That is the Eqs. (2.107)-(2.110) or (2.149)-(2.150) are calculated as sums with a number of elements equal to the number of subelements. The angle calculation was introduced to provide a better approximation to the normal derivative of the Green's function for terms in Eqs. (2.106) or (2.140), where the elements i and j are close to each other. In these terms the normal derivative was approximated as the angle θ spanned by the vectors from the sampling point in element i to each end of the element j. The two numerical techniques presented here were both used on their own and in combination with each other.

3.2 Stack Matrix Code

As described in Sec. 2.2 the stack matrix method (SMM) is used for calculating the reflectance and transmittance of stacks of parallel layers. While the groove structures considered in the present work do not consist of stacks of parallel layers, they can in a simple model be represented as stacks of layers with refractive index corresponding to the mode index for a G-SPP propagating in a gap of the same width as the groove width in that layer. This principle is shown in Fig. 3.2. The mode indices used in the SMM are calculated by the process described in Sec. 2.1.2.

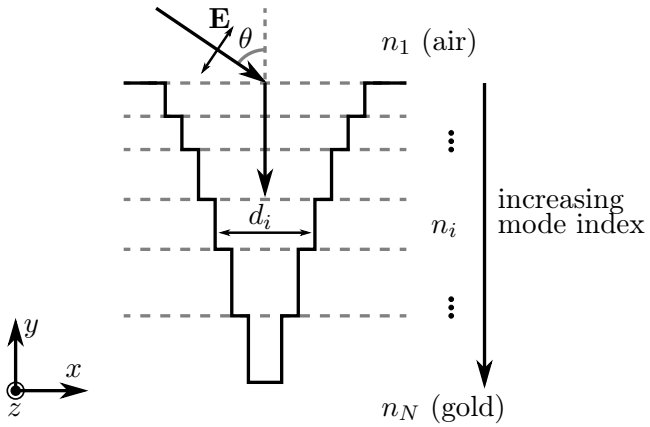

Figure 3.2. The principle used to convert one period of the groove structure into a multilayer structure to be used in the SMM. The figure also shows the physical interpretation of light incidence under an angle in the xy plane used in the SMM.

With the multilayer representation of the groove structure constructed by the principle shown in Fig. 3.2 the reflectance at normal incidence is simply calculated by applying the SMM to this multilayer structure. For incidence at an angle to the normal direction the problem must be treated differently depending on the direction of incidence. In the calculations for an angle of incidence in the xy plane the light is treated as p polarized light, but in all layers except the incident (air) layer the angle of incidence is set to 0 as illustrated in Fig. 3.2. In this case the in-plane wavenumber is not conserved across the first interface, which it would be for a stack of layers with parallel interfaces. This affects the reflection and transmission coefficients, which instead of the usual Fresnel coefficients described by Eqs. (2.39) and (2.40) become

$$\rho_{12} = \frac{(n_2/n_1)\cos(\theta) - 1}{(n_2/n_1)\cos(\theta) + 1}, \tag{3.1}$$

$$\tau_{12} = 1 + \rho_{12}. \tag{3.2}$$

In this representation the physical interpretation is that the incident light couples to a G-SPP, which propagates straight down into the groove.

In the calculations for an angle of incidence in the yz plane the in-plane wave number, $k_z = k_0 n_1 \sin(\theta)$, must be conserved through all layers, because the structure is invariant along the z axis. In this case, however, the light is treated as s polarized in the SMM. This situation is shown in Fig. 3.3. In this figure it is also seen that the choice of s polarization in the SMM is justified, since the main component of the electric field of the G-SPP is oriented as shown. The G-SPP also has a smaller electric field component in the direction of propagation. However, it is curious that the inherently p polarized G-SPP's must be modelled using s polarization. The ray path shown in Fig. 3.3 can be understood in a geometric optics picture and follows from Snell's law and the increasing mode index [36].

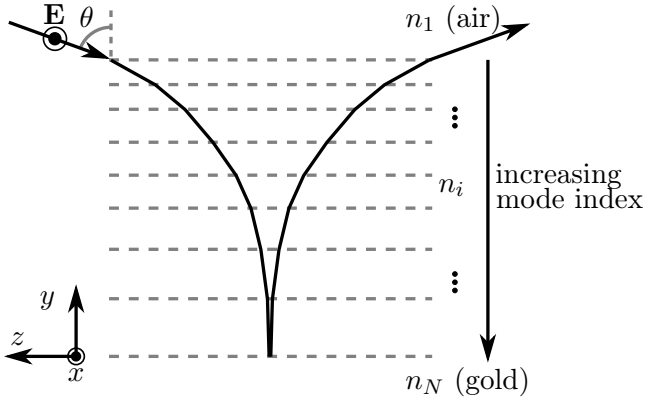

Figure 3.3. The physical interpretation of light incidence under an angle in the yz plane used in the SMM. For simplicity reflections at interfaces other than the last are omitted in the figure.

There is an important concern with regards to the usage of the SMM for the calculation of the reflectance of the sharp groove structures. This concern lies in the fact that the mode index for a G-SPP rapidly approaches very large values at small gap thicknesses and does

not approach the refractive index of gold in the limit of $d \to 0$. The final stack of layers will then contain layers with very large mode indices, which suddenly jump to the refractive index of gold at the bottom of the stack. In the model used here layers are only included for gap thicknesses down to 0.3 nm in order to avoid extremely large values of the mode index in the last layers.

A further modification to the standard SMM is made in the final layer of the structure by modifying the reflection phase in the reflection coefficient between the final layer and the gold substrate. The appropriate value of this reflection phase is assumed to be close to that for the reflection of a plane wave incident on an air-gold interface. As such the final reflection in the stack matrix, i.e. the reflection coefficient $\rho_{N-1,N}$ in $\mathbf{H}_{N-1,N}$, is instead treated as a reflection between air and gold. Calculations were performed in which this reflection occurred under normal incidence as well as under the angle that would be obtained in the final layer by applying Snell's law at each interface of the stack of layers. The results of these calculations deviated only slightly from each other, and as such the final model simply models this reflection as normal incidence.

3.3 GFSIEM Code

The GFSIEM code follows the theory presented in Secs. 2.6 and 2.7. In this section the flow of the code for the programs for each direction of light incidence is described. While the overall flow is very similar for the two directions of light incidence, both are given here to clarify the differences between the two programs.

3.3.1 Angle of Incidence in the xy Plane

When calculating the reflectance under an angle of incidence in the xy plane the GFSIEM code:

1. Loads the structure coordinates and refractive index data for gold and sets angle of incidence and wavelength interval.
2. Stores start and end points for each surface element and subelement and calculates the length and normal vectors of each element. Sampling points are set to the middle of each element.
3. Loops over wavelengths:
   a) Interpolates refractive index and dielectric constant of gold at the specific wavelength.
   b) Sets up the incident H field in each surface element
   c) Calculates the values of g_1 and g_2 as well as their normal derivatives with respect to x and y for a predefined grid of values of $(x - x')$ and $(y - y')$, then subtracts a Hankel function to remove the singularity, and finally stores these values in tables g_1, g_2, ndg_{1x}, ndg_{1y}, ndg_{2x}, and ndg_{2y}.
   d) Loops over surface elements r and r':

i. Extracts the appropriate coordinates and normal vectors for the current element and its subelements.

ii. Interpolates in the tables of g_1, g_2, ndg_{1x}, ndg_{1y}, ndg_{2x}, and ndg_{2y} at the appropriate values of $(x - x')$ and $(y - y')$, then adds a Hankel function to restore the previously removed singularity, and finds final values of g_1, g_2, ndg_1, and ndg_2.

iii. If $r = r'$ replaces the values of g_1, g_2, ndg_1, and ndg_2 at the middle subelement (sampling point) with appropriate approximations to avoid a singularity.

iv. Calculates the matrix elements of $\overline{\overline{A}}_1$, $\overline{\overline{A}}_2$, $\overline{\overline{B}}_1$, and $\overline{\overline{B}}_2$ at the specific set of (r, r').

e) Creates the final matrix using $\overline{\overline{A}}_1$, $\overline{\overline{A}}_2$, $\overline{\overline{B}}_1$, and $\overline{\overline{B}}_2$ and creates and solves the matrix equation to find the values of the H field and its normal derivative, ϕ, in each surface element.

f) Uses the H and ϕ values to calculate the field in a specific point far away from the surface and compares this to the value of the incident field to obtain the reflectance at the given wavelength.

3.3.2 Angle of Incidence in the yz Plane

When calculating the reflectance under an angle of incidence in the yz plane the GFSIEM code:

1. Loads the structure coordinates and refractive index data for gold and sets angle of incidence and wavelength interval.

2. Stores start and end points for each surface element and subelement and calculates the length and normal vectors of each element. Sampling points for large elements are set to the starting point of the element, and sampling points for subelements are set to the middle points of the subelements.

3. Loops over wavelengths:

   a) Interpolates refractive index and dielectric constant of gold at the specific wavelength.

   b) Sets up the incident H and E fields in each surface element.

   c) Calculates the values of g_1 and g_2 as well as their normal derivatives with respect to x and y for a predefined grid of values of $(x - x')$ and $(y - y')$, then subtracts a Hankel function to remove the singularity, and finally stores these values in tables g_1, g_2, ndg_{1x}, ndg_{1y}, ndg_{2x}, and ndg_{2y}.

   d) Loops over surface elements r and r':

      i. Extracts the appropriate coordinates and normal vectors for the current element and its subelements.

      ii. Interpolates in the tables of g_1, g_2, ndg_{1x}, ndg_{1y}, ndg_{2x}, and ndg_{2y} at the appropriate values of $(x - x')$ and $(y - y')$, then adds a Hankel function to

restore the previously removed singularity, and finds final values of g_1, g_2, ndg_1, and ndg_2.

iii. If $r = r'$ or $r = r' + 1$ or $r = 1 \wedge r' = N$ replaces the values of g_1, g_2, ndg_1, and ndg_2 at the first subelement (sampling point) with appropriate approximations to avoid a singularity.

iv. Weights each element of g_1, g_2, ndg_1, and ndg_2 by the weight functions N_1 and N_2 and calculates the matrix elements $\overline{\overline{A}}^{(1,1)}$, $\overline{\overline{A}}^{(1,2)}$, $\overline{\overline{A}}^{(2,1)}$, $\overline{\overline{A}}^{(2,2)}$, $\overline{\overline{B}}^{(1,1)}$, $\overline{\overline{B}}^{(1,2)}$, $\overline{\overline{B}}^{(2,1)}$, and $\overline{\overline{B}}^{(2,2)}$ at the specific set of (r, r').

e) Constructs the matrices $\overline{\overline{A}}_1$, $\overline{\overline{A}}_2$, $\overline{\overline{B}}_1$, and $\overline{\overline{B}}_2$ and creates and solves the matrix equation to find the E and H fields and their normal derivatives, ϕ_E and ϕ_H, in each surface element.

f) Uses the E, H, ϕ_E, and ϕ_H values to calculate the field in a specific point far away from the surface and compares this to the value of the incident field to obtain the reflectance at the given wavelength.

Numerical Results 4

This chapter contains a presentation of the results produced with the different programs for calculating the reflectance of periodic groove arrays. The calculations were performed for groove arrays constructed in the same way as those presented in [9]. Reflectances were calculated using both the GFSIEM and the SMM. The reflectance calculations with the GFSIEM include all reflected waves, and not only specular reflection.

The first GFSIEM programs were developed to test the different numerical techniques described in Sec. 3.1.1 in order to optimize the convergence of the calculations. The goal of the tests of the numerical techniques was to reproduce the results of Figs. 7a and 9a of [9] in the simplest and fastest way possible. The results of the different combinations of numerical techniques are presented in Sec. 4.1. It was found that the best results were obtained when using subdivision of the surface elements without an angle calculation for elements close to each other. For this reason all of the results presented in subsequent sections use this numerical technique. The calculations were tested for convergence by running calculations with significantly increased numbers of points. The results of these tests are presented in Sec. 4.2.

In Secs. 4.3-4.6 the results of the reflectance calculations using the GFSIEM and the SMM are presented for angles of incidence in both the xy plane and the yz plane. All of the groove arrays used in these calculations are made in a gold surface and have periods of $\Lambda = 250$ nm, groove depths of $h = 500$ nm, and 10 nm plateaus between neighbouring grooves. Seven different groove bottom widths are used, namely 0.3, 1, 2, 5, 10, 20, and 50 nm. The groove arrays are represented in the code as coordinate sets describing the surface of a single period of the structure. The structure with a bottom width of 0.3 nm is represented by 700 surface elements, while the structures with bottom widths of 1 and 2 nm are represented by 716 surface elements, and the structures with bottom widths of 5, 10, 20, and 50 nm are represented by 340 surface elements. Each surface element is further divided into 21 subelements. The number of surface elements for a given structure is chosen such that the field along the surface can be described properly. At smaller gap widths the field varies more rapidly with distance along the surface, and as such more points are required to accurately describe the field as the groove becomes narrower. For this reason the density of points is larger near the bottom of the structures with smaller bottom widths.

For ease of reading Secs. 4.3-4.6 only contain reflectance graphs for the structures with

bottom widths of 0.3 and 10 nm. A collection of reflectance graphs for all of the considered structures and angles of incidence is included in Appendix B.

4.1 Test of Different Numerical Techniques

In this section the results of the different numerical techniques presented in Sec. 3.1.1 are summarized. Here the numerical techniques will be referred to as angle calculation and subdivision. In order to evaluate the numerical techniques in relation to each other, two sets of reflectance spectra were produced with each combination of the numerical techniques, i.e. with and without angle calculation and subdivision as well as without any of them. The purpose of testing the different combinations of numerical techniques was to determine the most efficient way to obtain accurate results. Figs. 7a and 9a of [9] were used as guidelines when determining the quality of the results produced by each of the methods presented here. In the first set of reflectance spectra the reflectance was calculated at normal incidence for each of the different structures with bottom widths of 0.3, 1, 2, 5, 10, 20, and 50 nm. These results are shown in Fig. 4.1. In the second set of spectra, which is shown in Fig. 4.2, the reflectance was calculated at the angles of incidence of 0, 20, 40, 50, 60, 70, and 80° for the structure with a bottom width of 0.3 nm.

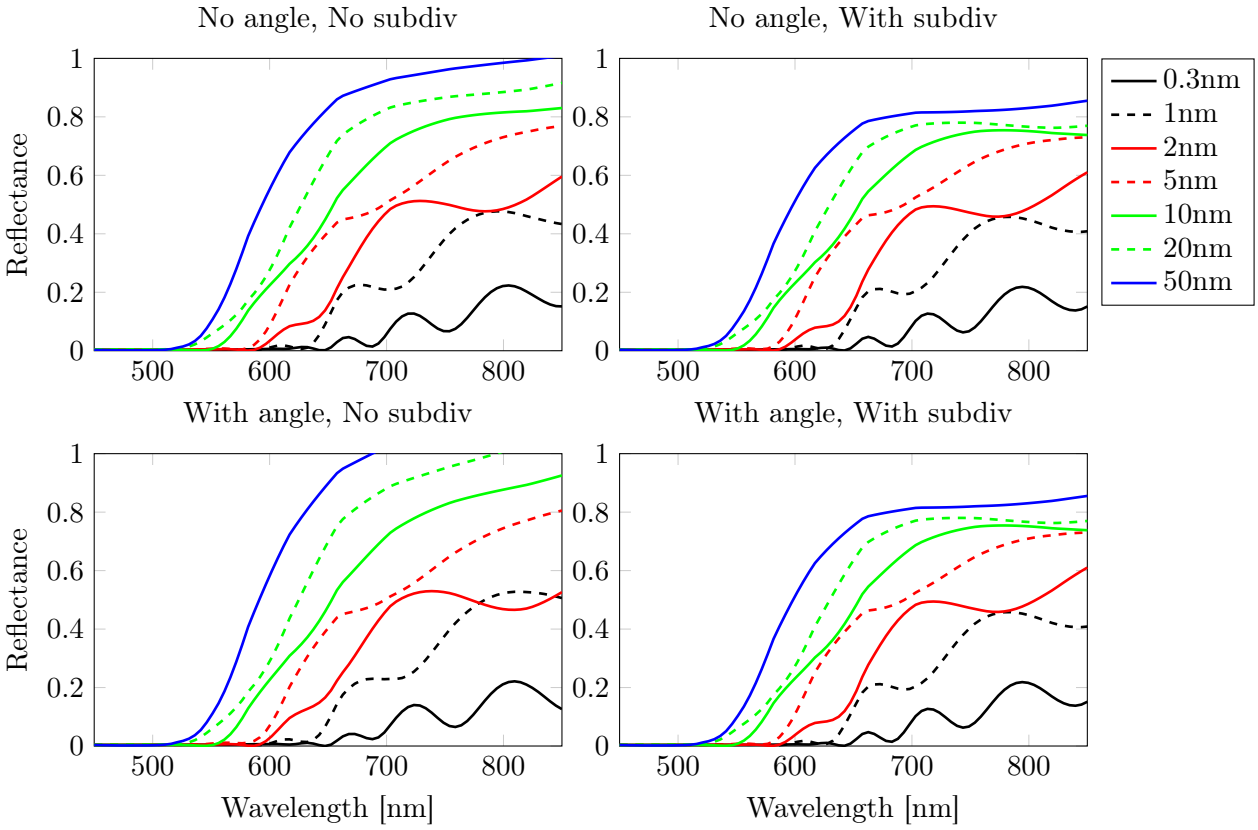

Figure 4.1. Reflectance of the different structures at normal incidence as calculated by the GFSIEM with different numerical techniques.

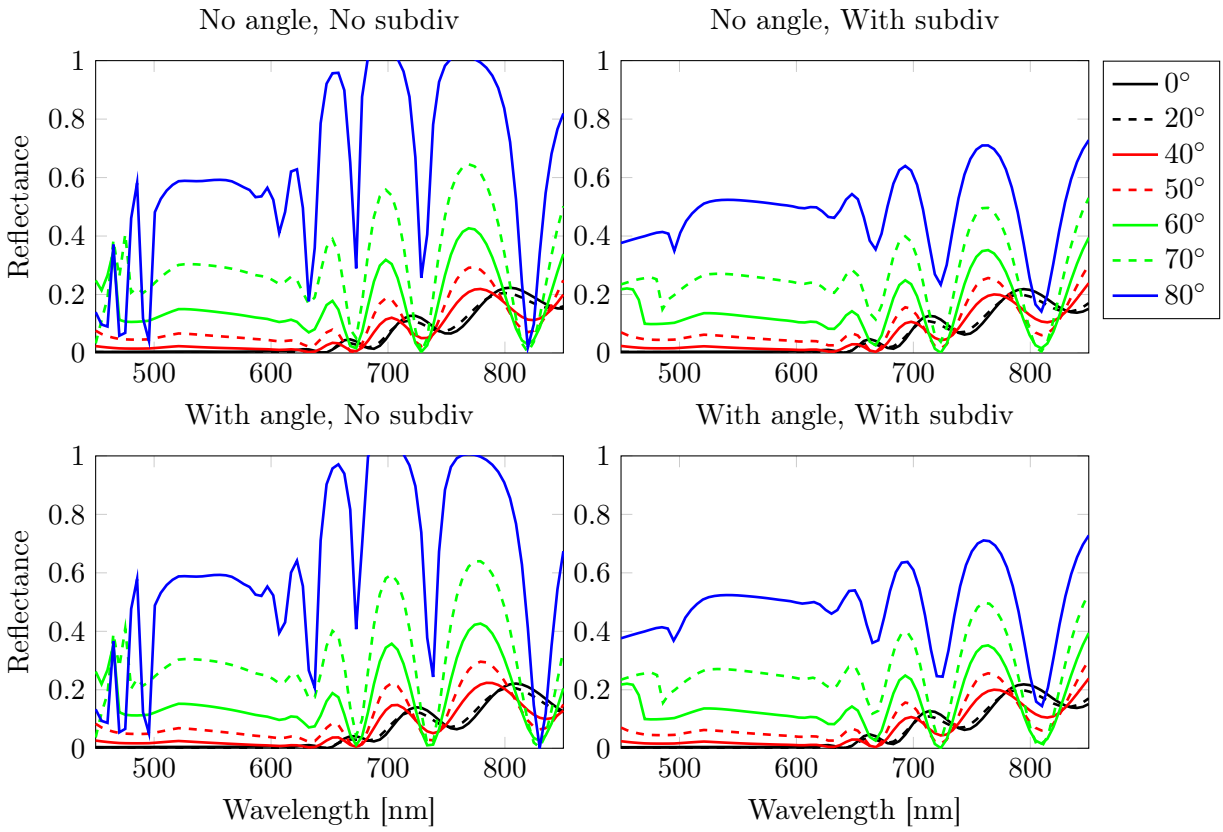

Figure 4.2. Reflectance of the structure with a bottom width of 0.3 nm under different angles of incidence as calculated by the GFSIEM with different numerical techniques.

It is evident from Figs. 4.1 and 4.2 that the GFSIEM calculations do not converge properly without subdivision of the surface elements with the chosen amount of surface elements for these structures. Regardless of whether or not the angle calculation is used, reflectance values above 1 are seen for the calculations without subdivision. Since this does not make sense physically, all of these results are considered inaccurate. The inaccuracy of these calculations is seen to increase with increasing bottom width and increasing angle. However, as mentioned previously the structures with larger bottom widths were represented by fewer surface elements, and as such the error is more likely an indication that this lower amount of surface elements is inadequate for properly describing the surface. In the calculations with subdivision it is immediately evident that the calculations have produced better results, since no reflectance values above 1 are seen. Furthermore, by comparison with the reference graphs of [9] these results appear identical.

It was found that the quality of the results without subdivision could be improved by increasing the amount of surface elements. However, even with twice the amount of surface elements they still deviated significantly from those with subdivision. Since part of the criteria used in determining the best numerical technique was the running time of the code, and the running time scales as the square of the number of surface elements, it was concluded that subdivision of the surface elements was required. The addition of the angle calculation

was not sufficient to make up for the difference between subdivision and no subdivision, and for most of the structures it actually made the calculations converge even more poorly.

As for the calculations with subdivision it is seen that the inclusion of the angle calculation makes very little, if any, difference. Both the results with and without angle calculation and with subdivision are practically identical to the reference graphs of [9]. While the running time of the code with angle calculation is not noticeably longer than that of the code without angle calculation, the code is more complex, where the ideal code would be as simple and as accurate as possible. For these reasons it was decided not to use the angle calculation in subsequent calculations, and as such all GFSIEM results presented in the next sections were made with subdivision and without angle calculation.

4.2 Test of Convergence

In order to test the convergence of the GFSIEM calculations a set of calculations was made in which the number of surface elements used to represent each structure was greatly increased. If the GFSIEM calculations have converged, no change in the results should occur by increasing the amount of points used in the calculations. As an example of the convergence tests Fig. 4.3 shows the reflectance spectra of the structures with bottom widths of 0.3, 2, and 10 nm as calculated by the GFSIEM with the structures represented by 700, 716, and 340 points, respectively, compared to the reflectance spectra with the structures represented by 1272, 1272, and 632 points, respectively. It is seen that the two sets of calculations are nearly identical, and as such it is concluded that the GFSIEM calculations have converged with the lower amount of points.

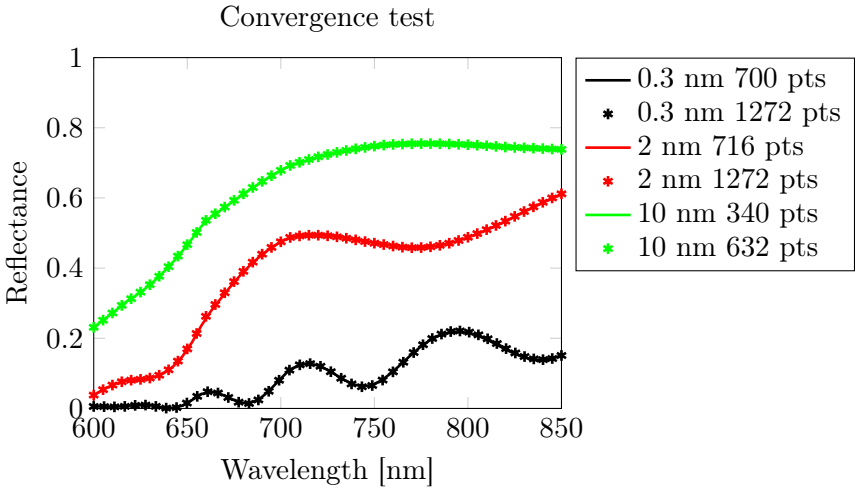

Figure 4.3. The reflectance of the structures with bottom widths of 0.3, 2, and 10 nm as calculated by the GFSIEM with different numbers of surface elements.

4.3 GFSIEM, xy Incidence

In this section the results of the reflectance calculations performed with the GFSIEM for an angle of incidence in the xy plane are presented. The results were produced with the code described in Sec. 3.3.1. Reflectance spectra were calculated for the different groove bottom widths of 0.3, 1, 2, 5, 10, 20, and 50 nm in the wavelength range of 450-850 nm at angles of incidence of 0, 20, 40, 50, 60, 70, and 80°. Fig. 4.4 shows the reflectance spectra of the structures with bottom widths of 0.3 and 10 nm. The reflectance spectra for the other structures are shown in Appendix B.1.

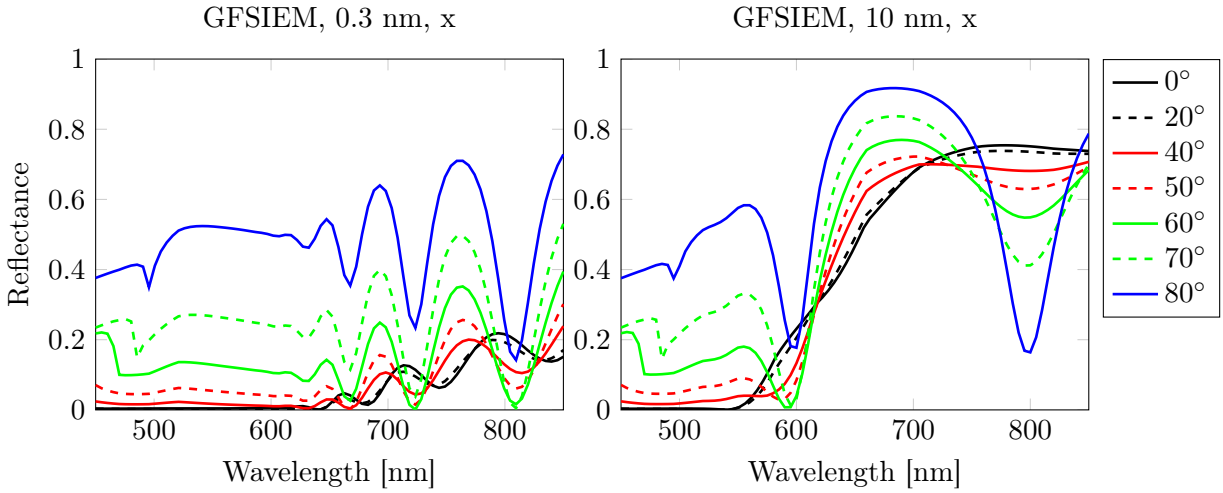

Figure 4.4. Reflectances of the structures with bottom widths of 0.3 and 10 nm under angles of incidence in the xy plane as calculated by the GFSIEM.

It is seen that the overall reflectance is smaller for smaller bottom groove widths. For all of the structures it is seen that an increasing angle of incidence increases the overall reflectance. However, the angle of incidence also results in oscillations in the reflectance spectra, even for structures where the reflectance at normal incidence does not exhibit oscillations. The oscillations start at wavelengths near 600 nm, with the onset shifting slightly towards shorter wavelengths with an increasing bottom width. An increasing bottom width also leads to a reduction in the frequency of the oscillations. This is clearly seen from the fact that the reflectance spectra for the structure with a bottom width of 0.3 nm show four periods of oscillations, whereas only two periods are seen in the spectra for the structure with a bottom width of 10 nm. The positions of the maxima and minima of the oscillations are constant across all of the tested angles of incidence for each structure. It is observed that the magnitudes of the maxima in the oscillations increase with an increasing angle of incidence, and for all structures except the one with a bottom width of 0.3 nm the magnitudes of the minima decrease with an increasing angle of incidence.

The structures with bottom widths of 1, 2, and 5 nm are particularly interesting in this respect. All of these structures exhibit reflectance minima with magnitudes very close to 0 at wavelengths where the structures display high reflectance at normal incidence. A very strong dependence on the bottom groove width is seen for these minima, which are located

at wavelengths of roughly 795, 720, and 650 nm for the bottom widths of 1, 2, and 5 nm, respectively. The reflectance minima correspond to maxima of both absorption and emission, indicating that the structures can be tailored to a specific requirement for absorption or emission.

While all of the structures exhibit reflectances very close to 0 at normal incidence and short wavelengths (below 500-600 nm depending on the structure) it is seen that the reflectance in this wavelength range increases significantly at larger angles of incidence. Especially notable is the difference between the angles of 70 and 80°, where an almost two-fold increase in reflectance is seen for most of the structures. Another effect of the increasing angle of incidence, which is seen in this wavelength range, is the presence of sharp changes in the reflectances at wavelengths just below 500 nm. These features arise from diffraction effects, which become prevalent at larger angles of incidence. This can be seen from the grating equation,

$$\Lambda \left(\sin \theta_i + \sin \theta_m\right) = m\lambda, \tag{4.1}$$

which describes the condition for diffraction maxima. Here Λ is the period of the grating, θ_i is the incident angle, θ_m is the angle at which the diffracted light exhibits maximum intensity, λ is the wavelength of the incident light, and m is an integer. From Eq. (4.1) it is seen that diffraction at normal incidence only occurs for periods $\Lambda \geq \lambda$, whereas an increasing angle of incidence leads to diffraction effects at wavelengths longer than the period.

4.4 SMM, xy Incidence

In this section the results of the reflectance calculations performed with the SMM for an angle of incidence in the xy plane are presented. These results were produced with the code described in Sec. 3.2. Reflectance spectra were calculated for the different groove bottom widths of 0.3, 1, 2, 5, 10, 20, and 50 nm in the wavelength range of 600-850 nm at angles of incidence of 0, 20, 40, 50, 60, 70, and 80°. Fig. 4.5 shows the reflectance spectra of the structures with bottom widths of 0.3 and 10 nm. The reflectance spectra for the other structures are shown in Appendix B.2. The reflectance calculations using the SMM have only been performed for wavelengths in the range of 600-850 due to the fact that gold behaves as a dielectric material at short wavelengths. Since a dielectric material cannot support G-SPP's, the physical interpretation used in the SMM does not hold at short wavelengths. Nevertheless, the reflectance graphs calculated with the SMM are plotted with wavelength axes ranging from 450 to 850 nm to facilitate comparison with the GFSIEM results.

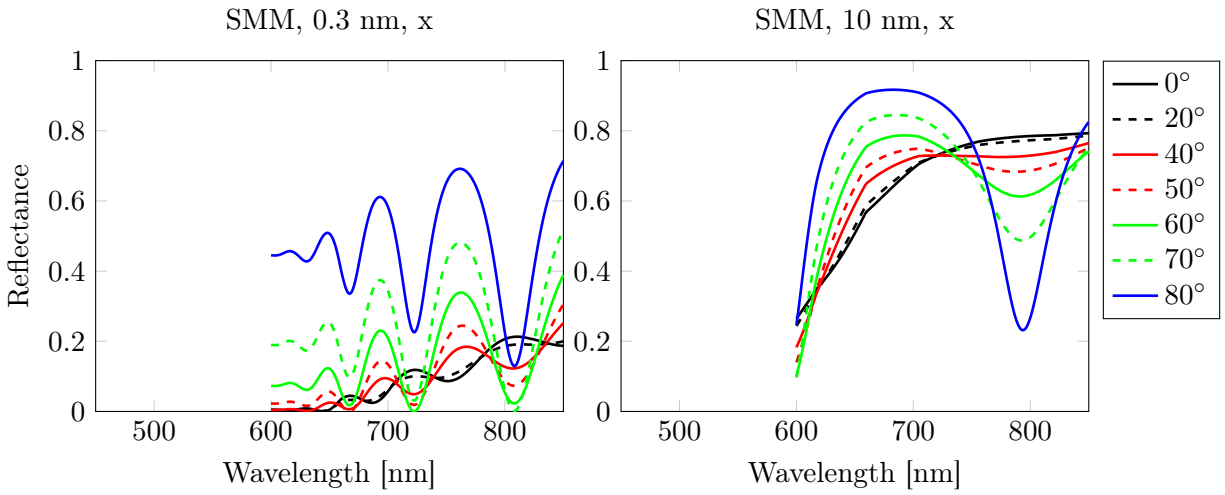

Figure 4.5. Reflectances of the structures with bottom widths of 0.3 and 10 nm under angles of incidence in the xy plane as calculated by the SMM.

It is immediately evident that the results of the SMM are remarkably similar to those of the GFSIEM. For this reason the features seen in the reflectance spectra will not be discussed here, since everything that was mentioned in Sec. 4.3 still applies.

Perhaps the most apparent similarity between the results of the two methods is found in the positions of the minima and maxima in the reflectance spectra. In the case of the larger bottom widths it is seen that the degree of similarity between the GFSIEM and the SMM decreases, as the magnitudes of the reflectance spectra differ slightly, and in some cases the positions of the minima or maxima are slightly shifted. However, the same features are clearly reproduced in the spectra produced with the SMM. It is remarkable that such a large degree of similarity is obtained with the two very different methods employed here, especially since the SMM is a highly simplified model. The fact that the SMM produces very similar results to the exact GFSIEM supports the physical interpretation that the low reflectance is caused by the coupling of light into G-SPP's, and it further indicates that the interaction between the light and the structures is dominated by this coupling effect. It should be noted that in the SMM used here, it is assumed that all of the incident light couples to G-SPP's. A contributing factor to the similarity between the SMM results and the GFSIEM results is thus the fact that the investigated structures have very small plateaus between neighbouring grooves, such that nearly 100% of the light couples to G-SPP's. If the plateaus were larger it would be necessary to incorporate some coupling factor into the first layer of the structure in the SMM in order to accommodate for the lower amount of light coupling into the structure.

4.5 GFSIEM, yz Incidence

In this section the reflectance spectra for the angles of incidence of 0, 20, 40, 50, 60, and 70° in the yz plane as calculated with the GFSIEM are presented. The spectra were produced with the code described in Sec. 3.3.2. The results for the structures with bottom widths of 0.3 and 10 nm are shown in Fig. 4.6, while the results for all of the structures are shown in Appendix

B.3. Results have not been included for angles larger than 70°, since the z components of the fields become small compared to the total fields at large angles of incidence in the yz plane. This, in turn, results in poor convergence of the GFSIEM calculations as the implementation used here is based on the z components of the fields.

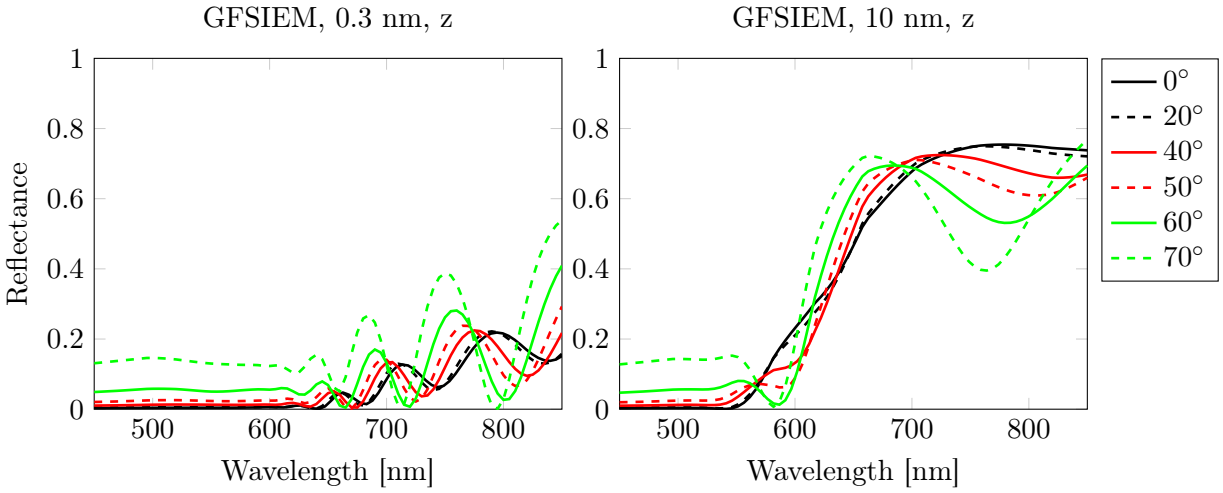

Figure 4.6. Reflectances of the structures with bottom widths of 0.3 and 10 nm under angles of incidence in the yz plane as calculated by the GFSIEM.

As with the results for an angle of incidence in the xy plane these results show a tendency for lower overall reflectances for smaller bottom widths, as well as an oscillatory behaviour in the spectra. The frequency of the oscillatory behaviour is larger for smaller bottom widths. Unlike the results for angles of incidence in the xy plane it is seen that the positions of the reflectance maxima and minima shift towards shorter wavelengths at larger angles of incidence. From the relation $k_s^2 = k_0^2\varepsilon - k_z^2$ it is seen that the behaviour may be attributed to the fact that an increasing angle of incidence in the yz plane increases the magnitude of k_z, which in turn reduces k_s. The reduction of k_s naturally leads to a shift in resonances towards shorter wavelengths. It is worth noting that for small bottom widths the reflectance spectra have several minima where the reflectance is close to zero. For larger bottom widths minima in the spectra are still observed, although with larger reflectance values. Furthermore, an increasing angle of incidence is observed to increase the overall reflectance as was the case for an angle of incidence in the xy plane. Here, however, the increase is smaller than for an angle of incidence in the xy plane.

4.6 SMM, yz Incidence

In this section the reflectance spectra for the angles of incidence of 0, 20, 40, 50, 60, and 70° in the yz plane as calculated by the SMM are presented. The spectra were produced with the code described in Sec. 3.2. The results for the structures with bottom widths of 0.3 and 10 nm are shown in Fig. 4.7, while the results for all of the structures are shown in Appendix B.4.

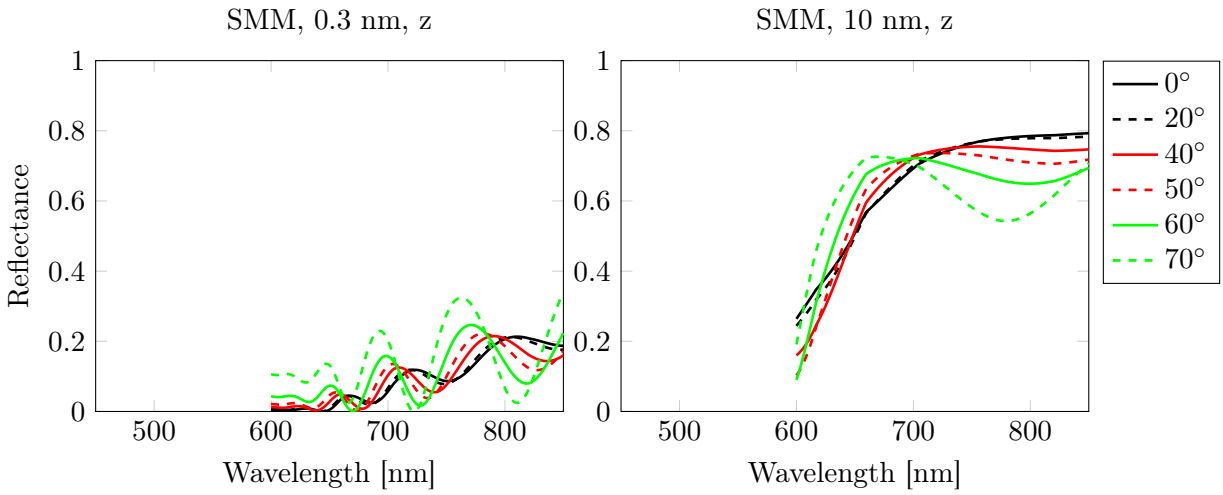

Figure 4.7. Reflectances of the structures with bottom widths of 0.3 and 10 nm under angles of incidence in the xy plane as calculated by the SMM.

Comparing the stack matrix results to those of the GFSIEM reveals a high degree of similarity. The results for the structures with smaller bottom widths exhibit notably high degrees of similarity. A few smaller discrepancies are seen, however. Some of the positions of the maxima and minima are shifted slightly, and the magnitude of the reflectance is also slightly off in some cases. The latter is clearly seen for the structure with a bottom width of 0.3 nm at an angle of incidence of 70°, where the magnitude of the reflectance peak between 700 and 800 nm is roughly 15% smaller than that seen with the GFSIEM. In general the discrepancies between the GFSIEM and SMM are more noticeable at larger angles of incidence. The larger discrepancies between the SMM and the GFSIEM seen for this direction of light incidence compared to the case of light incidence in the xy plane could be caused by the approximations used in describing the situation. For the case of light incidence in the yz plane, the ray path is calculated purely from a geometric optics perspective and follows from Snellâ€™s law and the increasing mode index. In reality the situation might be more complex, leading to the minor inaccuracies seen here. The overall tendencies seen in the reflectance spectra calculated with the GFSIEM are still clearly reproduced with the SMM, however.

It is important to note that the use of s polarization in the SMM for an angle of incidence in the yz plane is essential for obtaining results with as high a degree of similarity to the GFSIEM results as seen here. If p polarization is used the reflectance spectra deviate significantly from those of the GFSIEM. This can be understood by considering the direction of the field compared to the structure as shown in Fig. 3.3.

Discussion and Conclusion 5

In the previous chapters a theoretical foundation of the physics of ultra-sharp plasmonic grooves was given. The absorption processes in such structures are dominated by the coupling of light into G-SPP's. The physics and the conditions for the existence of G-SPP's were presented in Sec. 2.1. Following this two approaches for modelling the absorption of light in two-dimensional structures were described, namely the SMM presented in Sec. 2.2 and the GFSIEM presented in Secs. 2.3 through 2.7. In Sec. 2.8 it was described how the absorption of light is related to thermal emission, as this is a highly relevant consideration in applications such as TPV and CSP. The reflectance spectra of ultra-sharp plasmonic grooves were then calculated numerically using the GFSIEM and the SMM. In this chapter we summarize and discuss our theoretical work and the obtained numerical results.

Initially a program using the GFSIEM was constructed to calculate the scattering of light by a cylinder, when the light is incident in a plane perpendicular to the longitudinal direction. The program was then expanded such that the reflectance spectra of periodic structures could be calculated. However, the computation time for a reflectance spectrum was so long that it would become impractical for larger problems. As such the program underwent an optimization process, which led to several modifications, the most important of which was to tabulate the Green's function in a large grid. In this manner the Green's function could be found through interpolation in the grid, rather than having to calculate it separately for each surface point. Before tabulating the Green's function the singularity was subtracted in order to obtain smoothly varying values, and after interpolation it was added again. The tabulation reduced the computation time significantly, although the structures still had to be represented by large amounts of points in order for the results to converge. In order to improve the convergence and reduce the required computation time two different numerical techniques were tested, namely subdivision of surface elements and an angle calculation for elements close to each other. It was found that the convergence of the calculations improved significantly by using subdivision, such that the number of surface elements required to represent a given structure was reduced. This, in turn, greatly reduced the computation time. The inclusion of the angle calculation did not reduce the required amount of surface elements, and as such this numerical technique was not used in the final program.

After introducing the optimizations mentioned above, the program was used to calculate the reflectance spectra of periodic arrays of ultra-sharp grooves in a gold surface. The groove

arrays used in the calculations had periods of $\Lambda = 250$ nm, groove depths of $h = 500$ nm, and 10 nm plateaus between neighbouring grooves. Reflectance spectra were calculated for grooves with bottom widths of 0.3, 1, 2, 5, 10, 20, and 50 nm in the wavelength range of 450-850 nm at angles of incidence of 0, 20, 40, 50, 60, 70, and 80° in the xy plane. The purpose of this was to examine the changes in the absorption properties of a gold surface caused by the introduction of these structures. Several interesting features were seen from the reflectance spectra. The most immediately apparent feature is a significant reduction in the overall reflectance, with smaller groove bottom widths exhibiting lower reflectances. At increasing angles of incidence the overall reflectance increases, although the effect is very small for small angles of incidence ($\sim 20°$). At larger angles of incidence oscillations appear in the reflectance spectra. The magnitude of the oscillations increases with increasing angle of incidence, although the positions of the maxima and minima of the oscillations remain the same. These features could be utilized in devices, where the absorption can be controlled by simply changing the angle of the device relative to the incident light. In order to get a complete picture of the radiative properties of the structures reflectances should also be calculated for infrared wavelengths as well as for a continuum of incidence angles. This is essential for the calculation of the thermal emission of a structure, since integration over all wavelengths and angles of incidence is required as described in Sec. 2.8. Due to the required computation time this becomes a daunting task, however. As such a significant amount of time can be saved by investigating one part of the spectrum, e.g. the visible wavelength range, and then using these results to determine which structures warrant further investigations in other wavelength ranges.

As an alternative to the time consuming GFSIEM, a program using the SMM was constructed. This program was based on the approximation that the light incident on the structure is coupled directly into a G-SPP propagating downward into the structure as explained in Sec. 3.2. This approximation is based on an effective medium approach, where the structure is represented as layers with mode indices corresponding to the mode indices of a G-SPP. The SMM program was used to calculate the reflectance spectra of the same structures at the same angles of incidence as was done with the GFSIEM. Comparing the results of the GFSIEM and the SMM shows remarkable similarities for small bottom widths. This neatly demonstrates that the absorption processes in the structures are dominated by light coupling into G-SPP's. The strength of the SMM lies in its speed, as it is several thousand times faster than the GFSIEM. However, the price to be paid in using the SMM lies in the fact that it is based on approximations, and as such it does not produce exact results. Furthermore the model only works when the incident light couples to G-SPP's, which only occurs for p polarized light, and only at certain wavelengths due to the real part of the dielectric function of gold becoming non-negative at some wavelengths. Despite these shortcomings, the method quickly provides an overview of the reflection properties of a given structure for a large range of visible wavelengths.

After producing reflectance spectra for light incidence in the xy plane, the next step was to construct a program capable of calculating reflectance spectra for light incidence in the yz plane. Since little attention had been given to this problem previously, new theory had to be developed to expand the GFSIEM such that it could be used for a general direction of

light incidence. One of the challenges in this regard lies in the fact that, depending on the direction of light incidence, the electric and magnetic fields may be coupled, and as such the complexity of the problem increases significantly. However, since the computation time primarily scales with the square of the number of surface elements, the inclusion of the coupling between the fields does not noticeably affect the computation time.

This program was used to calculate the reflectance spectra for the same groove structures with bottom widths of 0.3, 1, 2, 5, 10, 20, and 50 nm in the wavelength range of 450-850 nm at angles of incidence of 0, 20, 40, 50, 60, and 70° in the yz plane. It was observed that the overall reflectance was generally lower than for the case of light incidence in the xy plane. Furthermore, the reflectance minima shift towards shorter wavelengths as the angle increases. As the angle increases, so does the magnitude of the wavevector k_z, which in turn reduces the in-plane wavevector, k_s. The reduction in k_s leads to resonances at shorter wavelengths. For smaller bottom widths several minima in the reflectance spectra with magnitudes close to zero are seen. This, combined with the angular dependence of the resonances, may be used in the design of a device to sort out desired visible light. The wavelength that is sorted out could then be mechanically controlled by changing the angle of the device in relation to the incident light. As before reflectance spectra were calculated with an SMM program, and these results were then compared to the results produced by the GFSIEM. The comparison shows that both methods produce similar results with slight variations in peak positions and magnitudes of the reflectances, but overall the results show the same tendencies. The similarity is most notable for smaller bottom widths.

Several topics are interesting for further work. Having examined several groove structures, it is clear that the bottom widths have to be small in order to get significant absorption of visible light, but it remains to be examined whether these structures are suitable for use in applications such as TPV and CSP. It is therefore of interest to examine the reflectance properties of these structures in the infrared spectrum. Furthermore, the primary method for obtaining very small bottom widths is focused ion beam milling [8], which is a time consuming and expensive process. As such it would be interesting to investigate the use of other materials, which can also support G-SPP's in similar structures, such as chromium, nickel, platinum, and palladium. These materials are more lossy than gold, and as such the requirement to the bottom groove width can be relaxed [9]. Other plasmonic materials such as TiN [37] could also be of interest. Another relevant aspect to investigate further is the incorporation of non-local effects in the GFSIEM calculations. Non-local effects are likely to influence the properties of the structures with small bottom widths, and it is possible that the model might more accurately predict the properties of a given structure by taking these into account.

Derivations A

A.1 Determinant for the G-SPP Mode Index

This section shows the process of reducing Eqs. (2.20), (2.21), (2.23), and (2.24) to a set of two equations with two unknowns and finding the determinant of this set of equations. The starting point is the equations

$$0 = -A + Be^{-i\kappa_{yI}d} + Ce^{i\kappa_{yI}d}, \tag{A.1}$$

$$0 = B + C - D, \tag{A.2}$$

$$0 = \frac{1}{\varepsilon_M} i\kappa_{yM} A - \frac{1}{\varepsilon_I} i\kappa_{yI} Be^{-i\kappa_{yI}d} + \frac{1}{\varepsilon_I} i\kappa_{yI} Ce^{i\kappa_{yI}d}, \tag{A.3}$$

$$0 = -\frac{1}{\varepsilon_M} i\kappa_{yM} D - \frac{1}{\varepsilon_I} i\kappa_{yI} B + \frac{1}{\varepsilon_I} i\kappa_{yI} C, \tag{A.4}$$

$$\kappa_{yI} = \sqrt{k_0^2 \varepsilon_I - \beta^2}, \tag{A.5}$$

$$\kappa_{yM} = \sqrt{k_0^2 \varepsilon_M - \beta^2}. \tag{A.6}$$

A and D are found from Eqs. (A.1) and (A.2) as

$$A = Be^{-i\kappa_{yI}d} + Ce^{i\kappa_{yI}d}, \tag{A.7}$$

$$D = B + C. \tag{A.8}$$

Eq. (A.7) is inserted into Eq. (A.3) to give

$$\frac{1}{\varepsilon_M} i\kappa_{yM} \left(Be^{-i\kappa_{yI}d} + Ce^{i\kappa_{yI}d} \right) - \frac{1}{\varepsilon_I} i\kappa_{yI} Be^{-i\kappa_{yI}d} + \frac{1}{\varepsilon_I} i\kappa_{yI} Ce^{i\kappa_{yI}d} = 0 \tag{A.9}$$

$$\Updownarrow$$

$$B \left(\frac{1}{\varepsilon_M} i\kappa_{yM} e^{-i\kappa_{yI}d} - \frac{1}{\varepsilon_I} i\kappa_{yI} e^{-i\kappa_{yI}d} \right) + C \left(\frac{1}{\varepsilon_M} i\kappa_{yM} e^{i\kappa_{yI}d} + \frac{1}{\varepsilon_I} i\kappa_{yI} e^{i\kappa_{yI}d} \right) = 0 \tag{A.10}$$

$$\Updownarrow$$

$$B \left(\frac{1}{\varepsilon_M} i\kappa_{yM} - \frac{1}{\varepsilon_I} i\kappa_{yI} \right) + C \left(\frac{1}{\varepsilon_M} i\kappa_{yM} e^{2i\kappa_{yI}d} + \frac{1}{\varepsilon_I} i\kappa_{yI} e^{2i\kappa_{yI}d} \right) = 0. \tag{A.11}$$

Eq. (A.8) is inserted into Eq. (A.4) to give

$$-\frac{1}{\varepsilon_M}i\kappa_{yM}\left(B+C\right)-\frac{1}{\varepsilon_I}i\kappa_{yI}B+\frac{1}{\varepsilon_I}i\kappa_{yI}C=0 \tag{A.12}$$

$$\Updownarrow$$

$$B\left(-\frac{1}{\varepsilon_M}i\kappa_{yM}-\frac{1}{\varepsilon_I}i\kappa_{yI}\right)+C\left(-\frac{1}{\varepsilon_M}i\kappa_{yM}+\frac{1}{\varepsilon_I}i\kappa_{yI}\right)=0. \tag{A.13}$$

The Eqs. (A.11) and (A.13) then constitute the desired set of two equations with two unknowns. The determinant of this set of equations is then

$$\begin{aligned}&\left(\frac{1}{\varepsilon_M}i\kappa_{yM}-\frac{1}{\varepsilon_I}i\kappa_{yI}\right)\left(-\frac{1}{\varepsilon_M}i\kappa_{yM}+\frac{1}{\varepsilon_I}i\kappa_{yI}\right)\\&-\left(-\frac{1}{\varepsilon_M}i\kappa_{yM}-\frac{1}{\varepsilon_I}i\kappa_{yI}\right)\left(\frac{1}{\varepsilon_M}i\kappa_{yM}e^{2i\kappa_{yI}d}+\frac{1}{\varepsilon_I}i\kappa_{yI}e^{2i\kappa_{yI}d}\right)=0\end{aligned} \tag{A.14}$$

$$\Updownarrow$$

$$\begin{aligned}&-\frac{1}{\varepsilon_M\varepsilon_I}\kappa_{yM}\kappa_{yI}+\frac{1}{\varepsilon_M^2}\kappa_{yM}^2+\frac{1}{\varepsilon_I^2}\kappa_{yI}^2-\frac{1}{\varepsilon_M\varepsilon_I}\kappa_{yM}\kappa_{yI}\\&-\left(\frac{1}{\varepsilon_M\varepsilon_I}\kappa_{yM}\kappa_{yI}e^{2i\kappa_{yI}d}+\frac{1}{\varepsilon_M^2}\kappa_{yM}^2e^{2i\kappa_{yI}d}+\frac{1}{\varepsilon_I^2}\kappa_{yI}^2e^{2i\kappa_{yI}d}+\frac{1}{\varepsilon_M\varepsilon_I}\kappa_{yM}\kappa_{yI}e^{2i\kappa_{yI}d}\right)=0\end{aligned} \tag{A.15}$$

$$\Updownarrow$$

$$\begin{aligned}&\frac{1}{\varepsilon_I^2}\kappa_{yI}^2+\frac{1}{\varepsilon_M^2}\kappa_{yM}^2-\frac{1}{\varepsilon_I^2}\kappa_{yI}^2e^{2i\kappa_{yI}d}-\frac{1}{\varepsilon_M^2}\kappa_{yM}^2e^{2i\kappa_{yI}d}\\&-\frac{2}{\varepsilon_M\varepsilon_I}\kappa_{yM}\kappa_{yI}-\frac{2}{\varepsilon_M\varepsilon_I}\kappa_{yM}\kappa_{yI}e^{2i\kappa_{yI}d}=0.\end{aligned} \tag{A.16}$$

A.2 Normalization Constant

In this section we wish to evaluate the integral

$$\int_{-\infty}^{\infty}e^{i(k-k')x}dx. \tag{A.17}$$

To do this we consider the integral

$$\lim_{\Delta\to\infty}\int_{k'}\int_{x=-\Delta}^{x=\Delta}e^{-i(k-k')x}f(k')dxdk'=2\pi f(k). \tag{A.18}$$

Here we use the residue theorem to evaluate the integral over x as

$$\int_k\left[\frac{e^{i(k-k')\Delta}-e^{-i(k-k')\Delta}}{i(k-k')}\right]f(k')dk'=2\pi i\frac{e^{i0}}{-i}f(k)=2\pi f(k). \tag{A.19}$$

The fact that the function f is evaluated at k after the integration is the equivalent of having integrated over a delta function and as such we see that the integral (A.17) is equal to $2\pi\delta(k-k')$

A.3 Field Equations

In this section we wish to describe the electric and magnetic field relations for a field propagating in the z direction. Our magnetic field is then on the form

$$\mathbf{H} = \mathbf{H}(x, y)e^{-ik_z z}. \tag{A.20}$$

For such fields it is then clear that we may express the operator $\boldsymbol{\nabla}$ as

$$\boldsymbol{\nabla} = \boldsymbol{\nabla}_s - ik_z\hat{z}. \tag{A.21}$$

In the absence of a current density, $\mathbf{J}$, the electric and magnetic fields are related through Maxwell's equations as

$$\boldsymbol{\nabla} \times \mathbf{E} = -i\omega\mu_0\mathbf{H}, \tag{A.22}$$

$$\boldsymbol{\nabla} \times \mathbf{H} = i\omega\varepsilon_0\varepsilon\mathbf{E}. \tag{A.23}$$

Decomposing Eq. (A.22) into terms for the in-plane component (x, y) and z component yields

$$\boldsymbol{\nabla}_s \times \mathbf{E}_s + \boldsymbol{\nabla}_s \times \hat{z}E_z - ik_z\hat{z} \times \mathbf{E}_s = -i\omega\mu_0(\mathbf{H}_s + \hat{z}H_z) \tag{A.24}$$

$$\Updownarrow$$

$$-i\omega\mu_0\mathbf{H}_s = \boldsymbol{\nabla}_s \times \hat{z}E_z - ik_z\hat{z} \times \mathbf{E}_s. \tag{A.25}$$

Similarly decomposing Eq. (A.23) gives

$$\boldsymbol{\nabla}_s \times \mathbf{H}_s + \boldsymbol{\nabla}_s \times \hat{z}H_z - ik_z\hat{z} \times \mathbf{H}_s = i\omega\varepsilon_0\varepsilon(\mathbf{E}_s + \hat{z}E_z) \tag{A.26}$$

$$\Updownarrow$$

$$i\omega\varepsilon_0\varepsilon\mathbf{E}_s = \boldsymbol{\nabla}_s \times \hat{z}H_z - ik_z\hat{z} \times \mathbf{H}_s. \tag{A.27}$$

We now insert Eq. (A.27) into Eq. (A.25) and obtain

$$\omega^2\mu_0\varepsilon_0\varepsilon\mathbf{H}_s = i\omega\varepsilon_0\varepsilon\boldsymbol{\nabla}_s \times \hat{z}E_z - ik_z\hat{z} \times (\boldsymbol{\nabla}_s \times \hat{z}H_z - ik_z\hat{z} \times \mathbf{H}_s). \tag{A.28}$$

In order to reduce this equation we apply the following relations

$$\hat{z} \times (\hat{z} \times \mathbf{H}_s) = -\mathbf{H}_s, \tag{A.29}$$

$$\hat{z} \times \boldsymbol{\nabla}_s \times \hat{z} = \boldsymbol{\nabla}_s, \tag{A.30}$$

and get that the relation between the fields is given as

$$(k_0^2\varepsilon - k_z^2)\mathbf{H}_s = i\omega\varepsilon_0\varepsilon(-\hat{z}) \times \boldsymbol{\nabla}_s E_z - ik_z\boldsymbol{\nabla}_s H_z \tag{A.31}$$

$$\Updownarrow$$

$$\mathbf{H}_s = \frac{-i}{k_s^2}(k_z\boldsymbol{\nabla}_s H_z + \omega\varepsilon_0\varepsilon\hat{z} \times \boldsymbol{\nabla}_s E_z), \tag{A.32}$$

where $k_s^2 = k_0^2\varepsilon - k_z^2$. Similarly we may insert Eq. (A.25) into Eq. (A.27) and get

$$\omega^2\mu_0\varepsilon_0\varepsilon\mathbf{E}_s = -i\omega\mu_0\boldsymbol{\nabla}_s \times \hat{z}H_z - ik_z\hat{z} \times (\boldsymbol{\nabla}_s \times \hat{z}E_z - ik_z\hat{z} \times \mathbf{E}_s) \tag{A.33}$$

$$\Updownarrow$$

$$(k_0^2\varepsilon - k_z^2)\mathbf{E}_s = i\omega\mu_0\hat{z} \times \boldsymbol{\nabla}_s H_z - ik_z\boldsymbol{\nabla}_s E_z \tag{A.34}$$

$$\Updownarrow$$

$$\mathbf{E}_s = \frac{-i}{k_s^2}(k_z\boldsymbol{\nabla}_s E_z + \omega\mu_0\hat{z} \times \boldsymbol{\nabla}_s H_z). \tag{A.35}$$

From Eqs. (A.32) and (A.35) we see that the in-plane components of the magnetic and electric fields may be described purely from the z components of the electric and magnetic fields.

A.4 Boundary Conditions

In this section we consider the field expressions of Eqs. (A.32) and (A.35). Using the appropriate boundary conditions we derive expressions relating the fields across an interface. Our boundary condition is that the tangential components of the magnetic and electric fields are conserved across the interface. As the surface normal is orthogonal to the tangential part of the field, we may express the boundary condition as

$$\hat{n} \times \mathbf{H}_{1s} = \hat{n} \times \mathbf{H}_{2s}, \tag{A.36}$$

$$\hat{n} \times \mathbf{E}_{1s} = \hat{n} \times \mathbf{E}_{2s}, \tag{A.37}$$

which results in

$$E_{z1} = E_{z2}, \tag{A.38}$$

$$H_{z1} = H_{z2}. \tag{A.39}$$

We now insert Eq. (A.32) into (A.36) and for the sake of transparency we here consider the two terms separately. For the first term we use the vector identity $\mathbf{A} \times (\mathbf{B} \times \mathbf{C}) = \mathbf{B}(\mathbf{A} \cdot \mathbf{C}) - \mathbf{C}(\mathbf{A} \cdot \mathbf{B})$) and get

$$\hat{n} \times (\hat{z} \times \boldsymbol{\nabla}_s) H_z = (\hat{z}\hat{n} \cdot \boldsymbol{\nabla}_s - \boldsymbol{\nabla}_s(\hat{n}\hat{z})) H_z = \hat{z}\hat{n} \cdot \boldsymbol{\nabla}_s H_z, \tag{A.40}$$

while for the second term we use the same vector identity and $\hat{z} \times (\hat{z} \times \mathbf{A}) = -\mathbf{A}$ to get

$$\hat{n} \times \boldsymbol{\nabla}_s E_z = -\hat{n} \times (\hat{z} \times [\hat{z} \times \boldsymbol{\nabla}_s E_z]) \tag{A.41}$$

$$= -\hat{z}(\hat{n}[\hat{z} \times \boldsymbol{\nabla}_s]) - [\hat{z} \times \boldsymbol{\nabla}_s E_z]\hat{n} \cdot \hat{z}, \tag{A.42}$$

where the last term vanishes as $\hat{n}$ is perpendicular to $\hat{z}$. We now use the identity

$$\mathbf{A} \cdot (\mathbf{B} \times \mathbf{C}) = \begin{vmatrix} A_x & A_y & A_z \\ B_x & B_y & B_z \\ C_x & C_y & C_z \end{vmatrix} = \begin{vmatrix} C_x & C_y & C_z \\ A_x & A_y & A_z \\ B_x & B_y & B_z \end{vmatrix} = \mathbf{C} \cdot (\mathbf{A} \times \mathbf{B}), \tag{A.43}$$

and see that

$$\hat{n} \cdot (\hat{z} \times \boldsymbol{\nabla}_s E_z) = (\boldsymbol{\nabla}_s E_z)(\hat{n} \times \hat{z}), \tag{A.44}$$

with $\hat{t} = \hat{n} \times \hat{z}$. For the electric field the tangential component on either side of the interface may then be expressed as

$$\hat{n} \times \mathbf{E}_{1s} = -\frac{ik_z}{k_{s1}^2}(-\hat{z})(\hat{t} \cdot \boldsymbol{\nabla}_s E_z) + \frac{i}{k_{s1}^2}\omega\mu_0 \hat{z}\hat{n} \cdot \boldsymbol{\nabla}_s H_{z1}, \tag{A.45}$$

$$\hat{n} \times \mathbf{E}_{2s} = -\frac{ik_z}{k_{s2}^2}(-\hat{z})(\hat{t} \cdot \boldsymbol{\nabla}_s E_z) + \frac{i}{k_{s2}^2}\omega\mu_0 \hat{z}\hat{n} \cdot \boldsymbol{\nabla}_s H_{z2}. \tag{A.46}$$

In accordance with the boundary condition we equate these two expressions and get

$$\frac{i}{k_{s2}^2}\omega\mu_0\hat{n}\cdot\boldsymbol{\nabla}_s H_{z2} + \frac{ik_z}{k_{s2}^2}\hat{t}\cdot\boldsymbol{\nabla}_s E_z = \frac{i}{k_{s1}^2}\omega\mu_0\hat{n}\cdot\boldsymbol{\nabla}_s H_{z1} + \frac{ik_z}{k_{s1}^2}\hat{t}\cdot\boldsymbol{\nabla}_s E_z \tag{A.47}$$

$$\Updownarrow$$

$$\hat{n}\cdot\boldsymbol{\nabla}_s H_{z2} = \frac{k_{s2}^2}{k_{s1}^2}\hat{n}\cdot\boldsymbol{\nabla}_s H_{z1} + k_z\left(\frac{k_{s2}}{k_{s1}} - 1\right)\frac{1}{\omega\mu_0}\hat{t}\cdot\boldsymbol{\nabla}_s E_z \tag{A.48}$$

$$\Updownarrow$$

$$\hat{n}\cdot\boldsymbol{\nabla}_s H_{z2} = \frac{k_{s2}^2}{k_{s1}^2}\hat{n}\cdot\boldsymbol{\nabla}_s H_{z1} + \frac{k_z}{k_0}\frac{k_0^2(\varepsilon_2-\varepsilon_1)}{k_{s1}^2}\sqrt{\frac{\varepsilon_0}{\mu_0}}\hat{t}\cdot\boldsymbol{\nabla}_s E_z, \tag{A.49}$$

where Eq. (A.49) is our first boundary condition for the fields. Through similar steps we find that

$$\hat{n}\times\mathbf{H}_{1s} = \hat{z}\left(\frac{i}{k_{s1}^2}[k_z\hat{t}\cdot\boldsymbol{\nabla}_s H_z] - \frac{i}{k_{s1}^2}\omega\varepsilon_0\varepsilon_1\hat{n}\cdot\boldsymbol{\nabla}_s E_{z1}\right), \tag{A.50}$$

$$\hat{n}\times\mathbf{H}_{2s} = \hat{z}\left(\frac{i}{k_{s2}^2}[k_z\hat{t}\cdot\boldsymbol{\nabla}_s H_z] - \frac{i}{k_{s2}^2}\omega\varepsilon_0\varepsilon_1\hat{n}\cdot\boldsymbol{\nabla}_s E_{z2}\right). \tag{A.51}$$

Equating Eqs. (A.50) and (A.51) we find that

$$-\frac{i}{k_{s1}^2}\omega\varepsilon_0\varepsilon_1\hat{n}\cdot\boldsymbol{\nabla}_s E_{z1} + \frac{i}{k_{s1}^2}k_z\hat{t}\boldsymbol{\nabla}_s H_z = -\frac{i}{k_{s2}^2}\omega\varepsilon_0\varepsilon_2\hat{n}\cdot\boldsymbol{\nabla}_s E_{z2} + \frac{i}{k_{s2}^2}k_z\hat{t}\boldsymbol{\nabla}_s H_z \tag{A.52}$$

$$\Updownarrow$$

$$\hat{n}\cdot\boldsymbol{\nabla}_s E_{z2} = \frac{k_{s2}^2}{k_{s1}^2}\frac{\varepsilon_1}{\varepsilon_2}\hat{n}\cdot\boldsymbol{\nabla}_s E_{z1} + k_z\left(1 - \frac{k_{s2}^2}{k_{s1}^2}\right)\frac{1}{\omega\varepsilon_0\varepsilon_2}\hat{t}\cdot\boldsymbol{\nabla}_s H_z \tag{A.53}$$

$$\Updownarrow$$

$$\hat{n}\cdot\boldsymbol{\nabla}_s E_{z2} = \frac{k_{s2}^2}{k_{s1}^2}\frac{\varepsilon_1}{\varepsilon_2}\hat{n}\cdot\boldsymbol{\nabla}_s E_{z1} + \frac{k_z}{k_0\varepsilon_2}\frac{k_0^2(\varepsilon_1-\varepsilon_2)}{k_{s1}^2}\sqrt{\frac{\mu_0}{\varepsilon_0}}\hat{t}\cdot\boldsymbol{\nabla}_s H_z, \tag{A.54}$$

where Eq. (A.54) is our second boundary condition for the fields.

A.5 Matrix Element Approximation

In this section, we show how the integral over the normal derivative of the Green's function may be approximated as 1/2. Consider a point close to a surface element as depicted in Fig. A.1.

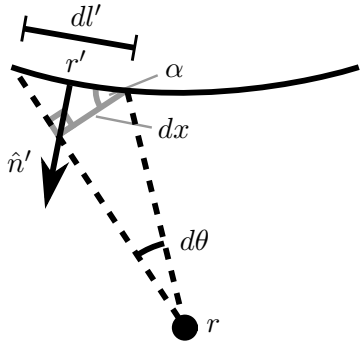

Figure A.1. The geometry of a point r close to a surface point r' used to approximate the normal derivative of the Green's function.

For small $|\mathbf{r}-\mathbf{r}'|$ we have that the Green's function can be approximated as a logarithmic function, i.e.

$$g \approx \frac{-1}{2\pi} \ln\left(\frac{k|\mathbf{r}-\mathbf{r}'|}{2}\right). \tag{A.55}$$

The normal derivative of this function is then given as

$$\hat{n}' \cdot \boldsymbol{\nabla}' g \, dl' = \frac{-1}{2\pi} \frac{\mathbf{r}-\mathbf{r}'}{|\mathbf{r}-\mathbf{r}'|^2} \cdot \hat{n}' dl'. \tag{A.56}$$

The small length dx is given as

$$dx = |\mathbf{r}-\mathbf{r}'| d\theta, \tag{A.57}$$

and the angle α is given as

$$\cos\alpha = -\hat{n}' \cdot \frac{\mathbf{r}-\mathbf{r}'}{|\mathbf{r}-\mathbf{r}'|} = \frac{dx}{dl}. \tag{A.58}$$

Equating Eqs. (A.57) and (A.58) we get

$$-\hat{n}' \cdot \frac{\mathbf{r}-\mathbf{r}'}{|\mathbf{r}-\mathbf{r}'|} = \frac{|\mathbf{r}-\mathbf{r}'| d\theta}{dl'}. \tag{A.59}$$

Rewriting this term we get an expression for the angle θ given as

$$d\theta = -\hat{n}' \cdot \frac{\mathbf{r}-\mathbf{r}'}{|\mathbf{r}-\mathbf{r}'|^2} dl'. \tag{A.60}$$

From this equation we see that if the observation point is close to the surface element, we get an angle of $\theta = \pi$ and we see by inserting this into Eq. (A.56) that the normal derivative of the Green's function may be approximated as $1/2$. Alternatively the angle may be calculated and a better approximation may then be expressed as $\theta/2\pi$.

Results B

This chapter contains all of the results of the reflectance calculations with both the GFSIEM and the SMM. The results are presented in four sections, which correspond to the four sections in the main results chapter, Ch. 4. These sections are GFSIEM with an angle of incidence in the xy plane, SMM with an angle of incidence in the xy plane, GFSIEM with an angle of incidence in the yz plane, and SMM with an angle of incidence in the yz plane. For easier identification graphs are titled in the format *Method, Bottom width of structure, Direction of incidence*. All graphs are plotted with the same axis values to facilitate comparison between the different results.

B.1 GFSIEM, xy Incidence

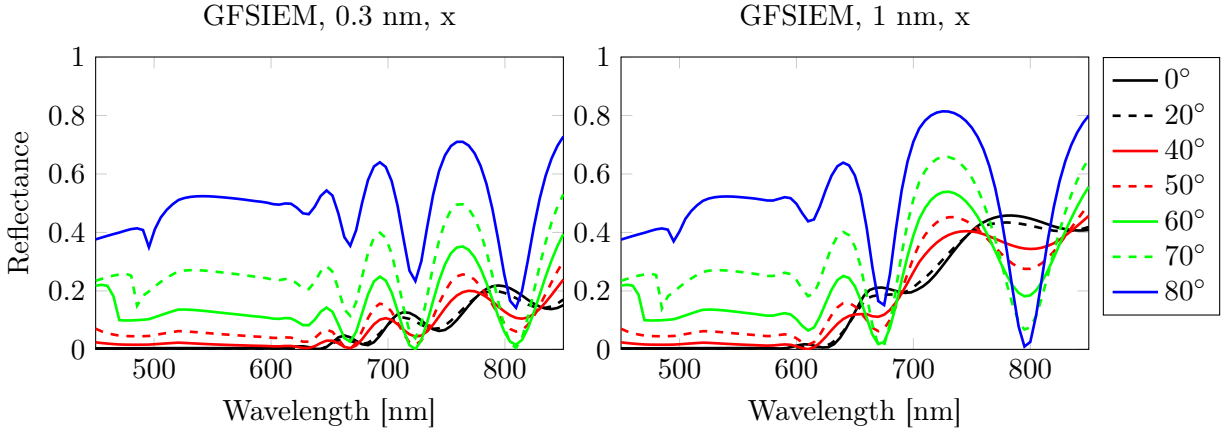

Figure B.1. Reflectances of the structures with bottom widths of 0.3 and 1 nm under angles of incidence in the xy plane as calculated by the GFSIEM.

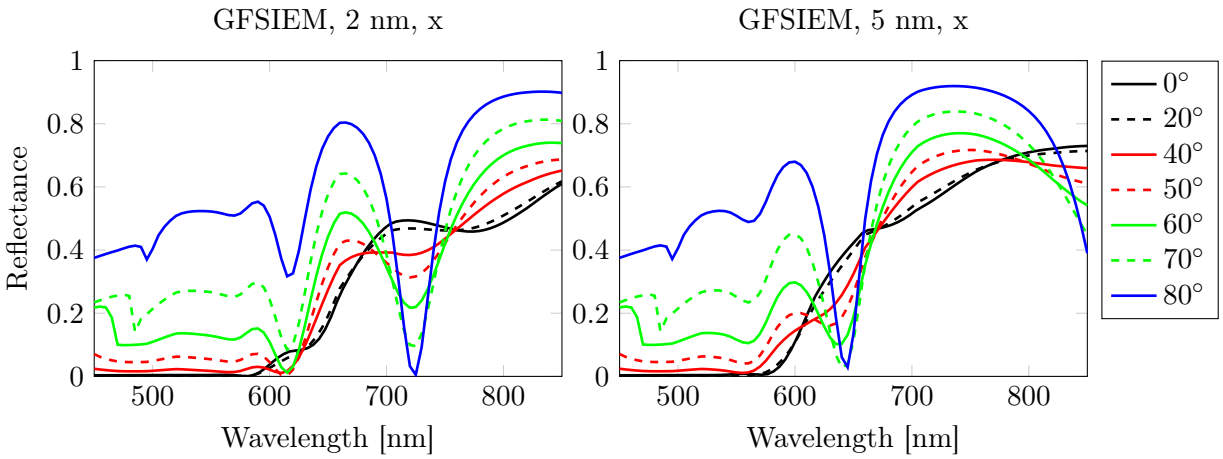

Figure B.2. Reflectances of the structures with bottom widths of 2 and 5 nm under angles of incidence in the xy plane as calculated by the GFSIEM.

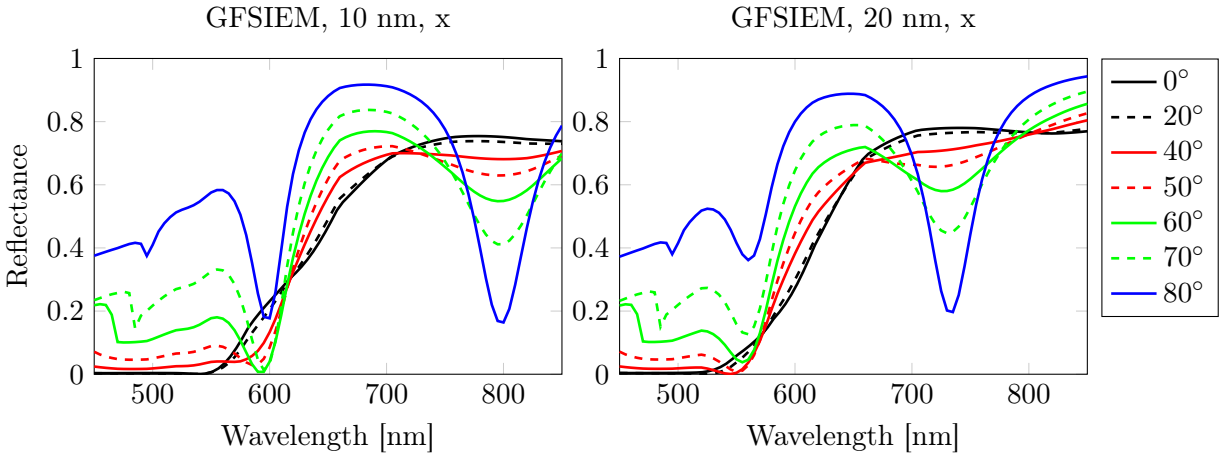

Figure B.3. Reflectances of the structures with bottom widths of 10 and 20 nm under angles of incidence in the xy plane as calculated by the GFSIEM.

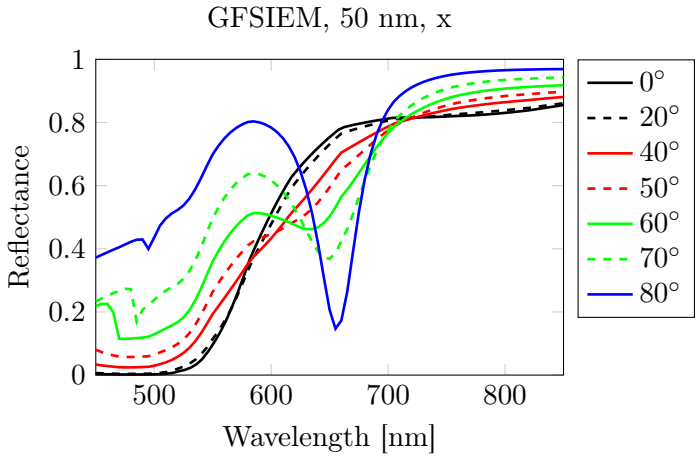

Figure B.4. Reflectances of the structure with a bottom width of 50 nm under angles of incidence in the xy plane as calculated by the GFSIEM.

B.2 SMM, xy Incidence

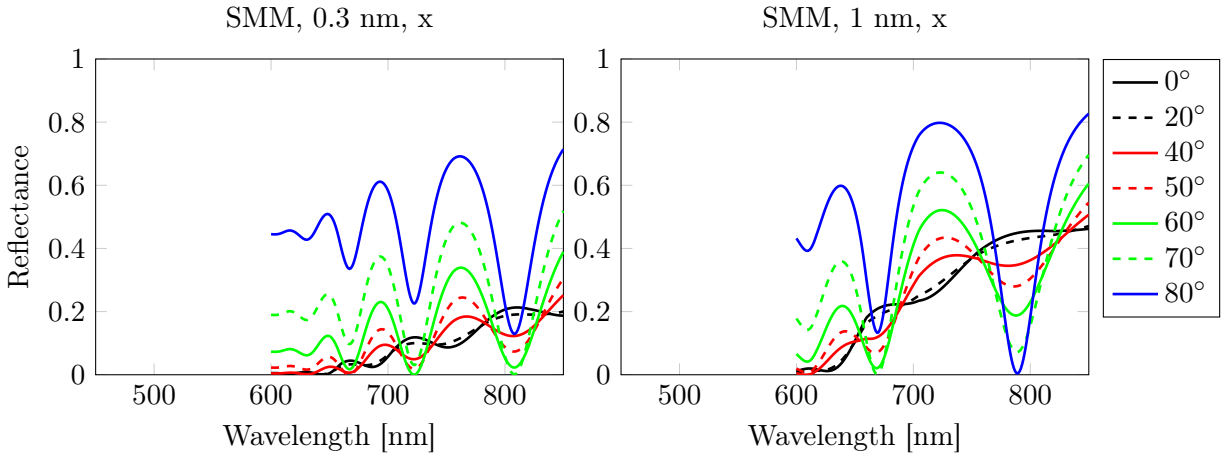

Figure B.5. Reflectances of the structures with bottom widths of 0.3 and 1 nm under angles of incidence in the xy plane as calculated by the SMM.

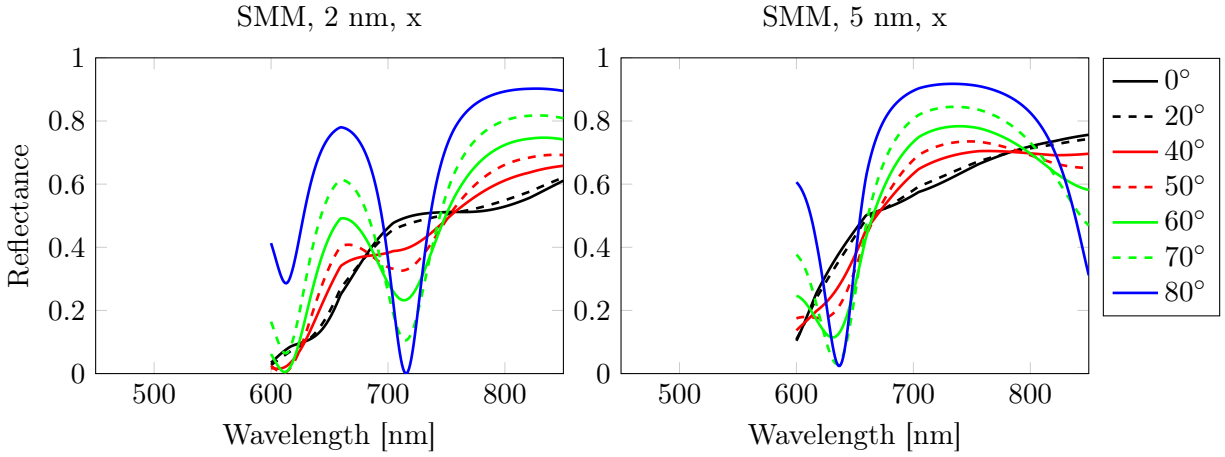

Figure B.6. Reflectances of the structures with bottom widths of 2 and 5 nm under angles of incidence in the xy plane as calculated by the SMM.

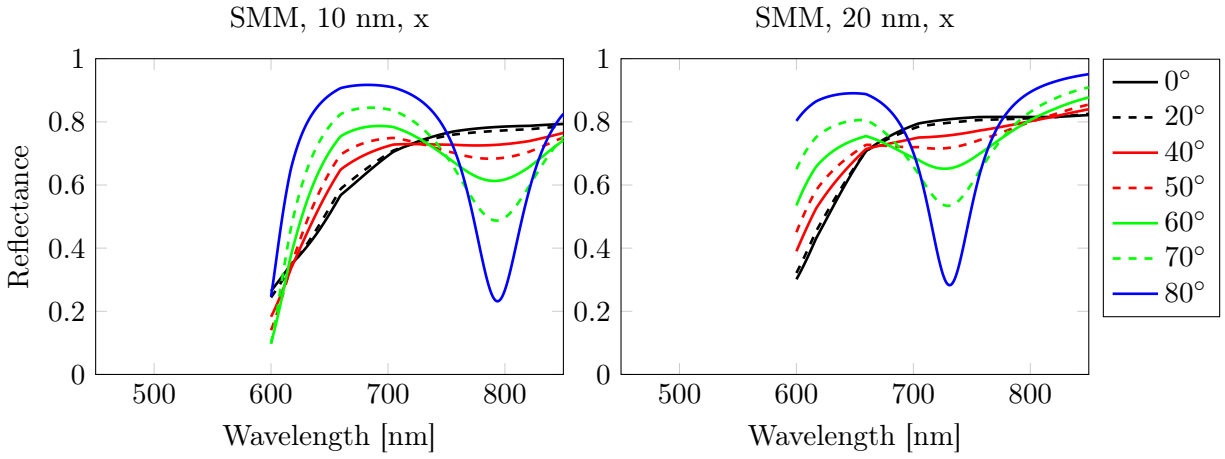

Figure B.7. Reflectances of the structures with bottom widths of 10 and 20 nm under angles of incidence in the xy plane as calculated by the SMM.

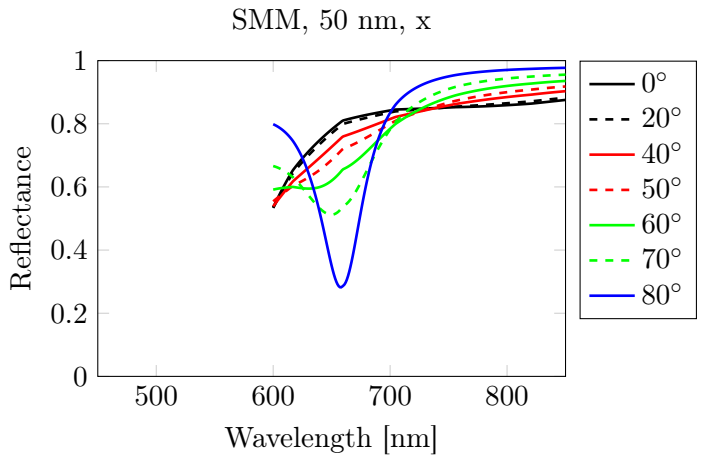

Figure B.8. Reflectances of the structure with a bottom width of 50 nm under angles of incidence in the xy plane as calculated by the SMM.

B.3 GFSIEM, yz Incidence

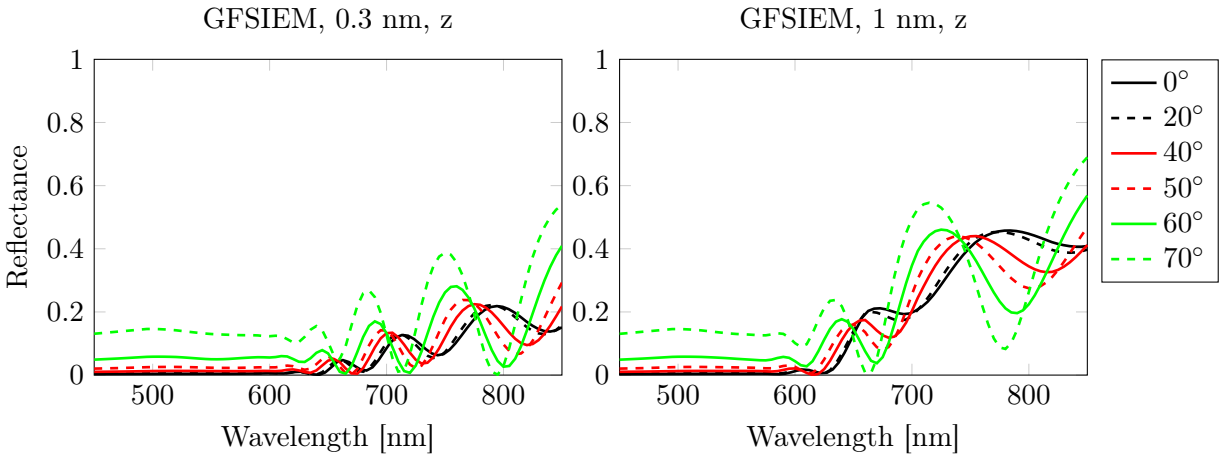

Figure B.9. Reflectances of the structures with bottom widths of 0.3 and 1 nm under angles of incidence in the yz plane as calculated by the GFSIEM.

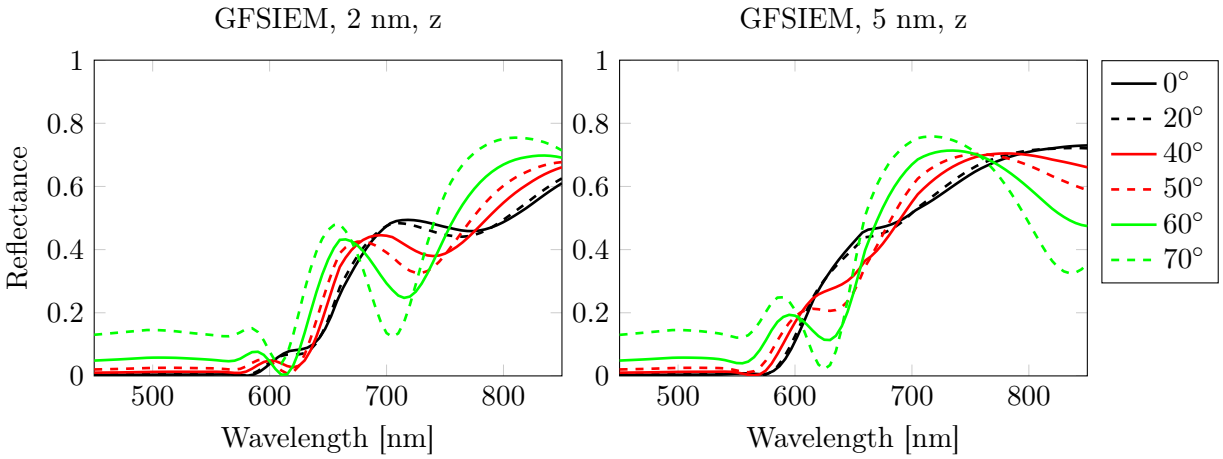

Figure B.10. Reflectances of the structures with bottom widths of 2 and 5 nm under angles of incidence in the yz plane as calculated by the GFSIEM.

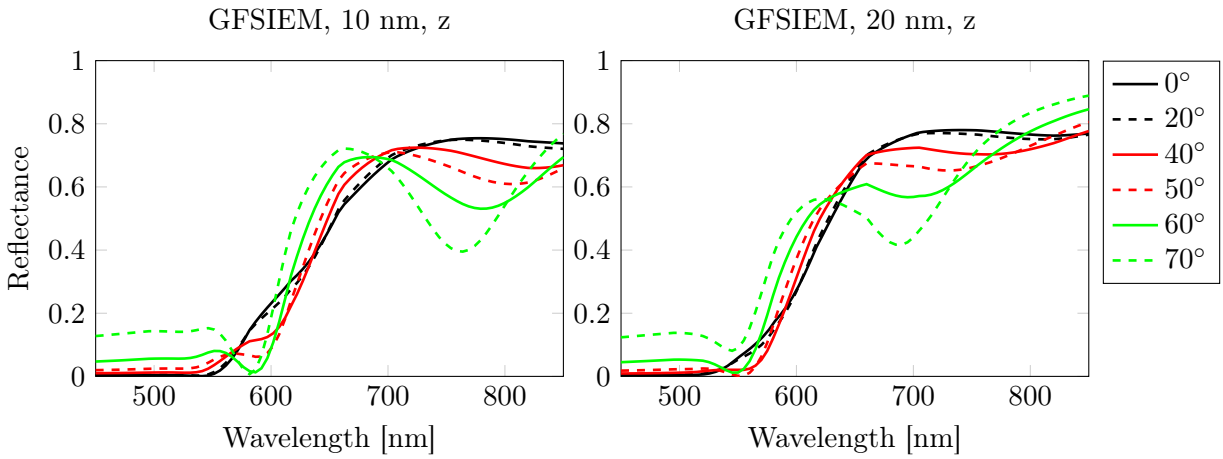

Figure B.11. Reflectances of the structures with bottom widths of 10 and 20 nm under angles of incidence in the yz plane as calculated by the GFSIEM.

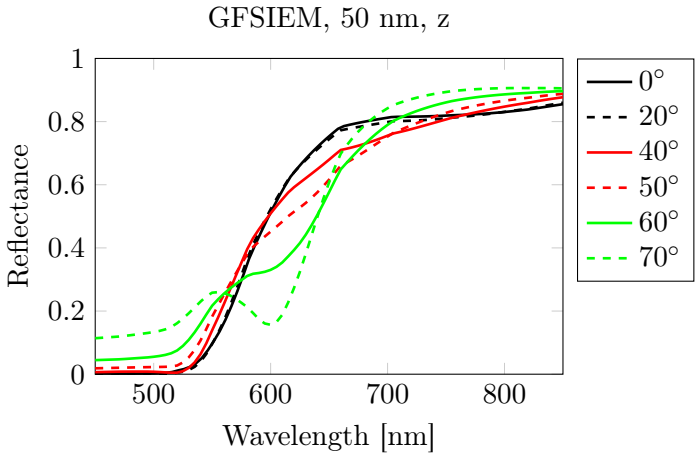

Figure B.12. Reflectances of the structure with a bottom width of 50 nm under angles of incidence in the yz plane as calculated by the GFSIEM.

B.4 SMM, yz Incidence

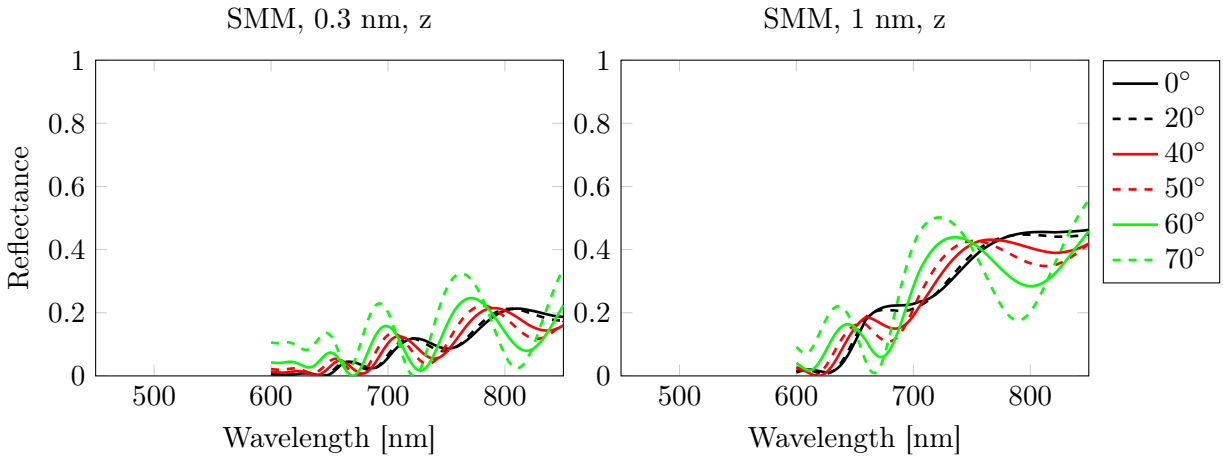

Figure B.13. Reflectances of the structures with bottom widths of 0.3 and 1 nm under angles of incidence in the yz plane as calculated by the SMM.

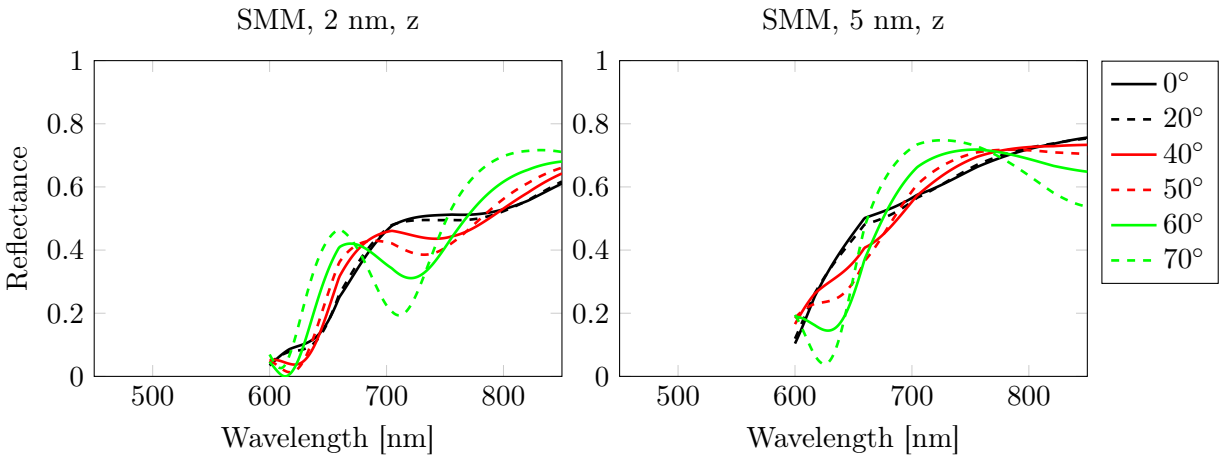

Figure B.14. Reflectances of the structures with bottom widths of 2 and 5 nm under angles of incidence in the yz plane as calculated by the SMM.

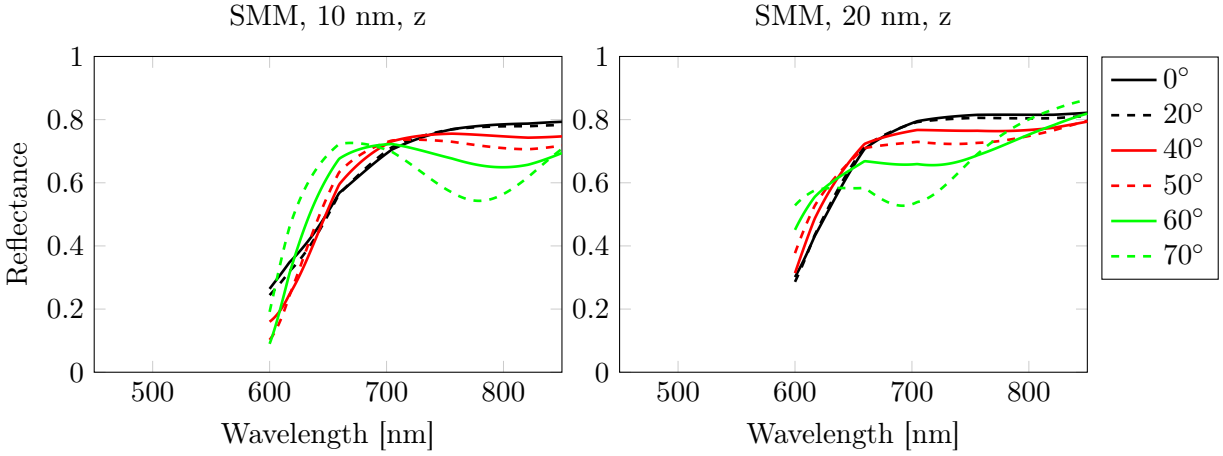

Figure B.15. Reflectances of the structures with bottom widths of 10 and 20 nm under angles of incidence in the yz plane as calculated by the SMM.

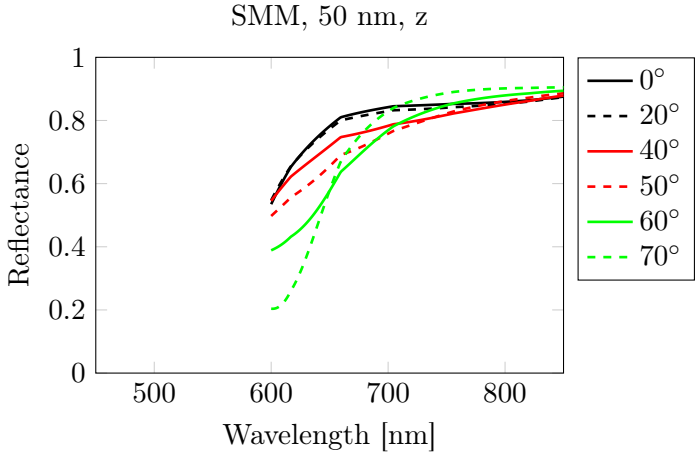

Figure B.16. Reflectances of the structure with a bottom width of 50 nm under angles of incidence in the yz plane as calculated by the SMM.

Modeling the Reflectivity of Plasmonic Ultra-sharp Groove Arrays: General Direction of Light Incidence

Michael Odgaard,[1,2] Mads G. Laursen,[1,2] and Thomas Søndergaard[1,*]

[1] *Department of Physics and Nanotechnology, Aalborg University, Skjernvej 4A, DK-9220 Aalborg Øst, Denmark*

[2] *These authors contributed equally*

compiled: June 3, 2014

The reflectivity of ultra-sharp periodic groove arrays in a gold surface is studied for a general direction of light incidence. This includes the case of incident light propagating along the grooves. Two efficient numerical modeling approaches are presented, namely a simple and approximate stack matrix method that uses the mode-index of gap-plasmon polaritons as an effective index, and a rigorous Green's Function Surface Integral Equation Method (GFSIEM). The results of the highly simple stack matrix method show remarkable similarity to the exact results obtained with the rigorous GFSIEM, which reinforces the idea that the physics of light absorption in such structures is dominated by the coupling of light into plasmons.

OCIS codes: (240.6680) Surface plasmons, (250.5403) Plasmonics, (050.1755) Computational electromagnetic methods, (050.2065) Effective medium theory, (050.6624) Subwavelength structures.

http://dx.doi.org/10.1364/XX.99.099999

1. Introduction

The structuring of metal surfaces on a sub-wavelength scale is interesting for creating materials with absorption selective properties that are useful in fields such as thermophotovoltaics and concentrated solar power. In particular, black materials that are based on metal nanostructures have been the focus of several articles [1–5]. In this paper we are concerned with a so-called plasmonic black metal (PBM) based on a periodic array of ultra-sharp grooves in a metal surface. Such a structure can drastically modify the optical properties of a metal surface for a broad wavelength range from being shiny and highly reflecting into a broadband absorber or black surface [6].

The optical properties of a PBM are strongly connected to the coupling of incident light into gap-surface-plasmon-polaritons (G-SPP's), which are waves propagating in the dielectric gap between the metal groove walls. More specifically, the structures under consideration in this paper are one-dimensionally periodic arrays of ultra-sharp grooves in a gold surface constructed in a way such that they allow for adiabatic nanofocusing of G-SPP's. This is done by designing convex groove walls with slopes such that the reflection for a G-SPP propagating into the groove is minimized [7]. We will consider groove arrays with periods of 250 nm, groove depths of 500 nm, bottom widths in the range of 0.3-50 nm, and a 10 nm plateau between neighboring grooves. It was recently demonstrated that this type of surface may be used as a broadband low-dispersion polarizer for ultra-short laser pulses [8]. In general it is observed that the absorption properties are sensitive to the precise surface geometry and the angle of light incidence. The modeling of these structures when considering a general direction of light incidence is the focus of this paper.

It is common in many theoretical studies of the optics of one-dimensionally periodic gratings to consider only a direction of light incidence in the plane spanned by the surface normal vector and the direction of periodicity (see e.g. [7, 9–14]). This restriction is convenient because it greatly simplifies the theoretical problem. However, this also means that out of convenience a general direction of light incidence on such structures is rarely considered. Some exceptions are that in [15] a general direction of light incidence was considered for non-periodic structures, while for periodic nanostructures the rigorous coupled wave analysis (RCWA) has been applied to a general direction of light incidence, although only for small angles [16].

For the purpose of modeling our periodic arrays of ultra-sharp grooves in a gold surface for a general direction of light incidence we present two efficient numerical methods, namely an approximate Stack Matrix Method (SMM) and a rigorous Green's Function Surface Integral Equation Method (GFSIEM). In the SMM we take advantage of the physical interpretation that wave propagation in the grooves is governed almost entirely by G-SPP waves. On the other hand the GFSIEM is a rigorous and highly efficient method for the modeling of general electromagnetic scattering problems [17–22]. Although the GFSIEM has been extensively used

* Corresponding author: ts@nano.aau.dk

for two-dimensional scattering problems, not much attention has been given to formulating a GFSIEM for solving scattering problems under a general direction of light incidence.

The paper is structured as follows. In Sec. 2 we present a simple SMM for modeling light absorption in ultra-sharp plasmonic grooves. In Sec. 3 we provide the theoretical foundations of a GFSIEM for a general direction of light incidence, and we provide a numerical approach to the solution of the integral equations governing the behaviour of the electric and magnetic fields. In Sec. 4 we compare the reflectivity of periodic arrays of ultra-sharp grooves as calculated with the simple stack matrix method and the exact GFSIEM model. In Sec. 5 we offer our conclusion.

2. Stack Matrix Method

The SMM is a method used to determine the reflectance and transmittance of an optical system consisting of a stack of homogeneous layers with parallel interfaces. While the groove structures considered in this paper do not consist of stacks of parallel layers, we will nevertheless as a simple model represent the structures as stacks of layers with refractive index corresponding to the mode index for a G-SPP propagating in a gap of the same width as the groove width at that layer. This principle is shown in Fig. 1. G-SPP's and the concept of an effective mode index have previously been studied by many groups [23–27]. The idea of using an effective mode index to model the propagation of plasmons with a SMM has been applied previously to model Bragg gratings with weakly bound modes [28, 29].

The basic principles of the SMM are outlined here; for a more thorough description see eg. [30]. Consider a stack of N horizontal parallel layers. In each layer the electric field will be described by the field components E_{dj} and E'_{dj} propagating downwards and the field components E_{uj} and E'_{uj} propagating upwards. The unprimed and primed notations refer to the fields on the upper and lower sides of the layer, respectively. At each interface the fields are subject to reflection and transmission, which is described through the interface transition matrix

$$\mathbf{H}_{ij} = \frac{1}{\tau_{ij}} \begin{bmatrix} 1 & \rho_{ij} \\ \rho_{ij} & 1 \end{bmatrix}, \tag{1}$$

where ρ_{ij} and τ_{ij} are the Fresnel reflection and transmission coefficients between layers i and j. The propagation through a layer is described by the layer propagation matrix

$$\mathbf{L}_j = \begin{bmatrix} \exp(-i\beta_j d_j) & 0 \\ 0 & \exp(i\beta_j d_j) \end{bmatrix}, \tag{2}$$

where d_j is the thickness of layer j, and β_j is a phase factor given as $\beta_j^2 = k_0^2 n_j^2 - k_0^2 n_1^2 \sin^2(\theta)$. Here $k_0 = 2\pi/\lambda_0$, with λ_0 being the wavelength of the incident light, n_j is the refractive index of layer j, and θ is the angle of incidence in the first layer. The matrices $\mathbf{H}_{ij}$ and $\mathbf{L}_j$ for the entire stack of N layers are combined into a single stack matrix

$$\mathbf{H}_{12}\mathbf{L}_2 \ldots \mathbf{H}_{N-2,N-1}\mathbf{L}_{N-1}\mathbf{H}_{N-1,N} = \mathbf{S}_{1N} = \begin{bmatrix} S_{11} & S_{12} \\ S_{21} & S_{22} \end{bmatrix}, \tag{3}$$

which describes the relation between the fields in the incident layer, 1, and the final layer, N, through the equation

$$\begin{bmatrix} E'_{u1} \\ E'_{d1} \end{bmatrix} = \mathbf{S}_{1N} \begin{bmatrix} E_{uN} \\ E_{dN} \end{bmatrix}. \tag{4}$$

As layer N is the final layer of the stack $E_{uN} = 0$, and the relation (4) gives the final reflectance of the entire system as

$$R = \left| \frac{E'_{u1}}{E'_{d1}} \right|^2 = \left| \frac{S_{12}}{S_{22}} \right|^2. \tag{5}$$

An effective mode index for a G-SPP in a part of the groove of width d can be found as follows. Consider a G-SPP propagating in the x direction along a dielectric material sandwiched between two parallel metal surfaces located at $y = 0$ and $y = d$, respectively. The propagating G-SPP is p polarized, and as such the corresponding field can be expressed as $\mathbf{H} = \hat{z}H$. The magnetic field as a function of x and y can be written as

$$H(x, y) = \exp(-ik_{\text{G-SPP}}\, x) f(y), \tag{6}$$

where $f(y)$ is an appropriate function describing the variation in the y-direction, and $k_{\text{G-SPP}}$ is the propagation constant of the G-SPP. $k_{\text{G-SPP}}$ can be expressed as $k_{\text{G-SPP}} = n_m k_0$, where n_m is the effective mode index of the G-SPP. With appropriate boundary conditions and constructions of the function $f(y)$ we arrive at the following expression, which can be solved on a computer to determine the mode index:

$$[1 - \exp(2i\kappa_{yI} d)] \left(\frac{\kappa_{yI}^2}{\varepsilon_I^2} + \frac{\kappa_{yM}^2}{\varepsilon_M^2} \right) - \frac{2\kappa_{yM}\kappa_{yI}}{\varepsilon_M \varepsilon_I} [1 + \exp(2i\kappa_{yI} d)] = 0, \tag{7}$$

where $\kappa_{yM} = (k_0^2 \varepsilon_M - k_{\text{G-SPP}}^2)^{1/2}$ and $\kappa_{yI} = (k_0^2 \varepsilon_I - k_{\text{G-SPP}}^2)^{1/2}$, with ε_M and ε_I being the dielectric constants of the metal and the dielectric, respectively. The expression given in (7) was used as the starting point for the mode index calculations performed in relation to the present work. These calculations were done by calculating the value of the left-hand side of (7) for a range of different values of $k_{\text{G-SPP}}$. When a value relatively close to 0 was identified through sign changes in the real and imaginary parts, the actual solution was approached using the Newton-Raphson method. In this way we found the effective mode index for the fundamental G-SPP propagating in an air layer between two gold interfaces for a large number of gap thicknesses in

the range of 0.3-250 nm at wavelengths in the range of 600-850 nm. For specific examples of the mode index see [7]. At shorter wavelengths (below 550 nm) the approach with an effective mode index for a G-SPP between two gold interfaces can no longer be used, since gold behaves as a dielectric at these wavelengths and as such the geometry no longer supports G-SPPs.

After constructing the multilayer structure used as a representation of the groove by the principle shown in Fig. 1 the reflectance at normal incidence was simply calculated by applying the SMM to the constructed multilayer structure. For incidence at an angle to the normal direction we treated the problem differently depending on the direction of incidence. In the calculations for an angle of incidence in the xy plane the light was treated as p polarized light, but in all layers except the incident (air) layer the angle of incidence was set to 0 as illustrated in Fig. 1. Thus, the in-plane wave number is not conserved across the first interface as it would be for stacks of layers with parallel interfaces. This affects the reflection and transmission coefficients, which instead of the usual Fresnel coefficients become

$$\rho_{12} = \frac{(n_2/n_1)\cos(\theta) - 1}{(n_2/n_1)\cos(\theta) + 1}, \tag{8}$$

$$\tau_{12} = 1 + \rho_{12}. \tag{9}$$

This represents the physical interpretation that the incident light couples to a G-SPP, which propagates straight down into the groove. In the calculations for an angle of incidence in the yz plane the in-plane wave number, $k_z = k_0 n_1 \sin(\theta)$, must be conserved through all layers, because the structure is invariant along the z axis. Here, however, the light was treated as s polarized in the SMM. This can be justified by the fact that the main component of the electric field of the G-SPP will be oriented as shown in Fig. 2. The G-SPP will also have a smaller electric field component in the direction of propagation. However, it is curious that waves (G-SPP's) which are inherently p polarized must be modeled using s polarization. The ray path shown in Fig. 2 can be understood in a geometric optics picture and follows from Snell's law and the increasing mode index [31].

An important concern with regards to the usage of the SMM for the calculation of the reflectance of the sharp groove structures is the fact that the mode index for a gap plasmon rapidly approaches very large values at small gap thicknesses and does not approach the refractive index of gold in the limit of $d \to 0$. Thus the final stack of layers would contain layers with very large mode indices, which would suddenly jump to the refractive index of gold when reaching the bottom of the stack. For this reason we chose to only include layers for gap thicknesses down to 0.3 nm in order to avoid extremely large values of the mode index in the last layers.

In order to further approach a complete model for the reflectance of the system we introduced an additional reflection phase in the reflection coefficient between the final layer and the gold substrate. The appropriate value

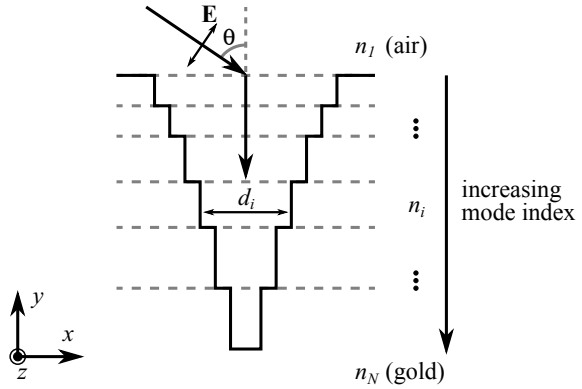

Fig. 1. The principle used to convert one period of the groove structure into a multilayer structure to be used in the SMM. The figure also shows the physical interpretation of light incidence under an angle in the xy plane used in the SMM.

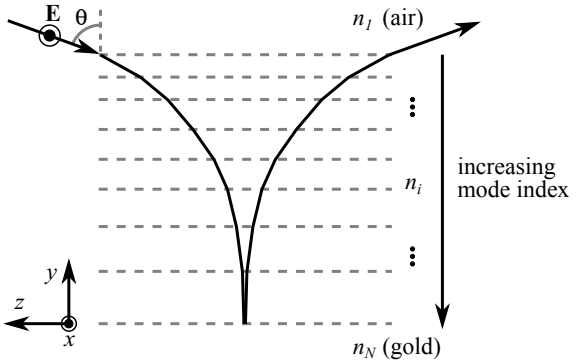

Fig. 2. The physical interpretation of light incidence under an angle in the yz plane used in the SMM. For simplicity reflections at interfaces other than the last are omitted in the figure.

of this reflection phase was assumed to be close to that for the reflection of a plane wave incident on an air-gold interface, and as such we modeled the final reflection in the stack matrix ($\mathbf{H}_{N-1,N}$) as a reflection between air and gold. We performed calculations where this reflection occurred under normal incidence as well as under angles corresponding to the incident angle or the angle that would be obtained in the final layer by applying Snell's law at each interface of the stack of layers. The results of these calculations were found to deviate only slightly from each other, and as such we chose to model it as normal incidence.

3. Green's Function Surface Integral Equation Method

The strength of the GFSIEM [32] has been demonstrated in several applications ranging from simple scattering configurations [17–22] to more complex periodic structures [33, 34]. Here we introduce a rigorous method for solving scattering problems for a general direction of light incidence, which has not previously been given a lot of attention.

Consider a scattering structure with a surface as shown in Fig. 3. For propagation in the xy plane and either s or p polarization the electric or magnetic field will only have a z component, and the other field will be perpendicular to the z axis, which greatly simplifies the problem to a formulation with only one scalar field component. This is no longer the case for a general direction of light incidence. However, two scalar field components are sufficient. Due to the translational invariance along the z axis and periodicity along the x axis the fields can be decomposed into Bloch waves of the form

$$\mathbf{E}(\mathbf{r}) = \mathbf{U}_E(\boldsymbol{\rho}; k_x, k_z)e^{-ik_x x}e^{-ik_z z}, \tag{10}$$

$$\mathbf{H}(\mathbf{r}) = \mathbf{U}_H(\boldsymbol{\rho}; k_x, k_z)e^{-ik_x x}e^{-ik_z z}, \tag{11}$$

where $\mathbf{U}_{j=E,H}$ is a periodic function satisfying $\mathbf{U}_j(\boldsymbol{\rho} + \hat{x}\Lambda) = \mathbf{U}_j(\boldsymbol{\rho})$ with Λ being the period of the structure, $\boldsymbol{\rho} = \hat{x}x + \hat{y}y$, and $\mathbf{r} = \hat{x}x + \hat{y}y + \hat{z}z$. We see that there are three components for both the magnetic field and the electric field. However, by inserting these expressions for the fields into Maxwell's equations it can be shown that the x and y components of the fields may be described purely from the z component of the magnetic and electric fields. We then get for the in-plane components of $\mathbf{H}$ and $\mathbf{E}$, $\mathbf{H}_s$ and $\mathbf{E}_s$, [35]

$$\mathbf{H}_s(\boldsymbol{\rho}) = \frac{-i}{k_s^2}[k_z \boldsymbol{\nabla}_s H_z + \omega\varepsilon_0\varepsilon\hat{z} \times \boldsymbol{\nabla}_s E_z], \tag{12}$$

$$\mathbf{E}_s(\boldsymbol{\rho}) = \frac{-i}{k_s^2}[k_z \boldsymbol{\nabla}_s E_z + \omega\mu_0\hat{z} \times \boldsymbol{\nabla}_s E_z], \tag{13}$$

where

$$k_s^2 = k_0^2\varepsilon - k_z^2, \tag{14}$$

$$\boldsymbol{\nabla}_s = \hat{x}\frac{\partial}{\partial x} + \hat{y}\frac{\partial}{\partial y}. \tag{15}$$

The z components of the fields must satisfy the scalar wave equation, i.e.

$$\nabla^2 E_z + k_0^2\varepsilon E_z = \nabla_s^2 E_z + k_s^2 E_z = 0. \tag{16}$$

In addition to the electric and magnetic fields, the field due to a point source is considered in each material,

$$(\nabla_s^2 + k_{si}^2)g_i(\boldsymbol{\rho}; \boldsymbol{\rho}') = -\delta(\boldsymbol{\rho} - \boldsymbol{\rho}'). \tag{17}$$

Here $k_{si}^2 = k_0^2\varepsilon_i - k_z^2$ with ε_i being the dielectric constant of material i, and g_i is the appropriate Green's function in material i. For a structure with periodicity in the x direction a solution for g_i that satisfies the radiating boundary condition along y and the Bloch boundary condition along x can be constructed through mode expansion as

$$g_i(\mathbf{r}, \mathbf{r}') = \frac{-i}{4\pi}\sum_n \frac{e^{-i(k_x - nG)(x-x')}e^{-ik_{yi,n}|y-y'|}}{k_{yi,n}}G. \tag{18}$$

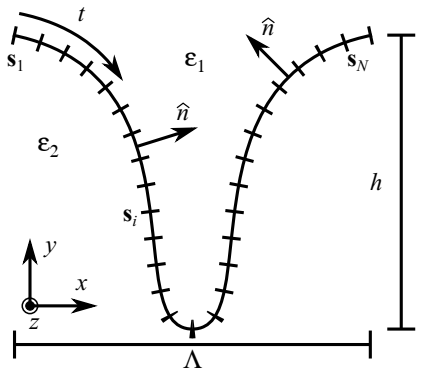

Fig. 3. The surface of a scattering structure divided into surface elements. For the periodic scattering problem considered here, the figure represents a single period, Λ, of the structure.

Here k_x is the Bloch wave number in the direction in which the structure is periodic, $G = 2\pi/\Lambda$ with Λ being the period of the structure, and $k_{yi,n} = [k_{si}^2 - (kx - nG)^2]^{1/2}$ with $\mathrm{Im}(k_{yi,n}) \leq 0$. Similar to the case of $k_z = 0$ (see e.g. [32]) we can obtain the integral equations

$$E_z(\boldsymbol{\rho}) = \begin{cases} E_{z0}(\boldsymbol{\rho}) - \oint \{g_1(\boldsymbol{\rho}; \boldsymbol{\rho}')\hat{n}' \cdot \boldsymbol{\nabla}' E_z(\boldsymbol{\rho}') \\ -E_z(\boldsymbol{\rho}')\hat{n}' \cdot \boldsymbol{\nabla}' g_1(\boldsymbol{\rho}; \boldsymbol{\rho}')\}dl' & \boldsymbol{\rho} \in \Omega_1 \\ \\ \oint \{g_2(\boldsymbol{\rho}; \boldsymbol{\rho}')\hat{n}' \cdot \boldsymbol{\nabla}' E_z(\boldsymbol{\rho}') \\ -E_z(\boldsymbol{\rho}')\hat{n}' \cdot \boldsymbol{\nabla}' g_2(\boldsymbol{\rho}; \boldsymbol{\rho}')\}dl' & \boldsymbol{\rho} \in \Omega_2, \end{cases} \tag{19}$$

$$H_z(\boldsymbol{\rho}) = \begin{cases} H_{z0}(\boldsymbol{\rho}) - \oint \{g_1(\boldsymbol{\rho}; \boldsymbol{\rho}')\hat{n}' \cdot \boldsymbol{\nabla}' H_z(\boldsymbol{\rho}') \\ -H_z(\boldsymbol{\rho}')\hat{n}' \cdot \boldsymbol{\nabla}' g_1(\boldsymbol{\rho}; \boldsymbol{\rho}')\}dl' & \boldsymbol{\rho} \in \Omega_1 \\ \\ \oint \{g_2(\boldsymbol{\rho}; \boldsymbol{\rho}')\hat{n}' \cdot \boldsymbol{\nabla}' H_z(\boldsymbol{\rho}') \\ -H_z(\boldsymbol{\rho}')\hat{n}' \cdot \boldsymbol{\nabla}' g_2(\boldsymbol{\rho}; \boldsymbol{\rho}')\}dl' & \boldsymbol{\rho} \in \Omega_2. \end{cases} \tag{20}$$

Here Ω_1 and Ω_2 refer to positions outside and inside the metal, respectively (dielectric constants ε_1 and ε_2), and E_{z0} and H_{z0} are the incident fields. Inserting Eqs. (12) and (13) into the boundary conditions $\hat{n} \times \mathbf{H}_1 = \hat{n} \times \mathbf{H}_2$

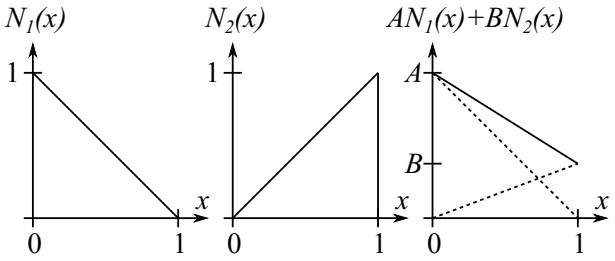

Fig. 4. The weight functions used in constructing linearly varying fields in each surface element.

and $\hat{n} \times \mathbf{E}_1 = \hat{n} \times \mathbf{E}_2$ we get

$$E_{z1} = E_{z2}, \tag{21}$$

$$H_{z1} = H_{z2}, \tag{22}$$

$$\hat{n} \cdot \boldsymbol{\nabla} H_{z2} = \hat{n} \cdot \boldsymbol{\nabla} H_{z1} \frac{k_0^2 \varepsilon_2 - k_z^2}{k_0^2 \varepsilon_1 - k_z^2} - \hat{t} \cdot \boldsymbol{\nabla} E_{z1} \frac{k_z}{k_0} \sqrt{\frac{\varepsilon_0}{\mu_0}} \frac{k_0^2(\varepsilon_1 - \varepsilon_2)}{k_0^2 \varepsilon_1 - k_z^2}, \tag{23}$$

$$\hat{n} \cdot \boldsymbol{\nabla} E_{z2} = \hat{n} \cdot \boldsymbol{\nabla} E_{z1} \frac{\varepsilon_1}{\varepsilon_2} \frac{k_0^2 \varepsilon_2 - k_z^2}{k_0^2 \varepsilon_1 - k_z^2} - \hat{t} \cdot \boldsymbol{\nabla} H_{z1} \frac{k_z}{k_0} \sqrt{\frac{\mu_0}{\varepsilon_0}} \frac{k_0^2(\varepsilon_2 - \varepsilon_1)}{k_0^2 \varepsilon_1 - k_z^2}. \tag{24}$$

We see that in the case of $k_z \neq 0$ there is a coupling between H_z and E_z, and if $k_z = 0$ Eqs. (23) and (24) reduce to $\hat{n} \cdot \boldsymbol{\nabla} H_{z2} = \hat{n} \cdot \boldsymbol{\nabla} H_{z1} \varepsilon_2/\varepsilon_1$ and $\hat{n} \cdot \boldsymbol{\nabla} E_{z2} = \hat{n} \cdot \boldsymbol{\nabla} E_{z1}$, in which case there is no coupling, and it is sufficient to consider each field separately, greatly reducing the complexity of the problem. In this case the integral equations can be solved by a numerical approach, in which the fields and their normal derivatives are considered constant in each surface element. However, for the case of $k_z \neq 0$ where there is a coupling between H_z and E_z this representation of the fields is inadequate for describing the tangential derivative in Eqs. (23) and (24). In order to expand the model to account for the tangential derivative, we introduce a linear variation of the fields in each element by combining two weight functions $N1$ and $N2$ as shown in Fig. 4. The field along a surface element may then be described as

$$E_z(\mathbf{s}) = E_z(\mathbf{s}(t)) \approx \sum_{i=1}^{N} E_{z,i}^{(s)} N_1 \left(\frac{t - t_i^{(s)}}{L_i} \right) + E_{z,i}^{(e)} N_2 \left(\frac{t - t_i^{(s)}}{L_i} \right), \tag{25}$$

where $\mathbf{s} = \mathbf{s}(t)$ is a position along the surface, with t being the distance along the surface from a starting point (see Fig. 3), $t_i^{(s)}$ is the start point of element i, L_i is the length of element i, and $E_{z,i}^{(s)}$ and $E_{z,i}^{(e)}$ are the values of E_z in the start and end points of surface element i, respectively. The magnetic fields are constructed using the same weight functions. The tangential derivative, $\hat{t} \cdot \boldsymbol{\nabla} E_z$ at all sampling points $t_i^{(s)}$ given as a column vector $\bar{t}_E$, can then be approximated as the average slope of the field values in neighboring surface elements

$$\bar{t}_E = \overline{\overline{T}}\, \overline{E}_z^{(s)}, \tag{26}$$

where $\overline{\overline{T}}$ is a matrix constructed from a finite-difference scheme using nearest neighbor sampling points. Another convenient matrix can be constructed by considering that the end point of surface element i is the start point of element $(i+1)$. That is

$$\overline{E}_z^{(e)} = \overline{\overline{D}}\, \overline{E}_z^{(s)}, \tag{27}$$

where $\overline{E}_z^{(s)}$ and $\overline{E}_z^{(s)}$ are column vectors containing all of the values $E_{z,i}^{(s)}$ and $E_{z,i}^{(e)}$, and the matrix $\overline{\overline{D}}$ is of the form

$$\overline{\overline{D}} = \begin{bmatrix} 0 & 1 & 0 & 0 & \dots & 0 \\ 0 & 0 & 1 & 0 & \dots & 0 \\ \vdots & \vdots & \vdots & \vdots & \ddots & \vdots \\ 0 & 0 & 0 & 0 & \dots & 1 \\ 1 & 0 & 0 & 0 & \dots & 0 \end{bmatrix}. \tag{28}$$

The matrix describing the magnetic and electric fields governed by Eqs. (19) and (20) is then constructed as

$$\begin{bmatrix} \overline{E}_{z,0}^{(s)} \\ \overline{0} \\ \overline{H}_{z,0}^{(s)} \\ \overline{0} \end{bmatrix} = \begin{bmatrix} \overline{\overline{B}}_1 & \overline{\overline{A}}_1 & \overline{\overline{0}} & \overline{\overline{0}} \\ \overline{\overline{B}}_2 & -\overline{\overline{A}}_2 f_1 & \overline{\overline{A}}_2 \overline{\overline{T}} f_2 & \overline{\overline{0}} \\ \overline{\overline{0}} & \overline{\overline{0}} & \overline{\overline{B}}_1 & \overline{\overline{A}}_1 \\ \overline{\overline{A}}_2 \overline{\overline{T}} f_4 & \overline{\overline{0}} & \overline{\overline{B}}_2 & -\overline{\overline{A}}_2 f_3 \end{bmatrix} \begin{bmatrix} \overline{E}_z^{(s)} \\ \overline{\phi}_E^{(s)} \\ \overline{H}_z^{(s)} \\ \overline{\phi}_H^{(s)} \end{bmatrix}, \tag{29}$$

where

$$f_1 = \frac{\varepsilon_1}{\varepsilon_2} \frac{k_0^2 \varepsilon_2 - k_z^2}{k_0^2 \varepsilon_1 - k_z^2}, \tag{30}$$

$$f_2 = \frac{k_z}{k_0} \frac{1}{\varepsilon_2} \frac{k_0^2(\varepsilon_2 - \varepsilon_1)}{k_0^2 \varepsilon_1 - k_z^2}, \tag{31}$$

$$f_3 = \frac{k_0^2 \varepsilon_2 - k_z^2}{k_0^2 \varepsilon_1 - k_z^2}, \tag{32}$$

$$f_4 = \frac{k_z}{k_0} \frac{k_0^2(\varepsilon_1 - \varepsilon_2)}{k_0^2 \varepsilon_1 - k_z^2}, \tag{33}$$

$$\overline{\overline{B}}_1 = \left(\frac{1}{2} \overline{\overline{I}} - \overline{\overline{B}}^{(1,1)} - \overline{\overline{B}}^{(1,2)} \overline{\overline{D}} \right), \tag{34}$$

$$\overline{\overline{A}}_1 = \left(\overline{\overline{A}}^{(1,1)} + \overline{\overline{A}}^{(1,2)} \overline{\overline{D}} \right), \tag{35}$$

$$\overline{\overline{B}}_2 = \left(\frac{1}{2} \overline{\overline{I}} + \overline{\overline{B}}^{(2,1)} + \overline{\overline{B}}^{(2,2)} \overline{\overline{D}} \right), \tag{36}$$

$$\overline{\overline{A}}_2 = \left(\overline{\overline{A}}^{(2,1)} + \overline{\overline{A}}^{(2,2)} \overline{\overline{D}} \right), \tag{37}$$

and

$$A_{i,j}^{(u,v)} = P \int g_u(\mathbf{s}_i, \mathbf{s}(t'))N_v \left(\frac{t' - t_j^{(s)}}{L_j} \right) dt', \tag{38}$$

$$B_{i,j}^{(u,v)} = P \int [\hat{n}' \cdot \boldsymbol{\nabla}' g_u(\mathbf{s}_i, \mathbf{r}')]_{\mathbf{r}'=\mathbf{s}(t')} N_v \left(\frac{t' - t_j^{(s)}}{L_j} \right) dt'. \tag{39}$$

The P's in Eqs. (38) and (39) indicate that the integrals must be calculated as principal value integrals. These integrals are calculated numerically as sums in which the singular point of the integrand is excluded from the integral. Because the period of the considered structures will be sufficiently small compared to the wavelength, the final reflectance can be found as the squared ratio between the magnitude of the scattered far-field and that of the incident field.

4. Results

In this section we present results produced with the simple SMM and the GFSIEM as described in the previous sections. The structure coordinates used for these calculations are produced in the same way as those presented in [7]. In all of the calculations we used the dielectric constant of gold from [36]. We show reflectance spectra calculated with both the SMM and the GFSIEM for angles of incidence in both the xy plane and the yz plane for structures with different bottom groove widths.

Fig. 5 shows the reflectance spectra calculated with both methods for the structure with a bottom width of 0.3 nm under angles of incidence in the xy plane. We see a very high degree of similarity between the results of the exact GFSIEM and those of our SMM in both the position and magnitude of the reflectance peaks. For the larger angles of incidence the reflectance graphs calculated with the SMM are almost identical to those of the GFSIEM. Even at smaller angles of incidence the differences between the results are surprisingly minor, considering the simplicity of the SMM. Note that the procedures used at the first interface as described in Eqs. (8) and (9) and at the last interface are crucial in order to obtain good agreement between the two methods. Note also that in this case $k_x = k_0 n_1 \sin(\theta)$ and $k_z = 0$ in the GFSIEM.

The reflectance spectra obtained for the same structure with a bottom width of 0.3 nm under an angle of incidence in the yz plane ($k_x = 0$, $k_z \neq 0$) are shown in Fig. 6. In these results we also see clear similarities between the results of the GFSIEM and those of the SMM. These are also the first results presented for light incidence along the non-periodic direction of this periodic structure. Of particular note in these results is the fact that the reflectance minima are shifted to shorter wavelengths with an increasing angle, whereas the positions of the minima are largely unaffected by the angle of incidence in the xy plane. The reflectance minima for an angle of incidence in the xy plane are attributed to resonances in the groove, which are unaffected by the

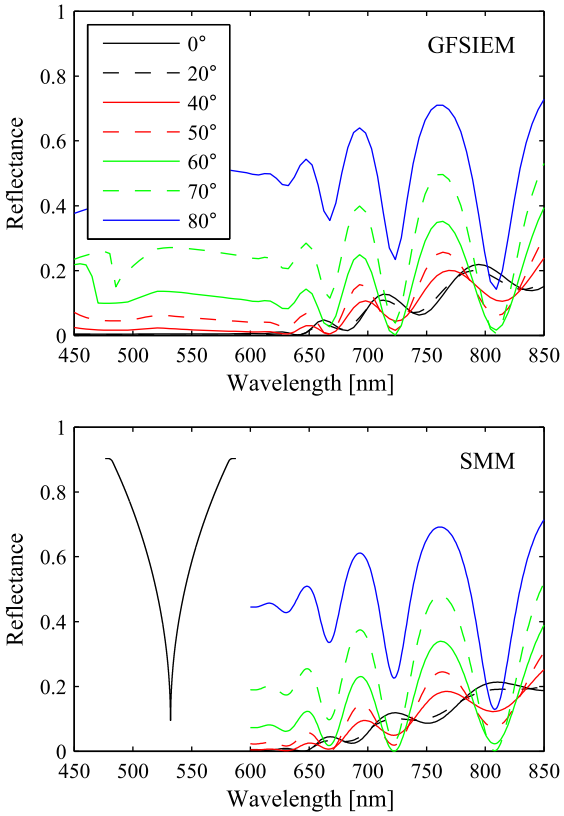

Fig. 5. (Color online) GFSIEM and SMM results for the reflectance of the structure with a bottom width of 0.3 nm ($\Lambda = 250$ nm, $h = 500$ nm) under angles of incidence in the xy plane. The inset on the left-hand side of the bottom figure shows one period of the actual structure.

details of the coupling of the incident light to plasmons. The difference observed for an angle of incidence in the yz plane is caused by the fact that an increasing angle of incidence in this direction increases the magnitude of k_z, which in turn reduces k_s, cf. Eq. (14). The reduction of k_s naturally leads to a shift in resonances towards shorter wavelengths. Note here that the choice of s polarization in the SMM is crucial in order to obtain good agreement with the exact method. If p polarization is used, the maxima and minima in the reflectance spectra will shift to different wavelengths.

We performed similar reflectance calculations for structures with bottom widths of 1, 2, 5, 10, 20, and 50 nm. The results of the calculations performed on the structure with a bottom width of 10 nm are shown in Figs. 7 and 8, which show the results for angles of incidence in the xy plane and the yz plane, respectively. Similar to the previously presented results for the structure with a bottom width of 0.3 nm we see a very high degree of similarity between the results obtained with the two methods. Once again the reflectance minima are seen to be unaffected by angle of incidence in the xy plane while they are shifted towards shorter wavelengths

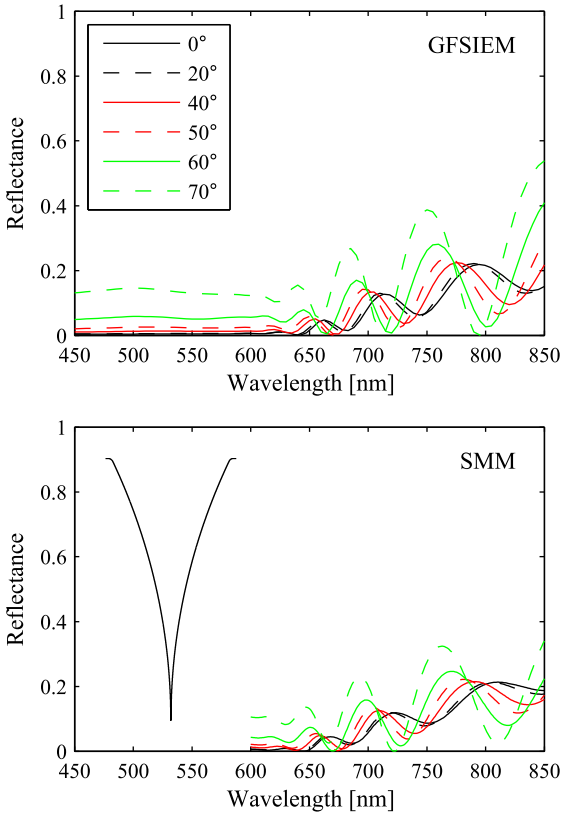

Fig. 6. (Color online) GFSIEM and SMM results for the reflectance of the structure with a bottom width of 0.3 nm ($\Lambda = 250$ nm, $h = 500$ nm) under angles of incidence in the yz plane. The inset on the left-hand side of the bottom figure shows one period of the actual structure.

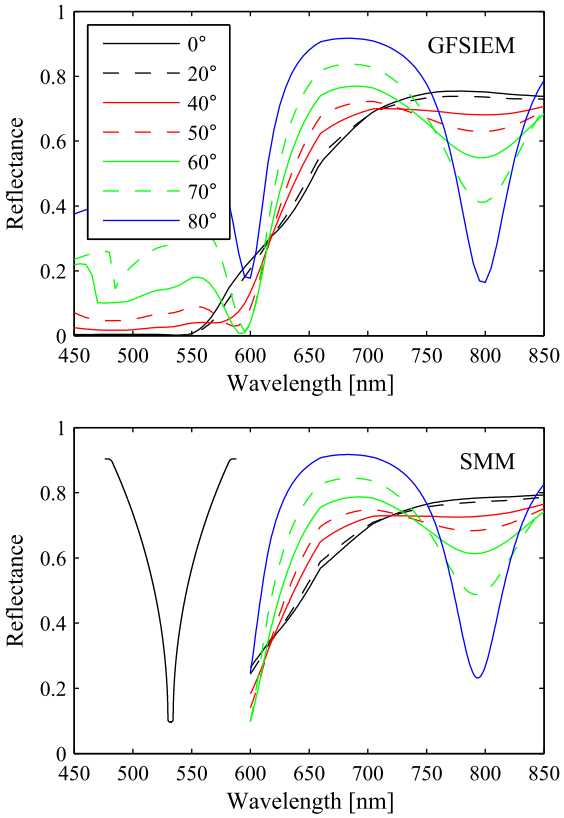

Fig. 7. (Color online) GFSIEM and SMM results for the reflectance of the structure with a bottom width of 10 nm ($\Lambda = 250$ nm, $h = 500$ nm) under angles of incidence in the xy plane. The inset on the left-hand side of the bottom figure shows one period of the actual structure.

at larger angles of incidence in the yz plane.

The results obtained for the other structures (not shown) exhibit equal similarities between results produced with the two methods as those presented here. It is remarkable that such a large degree of agreement is obtained between the rigorous GFSIEM and a highly simplified matrix model for a large range of different structures. Since the SMM does not account for diffraction, a contributing factor to the remarkable results obtained with the method here is the fact that the period of the structure is relatively small compared to the wavelength, which eliminates the case of far-field diffraction. It should also be noted that in our matrix model we treat the coupling of light to plasmons in a way such that all light transmitted across the first interface is coupled to plasmons in the groove. This is a reasonable assumption for structures as those considered in this paper, where the separation between neighboring grooves is very small compared to the period of the structure, such that the reflection caused by the plateaus between grooves is negligible. If the model were to be used for structures with significantly larger groove spacing, it would be necessary to incorporate some coupling factor in the transmission across the first interface in order to account for the increased reflection caused by the larger plateaus.

We have not included results for angles of incidence in the yz plane with $\theta > 70°$. At large angles in this direction E_z and H_z will become small compared to $\mathbf{E}_s$ and $\mathbf{H}_s$, and since our GFSIEM uses the z components of the fields it converges poorly in cases where the z components constitute a small part of the total fields.

While the results obtained for an angle of incidence in the xy plane can be verified by comparison with other results presented in the literature (see [7]), results for incidence in the yz plane have not previously been shown. The overwhelming similarity in the results obtained with the two very different methods used here, however, shows the validity of the method we present for modeling periodic nanostructures under a general direction of light incidence.

5. Conclusion

In this paper we have introduced two methods for modeling the reflection of light incident under a general direction of incidence on arrays of periodic ultra-sharp grooves in a gold surface. We presented a simple SMM as well as a rigorous method based on the GFSIEM. The

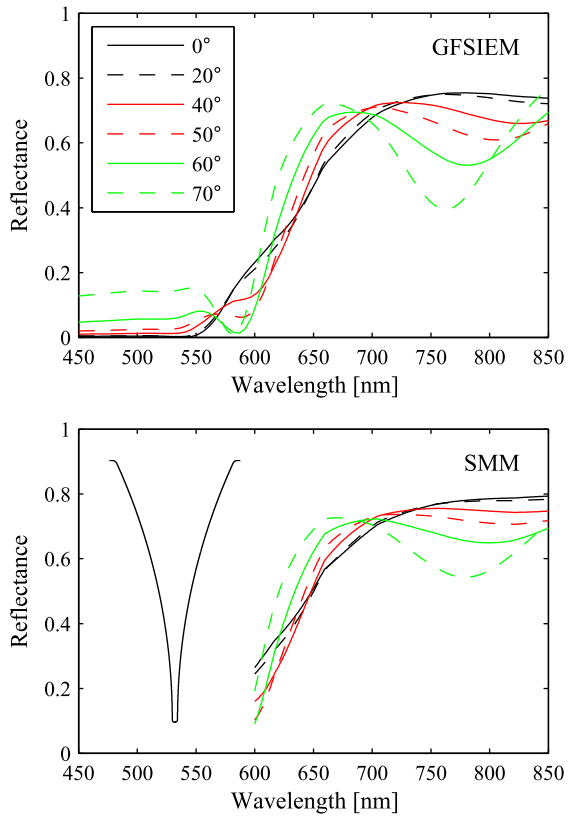

Fig. 8. (Color online) GFSIEM and SMM results for the reflectance of the structure with a bottom width of 10 nm ($\Lambda = 250$ nm, $h = 500$ nm) under angles of incidence in the yz plane. The inset on the left-hand side of the bottom figure shows one period of the actual structure.

results of the SMM show a remarkably large degree of similarity to those of the exact GFSIEM. We obtained good agreement between the two methods for structures with different bottom groove widths in a large range (0.3-50 nm).

The agreement between the two methods has two important consequences. First, it clearly demonstrates that the absorption of light in ultra-sharp grooves is dominated by the coupling of light into plasmons, since the SMM is almost entirely based on the properties of G-SPP waves. Furthermore, it opens possibilities for much faster calculations of reflectance spectra of plasmonic nanostructures. While our implementation of the GFSIEM in MATLAB takes upwards of 20 minutes to calculate the reflectance at a single wavelength for a single angle of incidence when run on a single CPU core, our SMM produces a full reflectance spectrum for 251 wavelengths in the range of 600-850 nm for seven different angles of incidence in less than five minutes. As the results of the SMM are very close to the exact results, this method can be used to quickly obtain an overview of the reflectance properties of a given structure.

While normal incidence exhibits the lowest reflectance overall, the reflectance calculations for angles of incidence in the yz plane generally show lower reflectances across the wavelength spectrum than those for incidence in the xy plane. As such this direction of incidence would be preferable in applications such as thermophotovoltaics, concentrated solar power, or broadband polarizers for short laser pulses, where low reflectivity is desired and different angles of incidence may occur.

Acknowledgments

The authors gratefully acknowledge financial support from the Danish Research Council for Independent Research (FTP contract no. 09-072949 ANAP), and from the Danish Advanced Technology Foundation (contract no. 063-2011-1).

References

[1] M. K. Hedayati, M. Javaherirahim, B. Mozooni, R. Abdelaziz, A. Tavassolizadeh, V. S. K. Chakravadhanula, V. Zaporojtchenko, T. Strunkus, F. Faupel, and M. Elbahri, "Design of a perfect black absorber at visible frequencies using plasmonic metamaterials," Advanced Materials **23**, 5410–5414 (2011).

[2] V. Kravets, S. Neubeck, A. Grigorenko, and A. Kravets, "Plasmonic blackbody: Strong absorption of light by metal nanoparticles embedded in a dielectric matrix," Physical Review B **81**, 165401 (2010).

[3] A. Pfund, "The optical properties of metallic and crystalline powders," JOSA **23**, 375–377 (1933).

[4] A. Vorobyev and C. Guo, "Femtosecond laser blackening of platinum," Journal of applied physics **104**, 053516 (2008).

[5] M. Bora, E. M. Behymer, D. A. Dehlinger, J. A. Britten, C. C. Larson, A. S. Chang, K. Munechika, H. T. Nguyen, and T. C. Bond, "Plasmonic black metals in resonant nanocavities," Applied Physics Letters **102**, 251105 (2013).

[6] T. Søndergaard, S. M. Novikov, T. Holmgaard, R. L. Eriksen, J. Beermann, Z. Han, K. Pedersen, and S. I. Bozhevolnyi, "Plasmonic black gold by adiabatic nanofocusing and absorption of light in ultra-sharp convex grooves," Nature communications **3**, 969 (2012).

[7] T. Søndergaard and S. I. Bozhevolnyi, "Theoretical analysis of plasmonic black gold: periodic arrays of ultra-sharp grooves," New Journal of Physics **15**, 013034 (2013).

[8] E. Skovsen, T. Søndergaard, C. Lemke, T. Holmgaard, T. Leißner, R. Eriksen, J. Beermann, M. Bauer, K. Pedersen, and S. Bozhevolnyi, "Plasmonic black gold based broadband polarizers for ultra-short laser pulses," Applied Physics Letters **103**, 211102 (2013).

[9] J. Porto, F. Garcia-Vidal, and J. Pendry, "Transmission resonances on metallic gratings with very narrow slits," Physical review letters **83**, 2845 (1999).

[10] F. Garcia-Vidal and L. Martin-Moreno, "Transmission and focusing of light in one-dimensional periodically nanostructured metals," Physical Review B **66**, 155412 (2002).

[11] J.-J. Greffet, R. Carminati, K. Joulain, J.-P. Mulet, S. Mainguy, and Y. Chen, "Coherent emission of light by thermal sources," Nature **416**, 61–64 (2002).

[12] A. Christ, T. Zentgraf, S. Tikhodeev, N. Gippius, O. Martin, J. Kuhl, and H. Giessen, "Interaction between localized and delocalized surface plasmon polariton modes in a metallic photonic crystal," physica status solidi (b) **243**, 2344–2348 (2006).

[13] S. Collin, G. Vincent, R. Haïdar, N. Bardou, S. Rommeluère, and J.-L. Pelouard, "Nearly perfect fano transmission resonances through nanoslits drilled in a metallic membrane," Physical review letters **104**, 027401 (2010).

[14] Y. Bao, Y. Hou, and Z. Wang, "Robust existence of the broadband optical transmission effect in multiple-layer gratings," JOSA B **31**, 255–258 (2014).

[15] W. Yan, N. A. Mortensen, and M. Wubs, "Green's function surface-integral method for nonlocal response of plasmonic nanowires in arbitrary dielectric environments," Physical Review B **88**, 155414 (2013).

[16] M. Moharam, E. B. Grann, D. A. Pommet, and T. Gaylord, "Formulation for stable and efficient implementation of the rigorous coupled-wave analysis of binary gratings," JOSA A **12**, 1068–1076 (1995).

[17] D. W. Prather, M. S. Mirotznik, and J. N. Mait, "Boundary integral methods applied to the analysis of diffractive optical elements," JOSA A **14**, 34–43 (1997).

[18] D. W. Prather, J. N. Mait, M. S. Mirotznik, and J. P. Collins, "Vector-based synthesis of finite aperiodic subwavelength diffractive optical elements," JOSA A **15**, 1599–1607 (1998).

[19] J. Liu, B.-Y. Gu, B.-Z. Dong, and G.-Z. Yang, "Interference effect of dual diffractive cylindrical microlenses analyzed by rigorous electromagnetic theory," JOSA A **18**, 526–536 (2001).

[20] J. Jung and T. Søndergaard, "Greens function surface integral equation method for theoretical analysis of scatterers close to a metal interface," Physical Review B **77**, 245310 (2008).

[21] M. K. Choi, "Numerical calculation of light scattering from a layered sphere by the boundary-element method," JOSA A **18**, 577–583 (2001).

[22] N. Zavareian and R. Massudi, "Controllable trapping of nanowires using a symmetric slot waveguide," The Journal of Physical Chemistry C **117**, 17159–17166 (2013).

[23] B. Prade, J. Vinet, and A. Mysyrowicz, "Guided optical waves in planar heterostructures with negative dielectric constant," Phys. Rev. B **44**, 13556–13572 (1991).

[24] S. I. Bozhevolnyi and J. Jung, "Scaling for gap plasmon based waveguides," Optics express **16**, 2676–2684 (2008).

[25] F. Kong, K. Li, B.-I. Wu, H. Huang, H. Chen, and J. A. Kong, "Propagation properties of the spp modes in nanoscale narrow metallic gap, channel, and hole geometries," Progress In Electromagnetics Research **76**, 449–466 (2007).

[26] H. T. Miyazaki and Y. Kurokawa, "Squeezing visible light waves into a 3-nm-thick and 55-nm-long plasmon cavity," Physical review letters **96**, 097401 (2006).

[27] H. Choo, M.-K. Kim, M. Staffaroni, T. J. Seok, J. Bokor, S. Cabrini, P. J. Schuck, M. C. Wu, and E. Yablonovitch, "Nanofocusing in a metal-insulator-metal gap plasmon waveguide with a three-dimensional linear taper," Nature Photonics **6**, 838–844 (2012).

[28] S. Jette-Charbonneau, R. Charbonneau, N. Lahoud, G. A. Mattiussi, and P. Berini, "Bragg gratings based on long-range surface plasmon-polariton waveguides: Comparison of theory and experiment," Quantum Electronics, IEEE Journal of **41**, 1480–1491 (2005).

[29] S. Jetté-Charbonneau and P. Berini, "Theoretical performance of bragg gratings based on long-range surface plasmon-polariton waveguides," JOSA A **23**, 1757–1767 (2006).

[30] M. V. Klein and T. E. Furtak, *Optics, Second Edition* (John Wiley & Sons, Inc., 1986), chap. 5.4A.

[31] D. K. Gramotnev, "Adiabatic nanofocusing of plasmons by sharp metallic grooves: Geometrical optics approach," Journal of applied physics **98**, 104302 (2005).

[32] T. Søndergaard, "Modeling of plasmonic nanostructures: Green's function integral equation methods," physica status solidi (b) **244**, 3448–3462 (2007).

[33] T. Søndergaard, J. Gadegaard, P. K. Kristensen, T. K. Jensen, T. G. Pedersen, and K. Pedersen, "Guidelines for 1d-periodic surface microstructures for antireflective lenses," Optics express **18**, 26245–26258 (2010).

[34] T. Søndergaard, S. I. Bozhevolnyi, J. Beermann, S. M. Novikov, E. Devaux, and T. W. Ebbesen, "Extraordinary optical transmission with tapered slits: effect of higher diffraction and slit resonance orders," JOSA B **29**, 130–137 (2012).

[35] W. C. Chew, *Waves and fields in inhomogeneous media* (IEEE press New York, 1995), chap. 8.

[36] P. B. Johnson and R. W. Christy, "Optical constants of the noble metals," Physical Review B **6**, 4370 (1972).

Bibliography

[1] T. Bauer, *Thermophotovoltaics: Basic Principles and Critical Aspects of System Design* (Springer, 2011). ISBN: 978-3-642-19964-6.

[2] International Energy Agency, "Technology roadmap: Concentrating solar power," (2010). URL: `http://www.iea.org/publications/freepublications/publication/csp_roadmap.pdf`, Downloaded (29/6-13).

[3] M. K. Hedayati, M. Javaherirahim, B. Mozooni, R. Abdelaziz, A. Tavassolizadeh, V. S. K. Chakravadhanula, V. Zaporojtchenko, T. Strunkus, F. Faupel, and M. Elbahri, "Design of a perfect black absorber at visible frequencies using plasmonic metamaterials," Advanced Materials **23**, 5410–5414 (2011).

[4] V. Kravets, S. Neubeck, A. Grigorenko, and A. Kravets, "Plasmonic blackbody: Strong absorption of light by metal nanoparticles embedded in a dielectric matrix," Physical Review B **81**, 165401 (2010).

[5] A. Pfund, "The optical properties of metallic and crystalline powders," JOSA **23**, 375–377 (1933).

[6] A. Vorobyev and C. Guo, "Femtosecond laser blackening of platinum," Journal of applied physics **104**, 053516 (2008).

[7] M. Bora, E. M. Behymer, D. A. Dehlinger, J. A. Britten, C. C. Larson, A. S. Chang, K. Munechika, H. T. Nguyen, and T. C. Bond, "Plasmonic black metals in resonant nanocavities," Applied Physics Letters **102**, 251105 (2013).

[8] T. Søndergaard, S. M. Novikov, T. Holmgaard, R. L. Eriksen, J. Beermann, Z. Han, K. Pedersen, and S. I. Bozhevolnyi, "Plasmonic black gold by adiabatic nanofocusing and absorption of light in ultra-sharp convex grooves," Nature communications **3**, 969 (2012).

[9] T. Søndergaard and S. I. Bozhevolnyi, "Theoretical analysis of plasmonic black gold: periodic arrays of ultra-sharp grooves," New Journal of Physics **15**, 013034 (2013).

[10] E. Skovsen, T. Søndergaard, C. Lemke, T. Holmgaard, T. Leißner, R. Eriksen, J. Beermann, M. Bauer, K. Pedersen, and S. Bozhevolnyi, "Plasmonic black gold based broadband polarizers for ultra-short laser pulses," Applied Physics Letters **103**, 211102 (2013).

[11] J. Porto, F. Garcia-Vidal, and J. Pendry, "Transmission resonances on metallic gratings with very narrow slits," Physical review letters **83**, 2845 (1999).

[12] F. Garcia-Vidal and L. Martin-Moreno, "Transmission and focusing of light in one-dimensional periodically nanostructured metals," Physical Review B **66**, 155412 (2002).

[13] J.-J. Greffet, R. Carminati, K. Joulain, J.-P. Mulet, S. Mainguy, and Y. Chen, "Coherent emission of light by thermal sources," Nature **416**, 61–64 (2002).

[14] A. Christ, T. Zentgraf, S. Tikhodeev, N. Gippius, O. Martin, J. Kuhl, and H. Giessen, "Interaction between localized and delocalized surface plasmon polariton modes in a metallic photonic crystal," physica status solidi (b) **243**, 2344–2348 (2006).

[15] S. Collin, G. Vincent, R. Haïdar, N. Bardou, S. Rommeluère, and J.-L. Pelouard, "Nearly perfect fano transmission resonances through nanoslits drilled in a metallic membrane," Physical review letters **104**, 027401 (2010).

[16] Y. Bao, Y. Hou, and Z. Wang, "Robust existence of the broadband optical transmission effect in multiple-layer gratings," JOSA B **31**, 255–258 (2014).

[17] W. Yan, N. A. Mortensen, and M. Wubs, "Green's function surface-integral method for nonlocal response of plasmonic nanowires in arbitrary dielectric environments," Physical Review B **88**, 155414 (2013).

[18] M. Moharam, E. B. Grann, D. A. Pommet, and T. Gaylord, "Formulation for stable and efficient implementation of the rigorous coupled-wave analysis of binary gratings," JOSA A **12**, 1068–1076 (1995).

[19] D. W. Prather, M. S. Mirotznik, and J. N. Mait, "Boundary integral methods applied to the analysis of diffractive optical elements," JOSA A **14**, 34–43 (1997).

[20] D. W. Prather, J. N. Mait, M. S. Mirotznik, and J. P. Collins, "Vector-based synthesis of finite aperiodic subwavelength diffractive optical elements," JOSA A **15**, 1599–1607 (1998).

[21] J. Liu, B.-Y. Gu, B.-Z. Dong, and G.-Z. Yang, "Interference effect of dual diffractive cylindrical microlenses analyzed by rigorous electromagnetic theory," JOSA A **18**, 526–536 (2001).

[22] J. Jung and T. Søndergaard, "Green's function surface integral equation method for theoretical analysis of scatterers close to a metal interface," Physical Review B **77**, 245310 (2008).

[23] M. K. Choi, "Numerical calculation of light scattering from a layered sphere by the boundary-element method," JOSA A **18**, 577–583 (2001).

[24] N. Zavareian and R. Massudi, "Controllable trapping of nanowires using a symmetric slot waveguide," The Journal of Physical Chemistry C **117**, 17159–17166 (2013).

[25] L. Novotny and B. Hecht, *Principles of Nano-Optics, Second Edition* (Cambridge University Press, 2012). ISBN: 978-1-107-00546-4.

[26] B. Prade, J. Vinet, and A. Mysyrowicz, "Guided optical waves in planar heterostructures with negative dielectric constant," Phys. Rev. B **44**, 13556–13572 (1991).

[27] S. I. Bozhevolnyi and J. Jung, "Scaling for gap plasmon based waveguides," Optics express **16**, 2676–2684 (2008).

[28] M. V. Klein and T. E. Furtak, *Optics, Second Edition* (John Wiley & Sons, Inc., 1986). ISBN: 0-471-87297-0.

[29] T. Søndergaard, *Lecture notes for Ph.D course: Green's function integral equation methods for electromagnetic scattering problems* (2012).

[30] T. Søndergaard, "Modeling of plasmonic nanostructures: Green's function integral equation methods," physica status solidi (b) **244**, 3448–3462 (2007).

[31] T. Søndergaard, J. Gadegaard, P. K. Kristensen, T. K. Jensen, T. G. Pedersen, and K. Pedersen, "Guidelines for 1d-periodic surface microstructures for antireflective lenses," Optics express **18**, 26245–26258 (2010).

[32] T. Søndergaard, S. I. Bozhevolnyi, J. Beermann, S. M. Novikov, E. Devaux, and T. W. Ebbesen, "Extraordinary optical transmission with tapered slits: effect of higher diffraction and slit resonance orders," JOSA B **29**, 130–137 (2012).

[33] W. C. Chew, *Waves and fields in inhomogeneous media* (IEEE press New York, 1995), chap. 8.

[34] M. F. Modest, *Radiative Heat Transfer, Second Edition* (Academic Press, 2003). ISBN: 0-12-503163-7.

[35] P. B. Johnson and R. W. Christy, "Optical constants of the noble metals," Physical Review B **6**, 4370 (1972).

[36] D. K. Gramotnev, "Adiabatic nanofocusing of plasmons by sharp metallic grooves: Geometrical optics approach," Journal of applied physics **98**, 104302 (2005).

[37] G. V. Naik, J. L. Schroeder, X. Ni, A. V. Kildishev, T. D. Sands, and A. Boltasseva, "Titanium nitride as a plasmonic material for visible and near-infrared wavelengths," Optical Materials Express **2**, 478–489 (2012).